Analysis of Energy Transfer among Background Flow, Gravity Waves and Turbulence in the mesopause region in the process of Gravity Wave Breaking from a High-resolution Atmospheric Model

Fan Yang[1], Wenjun Dong[2], Alan Z Liu[1], Thomas Lund[3], Christopher James Heale[1], and Jonathan Brian Snively[1]

[1]Embry-Riddle Aeronautical University
[2]Global Atmospheric Technologies and Sciences
[3]GATS

March 13, 2023

Abstract

We conducted an analysis of the process of GW breaking from an energy perspective using the output from a high-resolution compressible atmospheric model. The investigation focused on the energy conversion and transfer that occur during the GW breaking. The total change in kinetic energy and the amount of energy converted to internal energy and potential energy within a selected region were calculated.

Prior to GW breaking, part of the potential energy is converted into kinetic energy, most of which is transported out of the chosen region. After the GW breaks and turbulence develops, part of the potential energy is converted into kinetic energy, most of which is converted into internal energy.

The calculations for the transfer of kinetic energy among GWs, turbulence, and the BG in a selected region, as well as the contributions from various interactions (BG-GW, BG-turbulence, and GW-turbulence), are performed. At the point where the GW breaks, turbulence is generated. As the GW breaking process proceeds, the GWs lose energy to the background. At the start of the GW breaking, turbulence receives energy through interactions between GWs and turbulence, and between the BG and turbulence. Once the turbulence has accumulated enough energy, it begins to absorb energy from the background while losing energy to the GWs.

The probabilities of instability are calculated during various stages of the GW-breaking process. The simulation suggests that the propagation of GWs results in instabilities, which are responsible for the GW breaking. As turbulence grows, it reduces convective instability.

Analysis of Energy Transfer among Background Flow, Gravity Waves and Turbulence in the mesopause region in the process of Gravity Wave Breaking from a High-resolution Atmospheric Model

Fan Yang[1],*Wenjun Dong[1 2], Thomas Lund[2], Alan Z. Liu[1], Christopher Heale[1], Jonathan B. Snively[1]

[1] Center for Space and Atmospheric Research, Department of Physical Sciences, Embry-Riddle Aeronautical University, Daytona Beach, FL, USA.

[2] GATS, Boulder, CO, USA.

Key Points:

- The energy flow during a GW breaking case was investigated via a high-resolution atmospheric model.
- The wave-flow interactions dominate the wave-breaking energy-transferring process.
- Kinetic energy in background, gravity wave, and turbulence transfer among each other through nonlinear interactions.

*Department of Physical Sciences, Embry-Riddle Aeronautical University, 1 Aerospace Blvd, Daytona Beach, FL 32114-3900, USA

Abstract

We conducted an analysis of the process of GW breaking from an energy perspective using the output from a high-resolution compressible atmospheric model. The investigation focused on the energy conversion and transfer that occur during the GW breaking. The total change in kinetic energy and the amount of energy converted to internal energy and potential energy within a selected region were calculated. Prior to GW breaking, part of the potential energy is converted into kinetic energy, most of which is transported out of the chosen region. After the GW breaks and turbulence develops, part of the potential energy is converted into kinetic energy, most of which is converted into internal energy. The calculations for the transfer of kinetic energy among GWs, turbulence, and the BG in a selected region, as well as the contributions from various interactions (BG-GW, BG-turbulence, and GW-turbulence), are performed. At the point where the GW breaks, turbulence is generated. As the GW breaking process proceeds, the GWs lose energy to the background. At the start of the GW breaking, turbulence receives energy through interactions between GWs and turbulence, and between the BG and turbulence. Once the turbulence has accumulated enough energy, it begins to absorb energy from the background while losing energy to the GWs. The probabilities of instability are calculated during various stages of the GW-breaking process. The simulation suggests that the propagation of GWs results in instabilities, which are responsible for the GW breaking. As turbulence grows, it reduces convective instability.

1 Plain language

In this study, we utilized a high-resolution atmospheric model to analyze the energy flow of a gravity breaking event. Our main focus was to examine the conversion and transfer of energy during this process, and to investigate how it moves between gravity waves, turbulence, and the background atmosphere. To accomplish this, we formulated change rate equations for the kinetic energy tendencies of turbulence, gravity waves, and background flow, and assessed how various processes and interactions contribute to the kinetic energy change rate. Our findings reveal that when gravity waves break, they lose energy to the background flow, while turbulence gains energy from interactions with both gravity waves and the background flow. Additionally, we calculated the conversion and transfer of energy during the gravity wave breaking process and discovered that potential energy transforms into kinetic energy both before and after the gravity wave breaking.

Furthermore, we evaluated the probability of instabilities occurring during different stages of the gravity wave breaking and found that turbulence can diminish convective instability as it grows.

2 Introduction

Gravity wave (GW) breaking plays an important role in depositing the momentum and energy in GWs to the background mean flow. [*Lindzen*, 1981; *Dunkerton and Fritts*, 1984]. GW breaking process is related to GW propagation, turbulence, interactions of different scales, and instabilities.

A complete quantification of GW breaking dynamics and consequences requires direct numerical simulation (DNS). *Barat and Genie* [1982] and *Hunt et al.* [1985] suggested that the atmosphere has a vertical structure characterized by strong stable 'sheet' and less stable 'layers'. The S&L structures play an important role in the transport and mixing of heat, momentum, and constituents. The formation mechanisms of S&L structures arising from superposition of stable GWs and mean shears are referred as 'Multi-scale dynamics' (MSD). MSD drives S&L structure and evolutions. MSD includes KHI, GW breaking, and fluid intrusions [*Fritts et al.*, 2013a].

Among all physical processes during GW breaking, the mechanism of turbulence development is one of the most important scientific topics because of its effects on weather, climate, aircraft, and atmospheric observations[*Reiter*, 1969]. Turbulent flows develop spinning or swirling fluid structures called eddies[*Doran*, 2013]. *Winters and Riley* [1992] found a major source of eddy kinetic energy (KE) would be buoyancy. Besides the buoyancy terms, large shears in the mean and GW motion fields also contribute to the formation of eddy structures. The vertical shear is the dominant source of eddy KE after the initial wave collapse. The pressure-work terms contribute very little to the eddy KE [*Fritts et al.*, 1994]. *Palmer* [1996]; *Fritts et al.* [1996], and *Werne and Fritts* [1999] studied the dynamics of turbulence generation due to KH instability. *Fritts and Alexander* [2003] suggested turbulence arises mainly due to Kelvin-Helmholz (KH) shear instability and GW breaking. KH shear is more common at lower altitudes such as the troposphere and stratosphere. GW breaking is more important at higher altitudes and is the dominant source in the mesosphere. *Achatz* [2007] emphasized that the 'statically enhanced roll mechanism' is a strong contributor to the tendency of turbulence energy. GW-breaking and KHI play major roles in leading to strong turbulence. Fluid intrusions play more significant roles following the initial KHI [*Fritts et al.*, 2016, 2017a]. *Fritts et al.* [2017b] and *Dong et al.* [2022] explored the dynamics of GW encountering a mesospheric inversion layer (MIL). They found mean fields are driven largely by 2D GW and instability dynamics. They implicated that turbulence due to GW overturning arises in a transient phase of the GW that has weak convective stability. Further exploring of KHI leads to cases of 'tube and knot' (T&K) dynamics. T&K dynamics accelerate the transition from KH billow to turbulence. It may also enable strong turbulence to occur at large Richardson numbers [*Fritts et al.*, 2022a].

Besides DNS studies, multiple observational studies have been conducted to reveal the mechanisms of turbulence generation. *Lindzen* [1967, 1968] noted the possible mechanism of turbulence generation from wave breaking in the mesosphere. *Lindzen* [1971, 1981] argued that 'turbulent' diffusion could also result from nonbreaking waves. *Atlas and Bretherton* [2022] used aircraft measurements to correlate gravity waves (GWs) and turbulence with tropical tropopause layer cirrus. They found during their observation, turbulence co-occurred with GWs 95 % of the time. Observations also suggest that the dynamics of GW energy dissipation often involve 'sheet and layer' (S&L) structures [*Fritts et al.*, 2004; *Clayson and Kantha*, 2008; *Fritts et al.*, 2017a]. *Zovko-Rajak et al.* [2019] found near-cloud turbulence is associated with strong GWs generated by moist convection.

Nonlinear interactions are crucial in the GW-breaking process. Multiple nonlinear saturation theories were proposed [*Dunkerton*, 1987; *Klostermeyer*, 1991; *Hines*, 1991; *Fritts et al.*, 2003] to explain the relationships between instabilities and nonlinear interactions that are not accounted for in a linear theory. Both mechanisms helped to explain the wave-breaking processes and instabilities. Nonlinearity mainly includes the interactions among wave, turbulence, vortex, and background flow [*Lelong and Riley*, 1991; *Bühler*, 2010; *Fritts et al.*, 2015; *Dong et al.*, 2020; *Fritts et al.*, 2020]. Wave-turbulence interactions can modify primary wave amplitudes [*Fua et al.*, 1982; *Einaudi and Finnigan*, 1993]. Wave breaking, which can be triggered by wave-mean flow interactions [*Sutherland*, 2010; *Pairaud et al.*, 2010], is one of the most common mechanisms for turbulence generation. *Koch et al.* [2005] found that GWs and turbulence are often observed simultaneously due to GW instability being the source of turbulence. Their research showed that turbulence intensity did not vary with wave phase. They also discovered that turbulence is mostly forced at a horizontal scale of 700 m, with energy from both larger and smaller scales being transferred to this scale. Two-dimensional model result [*Liu et al.*, 2014] showed that the momentum deposited by breaking GWs accelerates the mean wind. GW breaking accelerates the background wind suggesting that the nonlinear interactions increase the tidal amplitude [*Liu et al.*, 2008]. *Fritts et al.* [2013b] revealed 2D wave-wave interactions are the only (sole) cause of the decrease of primary GW amplitude. They conclude that turbulence is highly dependent on the orientation of the GW. *Barbano et al.* [2022] evaluated the wave-turbulence interaction through triple decomposition [*Reynolds and Hussain*, 1972; *Finnigan and Einaudi*, 1981; *Finnigan et al.*, 1984] focusing on the production of turbulence momentum flux and wave shear or vorticity, which is one part of the wave-turbulence interaction. This particular aspect of wave-turbulence interactions can cause both the production and destruction of turbulent energy.

GW breaking is often associated with instabilities, which can induce its occurrence, as noted by *Sedlak et al.* [2021]. *Achatz* [2007] discussed how singular vectors (SVs) can destabilize statically and dynamically stable low-frequency inertia-GWs, while normal modes (NMs) destabilize can statically stable high-frequency GWs. In an observatory study, *Yang and Liu* [2022] reported GW instabilities and their relationship with GW frequencies using ALO lidar measurements.

There have been a number of research on mechanisms for GW breaking. Most studies focus on the dynamical process, not on the energetics of this process. The energetics provides important insights of the growth and delay of different components in the interactions. Many studies also focus on how wave breaks into turbulence, but not how turbulence influences the wave and/or the background. This work looks at all three components together from the energy perspective, and not just on the initial breaking of a wave, but also the eventual decay of the turbulence. Physical understanding of nonlinear interactions is still lacking. Improved understanding is critical for weather and environmental forecasts [*Sun et al.*, 2015].

The primary purpose of this paper is to study the dynamics of a GW breaking and assess the roles played by GWs and their background (BG) flow in the process. The objectives of this paper are to quantify the energy conversion among kinetic energy (KE), potential energy (PE), and internal energy (IE) and to determine the contributions to turbulence generation from nonlinear interactions of various scales and their energy transfer directions during a gravity wave breaking process. The structure of this study is as follows: In Section 2, we introduce the model and its inputs used in the study. Section 3 outlines the methodology of our analysis. The results, including the findings on energy conversions, the transfer of kinetic energy (KE) among the background, GWs, and turbulence, and the connection between instabilities and GW breaking, are presented in Section 4. The results are discussed in detail in Section 5. The conclusions of the study are summarized in Section 6. Finally, Appendixes A and B present the derivations of the formulations used in Section 3.

3 Model Description

The model used for this study is the Complex Geometry Compressible Atmospheric Model (CGCAM) described extensively by *Dong et al.* [2020] (hereafter D20). CGCAM satisfies the numerical conservation of mass, momentum, and kinetic and thermal energies since it discretizes the compressible Navier-Stokes equations [*Felten and Lund*, 2006]. See D20 for additional details.

As for background, a uniform temperature profile, $T_0(z) = 300$ K, is used which yields a scale height $H \sim 8.9$ km, a buoyancy frequency $N \sim 0.018$ s^{-1}. To make the model results comparable to lidar observation, the vertical wavelength is chosen to be 15 km. Therefore, the initial GW has a horizontal wavelength $\lambda_x = 45$ km, a vertical wavelength $\lambda_z = 15$ km, and a horizontal intrinsic phase speed $ci = -u_0(z) = -40.1$ m/s, which results in an intrinsic wave period of $2\pi/\omega = \lambda_x/ci = 1122$ s. The initial GW packet is introduced into the domain by specifying the streamwise velocity distribution. See detail in D20.

The simulations used here are performed in a Cartesian computational domain. The computational domains extend from -150 km to 150 km in the streamwise (x) direction and from 0 km to 170 km in the vertical (z) direction. The resolutions Δx and Δz in the zone of instability, GW breaking, and turbulence are both 300 m. Periodic boundary conditions are used in the x direction. Isothermal no-stress wall conditions are used at the lower boundary and a characteristic radiation boundary condition is used at the upper boundary. Numerical sponge layers are used at all boundaries to absorb the energy of outgoing fluctuations. The sponge layers are 20 km deep at the upper boundary, 5 km deep at the lower boundary, and 10 km wide at the streamwise boundaries. The sponges work as force terms added to conservation equations. See details in equation (33) in D20.

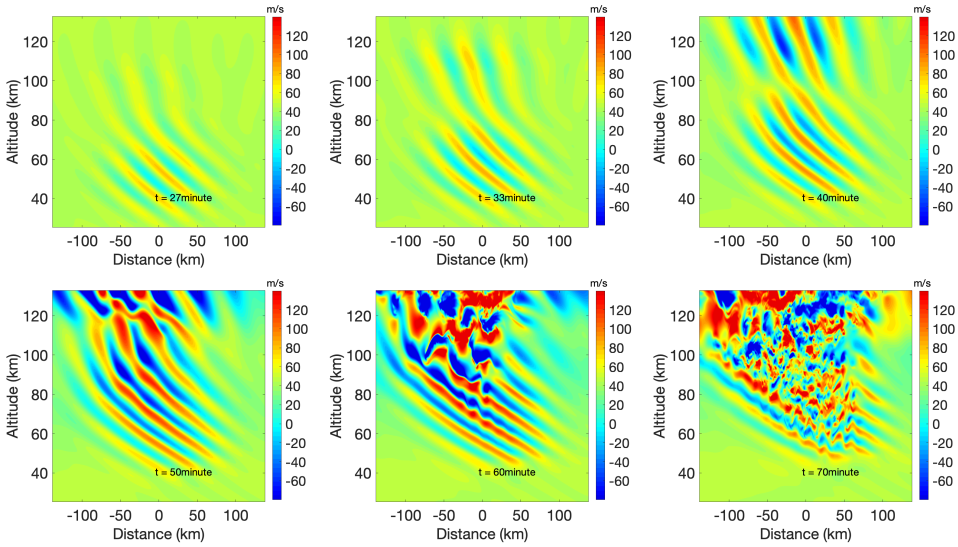

Figure 1: u (m/s) generated by 2D CGCAM at 6 times. They represent the horizontal wind speed in sequence from left to right, and from top to bottom, at the 27th, 33rd, 40th, 50th, 60th, and 70th minutes, respectively.

The output of CGCAM is used to investigate the energy transfer among turbulence, GWs, and background flow. The outputs of CGCAM are ρ, ρu, ρw and ρE. With ideal gas law, the temperature T, horizontal wind speed u, vertical wind speed w, pressure p, and density ρ can be derived. u at six different times are presented in Figure 1 as an example to depict the wave-breaking process. The initial condition for the simulation is a single GW with horizontal and vertical wavelengths of 45 km and 15 km, respectively. This study investigates the GW breaking process at the mesopause region. Thus, the activities in a 45 km-horizontal (-22.5 km - 22.5 km) and 15 km-vertical region at mesopause region (85 km - 100 km) are studied. In this chosen region, the GWs start to break around the 56th minute.

4 Methodology

Energy transfers studied in this paper include two sets. One set is energy conversion between KE, IE, and PE of the atmosphere. The other set is the kinetic energy transfer among BG, GWs, and turbulence.

4.1 Energy Conversion

Energy conversions are related to total KE, IE, and PE tendencies. The energy tendencies of KE, IE, and PE are:

$$\begin{aligned} \frac{\partial KE}{\partial t} &= -\nabla \cdot (KE\vec{v}) - \vec{v} \cdot \nabla p - g\rho w \\ &= -\nabla \cdot (KE\vec{v}) - \nabla \cdot (p\vec{v}) + p\nabla \cdot \vec{v} - g\rho w, \end{aligned} \tag{1}$$

$$\begin{aligned} \frac{\partial IE}{\partial t} &= -\mathrm{C_v}T(\vec{v} \cdot \nabla\rho + \rho\nabla \cdot \vec{v}) - p\nabla \cdot \vec{v} - \mathrm{C_v}\rho\vec{v} \cdot \nabla T + \kappa\nabla^2 T \\ &= -\nabla \cdot (IE\vec{v}) - p\nabla \cdot \vec{v}, \end{aligned} \tag{2}$$

$$\begin{aligned} \frac{\partial pE}{\partial t} &= gh\frac{\partial\rho}{\partial t} + g\rho w = -gh\,(\vec{v} \cdot \nabla\rho + \rho\nabla \cdot \vec{v}) + g\rho w \\ &= -\nabla \cdot (PE\vec{v}) + g\rho w, \end{aligned} \tag{3}$$

where $\mathrm{C_v}$ is the specific heat at constant volume. κ is the conductivity, and κ is not a constant. See details and deductions for the energy tendencies in Appendix A.

PE, KE, and IE vary through transportation and conversions among each other. KE tendency is related to the divergence/convergence of KE flux ($-\nabla \cdot (KE\vec{v})$), air expansion/compression ($-\nabla \cdot (p\vec{v})$), pressure doing work on air expansion/compression ($p\nabla \cdot \vec{v}$), and gravity force doing work ($-g\rho w$). IE tendency is related to the divergence/convergence of IE flux ($-\nabla \cdot (IE\vec{v})$) and pressure doing work on air expansion/compression ($-p\nabla \cdot \vec{v}$). PE tendency is related to the divergence/convergence of PE flux ($-\nabla \cdot (PE\vec{v})$) and gravity force doing work on air expansion/compression ($g\rho w$). KE tendency and IE tendency are related through the term $(\pm)p\nabla \cdot \vec{v}$. KE tendency and PE tendency are related through the term $(\mp)\rho g W$. The conversion between KE and IE occurs through pressure doing work on flow expansion/compression. The conversion between KE and PE is through gravity force doing work.

4.2 Kinetic Energy Transfer between Background and Perturbations

A typical approach for analyzing flow motion is to decompose the perturbation from the mean flow [*Reynolds and Hussain*, 1972; *Finnigan and Einaudi*, 1981; *Yim et al.*, 2019; *Barbano et al.*, 2022]. A variable or product of variables Q is divided into a BG-period-average (BPA) value (Q_0) and a fluctuation (Q_1) whose BPA value is zero, where BPA is defined as the temporal average over the period of the wave or perturbation. The BPA is indicated by the overline symbol $\overline{Q}$.

The calculation of KE tendency involves the process of decomposition. The transfer of KE between the BG and perturbations can be demonstrated through the examination of their respective KE tendencies. The background and the perturbation KE tendencies yield (See deductions in Appendix B):

$$\begin{aligned} &\frac{\partial KE_0}{\partial t} + \rho_0 u_0 u_0 \frac{\partial u_0}{\partial x} + \rho_0 w_0 w_0 \frac{\partial w_0}{\partial z} + \rho_0 w_0 u_0 (\frac{\partial w_0}{\partial x} + \frac{\partial u_0}{\partial z}) \\ &+ \rho_0 u_0 \overline{\vec{v_1} \cdot \nabla u_1} + \rho_0 w_0 \overline{\vec{v_1} \cdot \nabla w_1} \\ &= -\vec{v_0} \cdot \nabla p_0 + \vec{v_0} \cdot \overline{\frac{\rho_1}{\rho_0} \nabla p_1} - \rho_0 g w_0, \end{aligned} \tag{4}$$

$$\begin{aligned} &\frac{\partial KE_1}{\partial t} + \rho_0 u_1 \vec{v_1} \cdot \nabla u_0 + \rho_0 u_1 \vec{v_0} \cdot \nabla u_1 + \rho_0 u_1 \vec{v_1} \cdot \nabla u_1 \\ &+ \rho_0 w_1 \vec{v_1} \cdot \nabla w_0 + \rho_0 w_1 \vec{v_0} \cdot \nabla w_1 + \rho_0 w_1 \vec{v_1} \cdot \nabla w_1 \\ &= -\vec{v_1} \cdot \nabla p_1 + \frac{\vec{v_1} \rho_1}{\rho_0} \cdot \nabla p_0 + \frac{\vec{v_1} \rho_1}{\rho_0} \cdot \nabla p_1 \\ &+ \rho_0 u_1 \overline{\vec{v_1} \cdot \nabla u_1} + \rho_0 w_1 \overline{\vec{v_1} \cdot \nabla w_1} - u_1 \overline{\frac{\rho_1}{\rho_0} \frac{\partial p_1}{\partial x}} - w_1 \overline{\frac{\rho_1}{\rho_0} \frac{\partial p_1}{\partial z}}, \end{aligned} \tag{5}$$

where $\vec{v}$ is the wind velocity.

In order to demonstrate the variations in KE across different scale perturbations, proper BPAs must be applied to the tendency equations. Following the principle of triple decomposition, the variables are separated into turbulence, GWs, and BG [*Reynolds and Hussain*, 1972; *Finnigan and Einaudi*, 1981; *Yim et al.*, 2019; *Barbano et al.*, 2022]. The contributions to the energy change rate through different mechanics are analyzed, and the energy transfer among BG, GWs, and turbulence is studied. The triple decomposition for BG, GWs, and turbulence is based on their respective periods. The initial input is a single GW with a period of about 20 minutes. This period of 20 minutes is used to differentiate between the BG and the GWs. In terms of turbulence, there is no well-defined boundary between the GWs and turbulence. Fluctuations with periods less than 3 minutes are considered to be turbulence in this study. The selection of 3 minutes is based on the following considerations. On one hand, this period includes as much turbulence as possible. On the other hand, this study focuses on isotropic turbulence. CGCAM velocity output shows isotropic velocity fluctuations with periods shorter than around 3 minutes. As a result, 3-min averaged data is considered as the background for the turbulence perturbation, which encompasses GW perturbations and the slower varying 20-min averaged data.

During the GW breaking process, nonlinear physical terms play important roles in the energy transfer between different scales. As demonstrated by (5), the instantaneous

KE_1 tendency is related to various nonlinear terms, including flow expansion or compression, the products of perturbation momentum flux and BG shear, advection, and the pressure gradient force doing work. These nonlinear terms are derived to study the energy transfer process among turbulence, GWs, and BG. Linear terms, such as products of linear perturbation variables and BPA nonlinear products, represented by the last four terms in (5), will average to zero when the proper BPAs are applied.

4.3 Instability parameters

Probabilities of dynamic instabilities (PDI) and convective instabilities (PCI) [*Yang and Liu*, 2022] are used to depict the variation of instabilities in the chosen region. PCI and PDI represent the likelihood of occurrences of the negative values of the square of buoyance frequency and the values of Richardson number between 0 and 0.25. Further details can be found in *Yang and Liu* [2022].

5 Results

5.1 KE, IE and PE Conversions during GW breaking process

The KE, IE, and PE changes with respect to time are depicted in Figure 2. The energy changes are calculated as integrals of corresponding energy changes over the specified spatial domain. The blue solid lines in the left, middle, and right plots represent the total KE, IE, and PE variations derived from 2-s-resolution data, respectively. The red solid lines in these three plots depict the total KE, IE, and PE variations after a 20-min moving average with a 1.5-minute step. The vertical black lines mark the 56th minute, which is when the GWs start to break in the chosen region. The background values have been subtracted in IE and PE plots to highlight the variation. Before the start of the GW breaking process, the KE increases by approximately 400 J, while the IE and PE decrease by approximately 3000 J and 5000 J, respectively. The small variation in KE compared to the variations in IE and PE suggests that the energy change is primarily due to energy transport or advection, with the net effect of energy conversion being negligible.

Energy conversion is related to KE tendency. The right-hand side terms of KE tendency are presented in Figure 3. Based on (3), the energy conversion between KE and PE, and KE and IE, $p\nabla\cdot\vec{v}$ and $\rho g W$ are computed. The left plot depicts the energy change due to different physical processes, and the right plot depicts the corresponding energy change

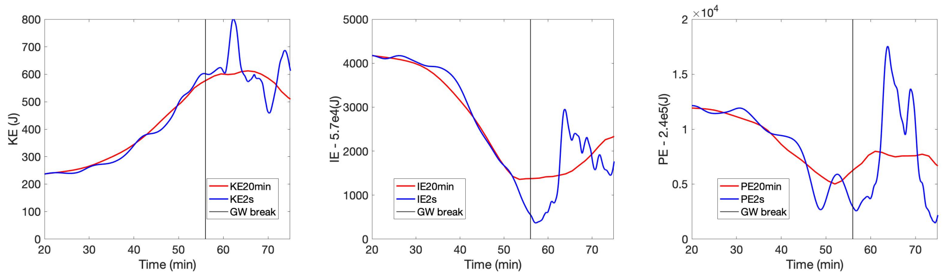

Figure 2: The integrals of KE, IE and PE over the chosen region. The three blue solid lines represent KE, IE, and PE obtained from 2-s resolution data. The three red solid lines show the results after applying 20-min moving averaging with 1.5-min step. GW breaking starts at the 56th minute marked by vertical black solid lines.

rate. The blue dashed line shows the integration of $-\rho g W$, which is the KE change converted from PE. The red dashed line is the KE change due to conversion from IE. The green solid line shows the KE change due to energy transport in the chosen region. The magenta solid line depicts the KE change due to air expansion or compression. During the first 60 minutes, roughly 2500 J of PE is converted into KE. During the same interval, only a limited amount of energy is converted into IE. The primary source of energy changes caused by fluid expansion or compression is from the work performed by the pressure gradient force. The process transported approximately 1500J of energy out of this region. During the period between the 60th and 63rd minutes, about 2500 J of KE is converted to PE, as indicated by the blue dashed line in the left top plot. Around 1500 J of IE is converted into KE, as depicted by the red dashed line in the same plot. During this 5-min interval, there is limited energy change resulting from the pressure gradient force doing work since the energy change by $-\nabla \cdot (p\vec{v})$ is about 1500 J as shown by the magenta solid line in the left top plot. Between the 63rd and 69th minutes, all factors in the right-hand side of KE tendency are relatively small compared with the tendency between 60th and 63rd minutes, and the tendency after the 69th minute. After the 69th minute, the primary source of energy variation caused by fluid expansion is the loss of energy into IE, as depicted by the red dashed line in the right top plot. The main increase of KE is a result of conversion from PE, as shown by the blue dashed line in the same plot.

KE tendency due to KE flux divergence is separated into its horizontal and vertical parts, as shown in the bottom 2 plots in Figure 3. The left plot illustrates the energy

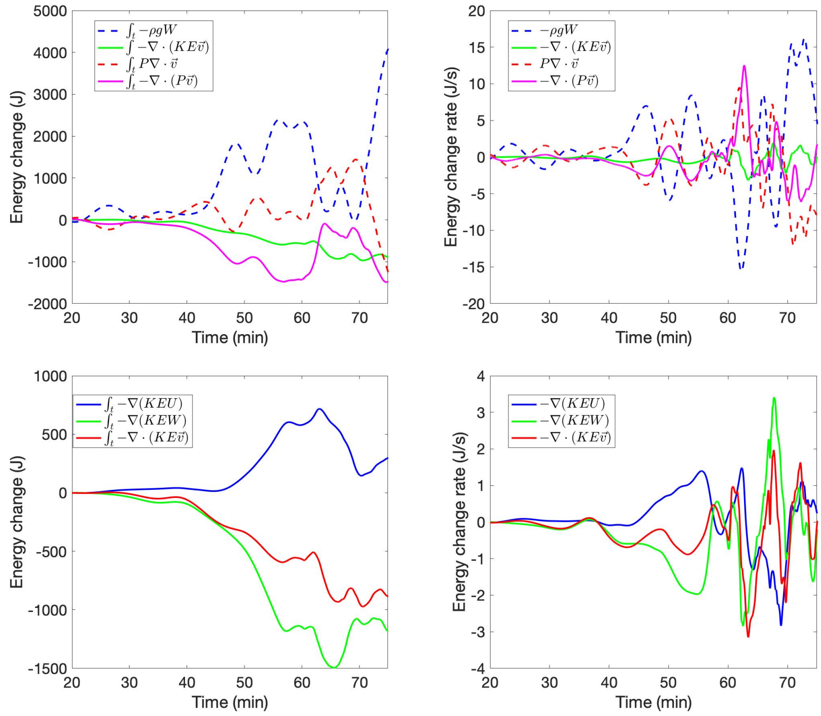

Figure 3: KE change and KE change rate due to forces. The top 2 plots depict the KE change and KE change rate due to conversion and the divergence of KE flux. The bottom 2 plots depict the horizontal and vertical components of KE change and KE change rate due to the divergence of KE flux. The energy changes depicted in the left plots are obtained by integrating the energy change rates over time. The energy change rates displayed in the right plots are obtained through the integration of energy change rates over the selected spatial domain.

change caused by various physical processes, while the right plot shows the corresponding energy change rate. The red solid lines represent the KE change and KE change rate due to the divergence of KE flux. The blue solid lines represent the KE change and KE change rate resulting from KE flux convergence through left and right boundaries. The green solid lines represent the KE change and KE change rate caused by KE divergence flux through the bottom and top boundaries. KE in the chosen region is reduced by approximately 2000 J due to the vertical KE flux, and increased by about 1500 J due to the horizontal KE flux. Prior to the 56th minute, the magnitude of convergence of horizontal KE flux and the divergence of vertical KE flux both increase. During the period from the 56th minute to the 75th minute, the variation is fast and substantial. Between the 70th minute and the 90th minute, the vertical KE flux continues to diverge and the horizontal KE flux continues to converge. After the 90th minute, the divergence or convergence of KE flux is almost negligible. The energy transported by the flux remains unchanged, which suggests the velocity field has been mixed uniformly on a 15km scale. The GW source in the simulation is below the chosen region. At this height region, most energy transport occurs through the horizontal KE flux, which absorbs energy into this region from the left and right boundaries.

5.2 Energy Transfer among BG, GWs, and Turbulence

KE in BG, GW, and turbulence transfer among each other through nonlinear interactions. These interactions play different roles at different times causing KE to vary. In this section, the general variations of KE in BG, GW, and turbulence over the entire GW breaking process are discussed. More detailed analyses are provided for the interval when GW begins to break. KE in 20-minute BG, KE in GW, and KE in turbulence are denoted by KE_0, KE_{GW}, and KE_{turb}, respectively.

5.2.1 Mean Flow KE Tendency

Following (4), the equation for KE_0 tendency is as follows:

$$\begin{aligned} \frac{\partial KE_0}{\partial t} &= -\rho_0 u_0 u_0 \frac{\partial u_0}{\partial x} - \rho_0 w_0 w_0 \frac{\partial w_0}{\partial z} \\ &-\rho_0 w_0 u_0 \left(\frac{\partial w_0}{\partial x} + \frac{\partial u_0}{\partial z}\right) \\ &-\rho_0 u_0 \overline{\vec{v_1} \cdot \nabla u_1}^{20\text{min}} - \rho_0 w_0 \overline{\vec{v_1} \cdot \nabla w_1}^{20\text{min}} \\ &-\vec{v_0} \cdot \nabla p_0 + \vec{v_0} \cdot \overline{\frac{\rho_1}{\rho_0} \nabla p_1}^{20\text{min}} - \rho_0 g w_0. \end{aligned} \tag{6}$$

KE_0 change can be examined by integrating over time. The energy changes are calculated as the integrals of energy change rates over time. The energy change rates are obtained by integrating the energy change rates over the selected spatial domain. In (6), $-\rho_0 u_0 u_0 \frac{\partial u_0}{\partial x} - \rho_0 w_0 w_0 \frac{\partial w_0}{\partial z}$ is the KE_0 change due to BG air expansion or compression. $-\rho_0 w_0 u_0 (\frac{\partial w_0}{\partial x} + \frac{\partial u_0}{\partial z})$ is the KE_0 change due to BG wind shear. $-\rho_0 u_0 \overline{\vec{v_1} \cdot \nabla u_1}^{20\text{min}} - \rho_0 w_0 \overline{\vec{v_1} \cdot \nabla w_1}^{20\text{min}}$ depicts how BG changes due to nonlinear interactions of perturbations. $-\vec{v_0} \cdot \nabla p_0$ and $-\rho_0 g w_0$ depict the work by pressure gradient force and gravity force, respectively. $\vec{v_0} \cdot \overline{\frac{\rho_1}{\rho_0} \nabla p_1}^{20\text{min}}$ depicts the perturbation pressure gradient averaged effect on KE_0 change, which is another form of nonlinear interaction of perturbations.

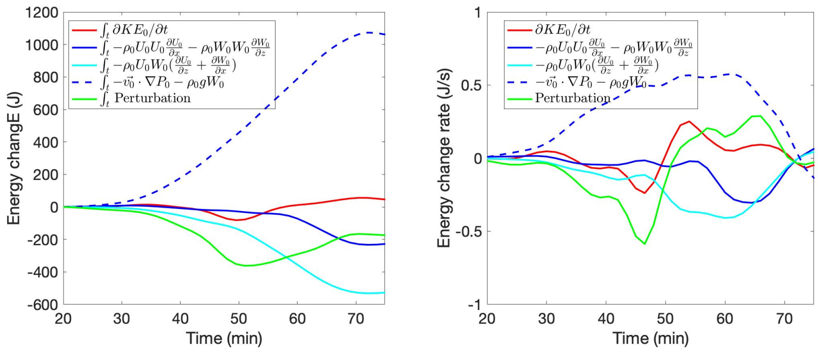

Figure 4: KE_0 change and change rate over the chosen domain. The left plot is the integration of force terms for KE_0 change rate. The right plot is the work done by force terms for KE_0 change. The energy changes depicted in the left plot are obtained by integrating the energy change rates over time. The energy change rates displayed in the right plot are obtained through the integration of energy change rates over the selected spatial domain.

The KE_0 change and change rate are shown in Figure 4. The energy changes depicted in the left plots are obtained by integrating the energy change rates over time. The energy change rates displayed in the right plots are obtained through the integration of energy change rates over a selected spatial domain. The energy changes caused by various mechanisms are described as follows. The evolution of KE_0 is depicted by the red solid line in the left plot. It decreases first and then increases slightly by about 180 J at the end. The only positive contribution to KE_0 comes from the work done by the pressure gradient force and gravity force, as shown by the blue dashed line. On the other hand, the blue solid line, which represents the expansion and compression of the flow, has a negative effect on KE_0. This indicates that the flow is expanding and transporting KE_0 out of the chosen domain. The cyan solid line depicts the product of BG momentum flux and BG wind shear. In general, this term is negative, meaning that the momentum flux and wind shear have the same sign. This process transports flow with smaller/larger momentum to the position of flow with larger/smaller momentum, making the velocity field more uniform and reducing the KE_0. Before the 50th minute, a few minutes before the GW breaking, the averaged nonlinear interactions reduce KE_0, as shown by the green solid line. After GW breaking and turbulence develop, the nonlinear terms have a positive contribution to KE_0 till the 75th minute. The same line types in the right plot depict the corresponding energy change rates.

5.2.2 Perturbation KE Tendency

KE in perturbation (KE_1) here includes KE in turbulence (KE_{turb}) and GWs (KE_{GW}). The background value is a 20-min average background. To accurately capture turbulence fluctuations, a 2-second resolution was used for the data analysis.

$$\begin{aligned}\frac{\partial KE_1}{\partial t} &= -\rho_0 u_1 u_1 \frac{\partial u_0}{\partial x} - \rho_0 w_1 w_1 \frac{\partial w_0}{\partial z} - \rho_0 w_1 u_1 (\frac{\partial w_0}{\partial x} + \frac{\partial u_0}{\partial z}) \\ &-\vec{v} \cdot \nabla KE_1 + \frac{\vec{v_1}\rho_1}{\rho_0} \cdot \nabla p_0 + \frac{(\rho_1 - \rho_0)\vec{v_1}}{\rho_0} \cdot \nabla p_1 \\ &+\rho_0 u_1 \overline{\vec{v_1} \cdot \nabla u_1}^{20\text{min}} + \rho_0 w_1 \overline{\vec{v_1} \cdot \nabla w_1}^{20\text{min}} \\ &-u_1 \overline{\frac{\rho_1}{\rho_0}\frac{\partial p_1}{\partial x}}^{20\text{min}} - w_1 \overline{\frac{\rho_1}{\rho_0}\frac{\partial p_1}{\partial z}}^{20\text{min}},\end{aligned} \tag{7}$$

Perturbation Q_1 can be separated into Q_{turb} and Q_{GW}. This allows for an investigation of the variations in both the KE_{turb} and KE_{GW}.

Turbulence KE

The 2 s-resolution data and 3-min BPA is utilized in this study to analyze the turbulence energy and its interaction with GWs and BG. The equation for turbulence is the same as for total perturbation, but the BG for turbulence in this equation is 3 min-resolution data, which includes GWs. The total BG for turbulence (Q_0) is separated into two components: Q_{GW} and Q_{BG}. This allows for the examination of the interactions between turbulence (Q_{turb}) and the BG (Q_{BG}), as well as between turbulence and GWs (Q_{GW}).

$$
\begin{aligned}
\frac{\partial KE_1}{\partial t} = & -\rho_0 u_1 u_1 \frac{\partial u_0}{\partial x} - \rho_0 w_1 w_1 \frac{\partial w_0}{\partial z} - \rho_0 w_1 u_1 (\frac{\partial w_0}{\partial x} + \frac{\partial u_0}{\partial z}) \\
& - \vec{v} \cdot \nabla KE_1 + \frac{\vec{v_1}\rho_1}{\rho_0} \cdot \nabla p_0 + \frac{(\rho_1 - \rho_0)\vec{v_1}}{\rho_0} \cdot \nabla p_1 \\
& + \rho_0 u_1 \overline{\vec{v_1} \cdot \nabla u_1}^{3\text{min}} + \rho_0 w_1 \overline{\vec{v_1} \cdot \nabla w_1}^{3\text{min}} \\
& - u_1 \overline{\frac{\rho_1}{\rho_0} \frac{\partial p_1}{\partial x}}^{3\text{min}} - w_1 \overline{\frac{\rho_1}{\rho_0} \frac{\partial p_1}{\partial z}}^{3\text{min}},
\end{aligned}
\tag{8}
$$

where the symbol $\overline{Q}^{3\text{min}}$ denotes the 3-minute BPA. To simplify the problem, ρ_1 is assumed to be much smaller than ρ_0. Therefore, $\rho_1 + \rho_0 \sim \rho_0$ and $(\rho_0 - \rho_1)/\rho_0 \sim 1$.

$$
\begin{aligned}
\frac{\partial KE_{turb}}{\partial t} = & -\rho_0 u_{turb}^2 \frac{\partial (u_{GW} + u_0)}{\partial x} - \rho_0 w_{turb}^2 \frac{\partial (w_{GW} + w_0)}{\partial z} \\
& - \rho_0 w_{turb} u_{turb} (\frac{\partial (w_{GW} + w_0)}{\partial x} + \frac{\partial (u_{GW} + u_0)}{\partial z}) \\
& - (\vec{v_{turb}} + \vec{v_{GW}} + \vec{v_0}) \cdot \nabla KE_{turb} + \frac{\vec{v_{turb}}\rho_{turb}}{\rho_0} \cdot \nabla (p_{GW} + p_0) - \vec{v_{turb}} \cdot \nabla p_{turb} \\
& + \rho_0 u_{turb} \overline{\vec{v_{turb}} \cdot \nabla u_{turb}}^{3\text{min}} + \rho_0 w_{turb} \overline{\vec{v_{turb}} \cdot \nabla w_{turb}}^{3\text{min}} \\
& - u_{turb} \overline{\frac{\rho_{turb}}{\rho_0} \frac{\partial p_{turb}}{\partial x}}^{3\text{min}} - w_{turb} \overline{\frac{\rho_{turb}}{\rho_0} \frac{\partial p_{turb}}{\partial z}}^{3\text{min}},
\end{aligned}
\tag{9}
$$

Do 3-minute BPA on the KE_{turb} tendency equation and remove the terms averaged to zero yields

$$
\begin{aligned}
\overline{\frac{\partial KE_{turb}}{\partial t}}^{3\text{min}} = & -\rho_0 \overline{u_{turb}^2 \frac{\partial (u_{GW} + u_0)}{\partial x}}^{3\text{min}} - \rho_0 \overline{w_{turb}^2 \frac{\partial (w_{GW} + w_0)}{\partial z}}^{3\text{min}} \\
& - \rho_0 \overline{w_{turb} u_{turb}}^{3\text{min}} (\frac{\partial (w_{GW} + w_0)}{\partial x} + \frac{\partial (u_{GW} + u_0)}{\partial z}) \\
& - \overline{(\vec{v_{turb}} + \vec{v_{GW}} + \vec{v_0}) \cdot \nabla KE_{turb}}^{3\text{min}} \\
& + \overline{\frac{\vec{v_{turb}}\rho_{turb}}{\rho_0}}^{3\text{min}} \cdot \nabla (p_{GW} + p_0) - \overline{\vec{v_{turb}} \cdot \nabla p_{turb}}^{3\text{min}}.
\end{aligned}
\tag{10}
$$

The last 4 terms in (9) averages to zero ideally theoretically. However, in the practical calculation, these 4 terms do not average to zero because the separation among different time scales cannot be clear-cut. In (10), $-\rho_0 \overline{u_{turb}^2 \frac{\partial (u_{GW}+u_0)}{\partial x}}^{3\text{min}} - \rho_0 \overline{w_{turb}^2 \frac{\partial (w_{GW}+w_0)}{\partial z}}^{3\text{min}}$ represents the KE_{turb} change rate due to GW and BG flow expansion or compression. GW and BG flow expansion or compression result in a redistribution of KE_{turb}. $-\rho_0 \overline{w_{turb} u_{turb}}^{3\text{min}} (\frac{\partial (w_{GW}+w_0)}{\partial x} + \frac{\partial (u_{GW}+u_0)}{\partial z})$ represents the KE_{turb} change rate due to GW and BG wind shear. $-\overline{(\vec{v_{GW}} + \vec{v_0}) \cdot \nabla KE_{turb}}^{3\text{min}}$ depicts the KE_{turb} change rate due to GW and BG wind transport KE_{turb} into or out of the chosen region. $\overline{\frac{\vec{v_{turb}}\rho_{turb}}{\rho_0}}^{3\text{min}} \cdot \nabla (p_{GW} + p_0)$ depicts the KE_{turb} change rate due to GW and BG pressure gradients or buoyancy terms. All the terms discussed above are related to interactions between turbulence and its background. $-\overline{(\vec{v_{turb}}) \cdot \nabla KE_{turb}}^{3\text{min}}$ and $-\overline{\vec{v_{turb}} \cdot \nabla p_{turb}}^{3\text{min}}$ are turbulence self-interactions. Self-interactions of perturbations may both strengthen or weaken the perturbation. These two processes are referred to as "self-strengthening" and "self-weakening," respectively.

GW-turbulence interactions generally result in a decrease in the KE_{turb} during the GW-breaking process. As illustrated in the middle 2 plots in Figure 5, in the left plot, the red solid line depicts the KE_{turb} increased by about 70 J due to redistribution of KE_{turb} by GWs. The blue solid line depicts the KE_{turb} lost approximately 170 J through the interaction of turbulence momentum flux and GW wind shear. The cyan line depicts a loss of about 120 J in KE_{turb} through advection caused by the velocity of GWs. The green solid line shows that the change in KE_{turb} due to the pressure gradient force of the GWs acting on the turbulence velocity is approximately zero. Turbulence loses about 220 J into GWs during the GW-breaking process.

After GWs begin to break, the increase in KE_{turb} is primarily due to BG-turbulence interactions. As shown in the bottom two plots in Figure 5, the left plot depicts the energy change due to different physical processes, while the right plot shows the corresponding energy change rate. The energy changes are obtained by integrating the rates of change over time, while the rates of change are obtained by integrating over a chosen spatial domain. In the left plot, the red solid line indicates that KE_{turb} increased by about 10 J due to the redistribution of KE_{turb} by BG flow. The blue solid line depicts that KE_{turb} lost approximately 110 J through the interaction of turbulence momentum flux and BG wind shear. The cyan line depicts that KE_{turb} continues to gain energy through advection due to BG velocity, resulting in a gain of approximately 100 J. The green solid line shows the KE_{turb} change and change rate through BG pressure gradient force doing work on turbulence velocity. This process decreases the KE_{turb} before GW breaking. However, after GW starts to break, the BG pressure gradient force or the buoyant force increases the KE_{turb} by approximately 300 J.

Self-interactions of turbulence play a crucial role in the variability of KE_{turb}. As shown in the top two plots in Figure 5, KE_{turb} starts to grow rapidly after the 56th minute when GW starts to break. Advection of KE_{turb} by turbulence velocity starts to decrease KE_{turb} around the 60th minute, as depicted by the blue lines. Turbulence pressure gradient along with turbulence velocity causes a decrease in KE_{turb} from the 56th to 65th minute and increases KE_{turb} after the 65th minute, as shown by the cyan lines.

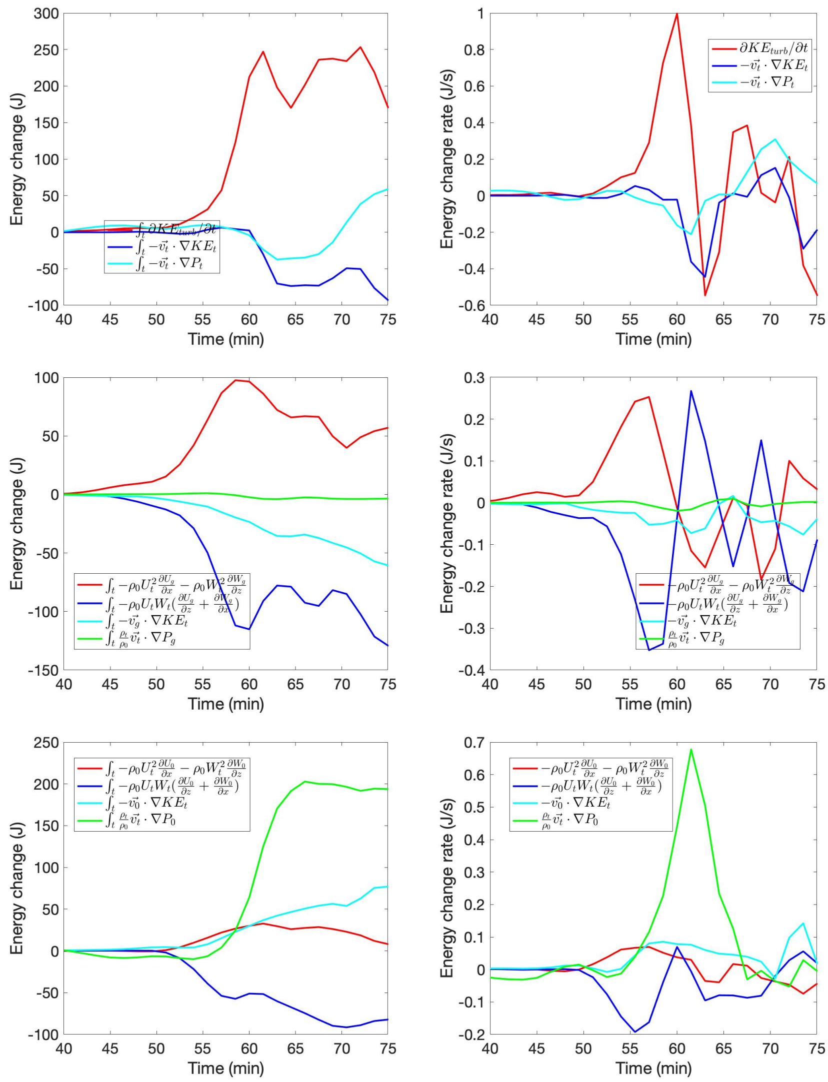

Figure 5: KE_{turb} change and change rate through different physical processes. The energy changes depicted in the left plots are obtained by integrating the energy change rates over time. The energy change rates displayed in the right plots are obtained through the integration of energy change rates over the selected spatial domain.

Gravity Wave KE

KE in perturbations with 20-min BPA BG and KE in turbulence with 3-min BPA BG were deducted in this section. Their difference represents the tendency of KE in GWs. Rewrite (7),

$$\begin{aligned}
\frac{\partial(KE_{turb}+KE_{GW})}{\partial t} &= -\rho_0(u_{GW}+u_{turb})(u_{GW}+u_{turb})\frac{\partial u_0}{\partial x} \\
&-\rho_0(w_{GW}+w_{turb})(w_{GW}+w_{turb})\frac{\partial w_0}{\partial z} \\
&-\rho_0(w_{GW}+w_{turb})(u_{GW}+u_{turb})(\frac{\partial w_0}{\partial x}+\frac{\partial u_0}{\partial z}) \\
&-\vec{v}\cdot\nabla(KE_{turb}+KE_{GW}) \\
&+\frac{(\vec{v_{GW}}+\vec{v_{turb}})(\rho_{turb}+\rho_{GW})}{\rho_0}\cdot\nabla p_0-(\vec{v_{GW}}+\vec{v_{turb}})\cdot\nabla(p_{GW}+p_{turb}) \\
&+\rho_0(u_{GW}+u_{turb})\overline{(\vec{v_{GW}}+\vec{v_{turb}})\cdot\nabla(u_{GW}+u_{turb})}^{20\text{min}} \\
&+\rho_0(w_{GW}+w_{turb})\overline{(\vec{v_{GW}}+\vec{v_{turb}})\cdot\nabla(w_{GW}+w_{turb})}^{20\text{min}} \\
&-(u_{GW}+u_{turb})\overline{\frac{(\rho_{turb}+\rho_{GW})}{\rho_0}\frac{\partial(p_{GW}+p_{turb})}{\partial x}}^{20\text{min}} \\
&-(w_{GW}+w_{turb})\overline{\frac{(\rho_{turb}+\rho_{GW})}{\rho_0}\frac{\partial(p_{GW}+p_{turb})}{\partial z}}^{20\text{min}},
\end{aligned} \tag{11}$$

where the symbol $\overline{Q}^{20\text{min}}$ denotes the 20-minute BPA. Subtract (9) from (11).

$$\begin{aligned}
\frac{\partial KE_{GW}}{\partial t} &= -\rho_0(u_{GW}^2+2u_{turb}u_{GW})\frac{\partial u_0}{\partial x}+\rho_0u_{turb}^2\frac{\partial u_{GW}}{\partial x} \\
&-\rho_0(w_{GW}^2+2w_{turb}w_{GW})\frac{\partial w_0}{\partial z}+\rho_0w_{turb}^2\frac{\partial w_{GW}}{\partial z} \\
&-\rho_0w_{GW}u_{GW}(\frac{\partial w_0}{\partial x}+\frac{\partial u_0}{\partial z})-\rho_0(w_{turb}u_{GW}+w_{GW}u_{turb})(\frac{\partial w_0}{\partial x}+\frac{\partial u_0}{\partial z}) \\
&+\rho_0w_{turb}u_{turb}(\frac{\partial w_{GW}}{\partial x}+\frac{\partial u_{GW}}{\partial z})-\vec{v}\cdot\nabla KE_{GW} \\
&+\frac{(\vec{v_{GW}}\rho_{GW}+\vec{v_{GW}}\rho_{turb}+\vec{v_{turb}}\rho_{GW})}{\rho_0}\cdot\nabla p_0-\frac{\vec{v_{turb}}\rho_{turb}}{\rho_0}\cdot\nabla p_{GW} \\
&-\vec{v_{GW}}\cdot\nabla p_{GW}-\vec{v_{turb}}\cdot\nabla p_{GW}-\vec{v_{GW}}\cdot\nabla p_{turb} \\
&+\rho_0(u_{GW}+u_{turb})\overline{(\vec{v_{GW}}+\vec{v_{turb}})\cdot\nabla(u_{GW}+u_{turb})}^{20\text{min}} \\
&+\rho_0(w_{GW}+w_{turb})\overline{(\vec{v_{GW}}+\vec{v_{turb}})\cdot\nabla(w_{GW}+w_{turb})}^{20\text{min}} \\
&-(u_{GW}+u_{turb})\overline{\frac{(\rho_{turb}+\rho_{GW})}{\rho_0}\frac{\partial(p_{GW}+p_{turb})}{\partial x}}^{20\text{min}} \\
&-(w_{GW}+w_{turb})\overline{\frac{(\rho_{turb}+\rho_{GW})}{\rho_0}\frac{\partial(p_{GW}+p_{turb})}{\partial z}}^{20\text{min}} \\
&-\rho_0u_{turb}\overline{\vec{v_{turb}}\cdot\nabla u_{turb}}^{3\text{min}}-\rho_0w_{turb}\overline{\vec{v_{turb}}\cdot\nabla w_{turb}}^{3\text{min}} \\
&+u_{turb}\overline{\frac{\rho_{turb}}{\rho_0}\frac{\partial p_{turb}}{\partial x}}^{3\text{min}}+w_{turb}\overline{\frac{\rho_{turb}}{\rho_0}\frac{\partial p_{turb}}{\partial z}}^{3\text{min}}.
\end{aligned} \tag{12}$$

Averaging the equation over 20-min intervals and removing the linear terms that averaged to zero yields

$$
\begin{aligned}
\frac{\partial \overline{KE_{GW}}^{\text{20min}}}{\partial t} &= -\rho_0 \overline{(u_{GW}^2 + 2u_{turb}u_{GW})}^{\text{20min}} \frac{\partial u_0}{\partial x} + \rho_0 \overline{u_{turb}^2 \frac{\partial u_{GW}}{\partial x}}^{\text{20min}} \\
& -\rho_0 \overline{(w_{GW}^2 + 2w_{turb}w_{GW})}^{\text{20min}} \frac{\partial w_0}{\partial z} + \rho_0 \overline{w_{turb}^2 \frac{\partial w_{GW}}{\partial z}}^{\text{20min}} \\
& -\rho_0 \overline{w_{GW}u_{GW}}^{\text{20min}} \left(\frac{\partial w_0}{\partial x} + \frac{\partial u_0}{\partial z}\right) - \rho_0 \overline{(w_{turb}u_{GW} + w_{GW}u_{turb})}^{\text{20min}} \left(\frac{\partial w_0}{\partial x} + \frac{\partial u_0}{\partial z}\right) \\
& +\rho_0 \overline{w_{turb}u_{turb}\left(\frac{\partial w_{GW}}{\partial x} + \frac{\partial u_{GW}}{\partial z}\right)}^{\text{20min}} - \overline{\vec{v} \cdot \nabla KE_{GW}}^{\text{20min}} \\
& + \frac{\overline{(\vec{v_{GW}}\rho_{GW} + \vec{v_{GW}}\rho_{turb} + \vec{v_{turb}}\rho_{GW})}^{\text{20min}}}{\rho_0} \cdot \nabla p_0 - \overline{\frac{\vec{v_{turb}}\rho_{turb}}{\rho_0} \cdot \nabla p_{GW}}^{\text{20min}} \\
& -\overline{\vec{v_{GW}} \cdot \nabla p_{GW}}^{\text{20min}} - \overline{\vec{v_{turb}} \cdot \nabla p_{GW}}^{\text{20min}} - \overline{\vec{v_{GW}} \cdot \nabla p_{turb}}^{\text{20min}} \\
& -\rho_0 \overline{u_{turb} \overline{\vec{v_{turb}} \cdot \nabla u_{turb}}^{\text{3min}}}^{\text{20min}} - \rho_0 \overline{w_{turb} \overline{\vec{v_{turb}} \cdot \nabla w_{turb}}^{\text{3min}}}^{\text{20min}} \\
& + \overline{u_{turb} \overline{\frac{\rho_{turb}}{\rho_0} \frac{\partial p_{turb}}{\partial x}}^{\text{3min}}}^{\text{20min}} + \overline{w_{turb} \overline{\frac{\rho_{turb}}{\rho_0} \frac{\partial p_{turb}}{\partial z}}^{\text{3min}}}^{\text{20min}} .
\end{aligned} \tag{13}
$$

The 4 terms in (12) are expected to average to zero when using 20-minute averages, but in the practice, this is not always the case due to the difficulty in clearly distinguishing between different time scales. In (13), $-\rho_0 \overline{u_{GW}^2}^{\text{20min}} \frac{\partial u_0}{\partial x} - \rho_0 \overline{w_{GW}^2}^{\text{20min}} \frac{\partial w_0}{\partial z}$ is the KE_{GW} change rate due to BG flow expansion or compression, also referred to as the redistribution of KE_{GW} by BG. $-\rho_0 \overline{w_{GW}u_{GW}}^{\text{20min}} (\frac{\partial w_0}{\partial x} + \frac{\partial u_0}{\partial z})$ is the KE_{GW} change rate resulting from the interaction of GW momentum flux and BG wind shear. $-\overline{\vec{v_0} \cdot \nabla KE_{GW}}^{\text{20min}}$ is the transportation of KE_{GW} caused by the BG wind. $\frac{\overline{\vec{v_{GW}}\rho_{GW}}^{\text{20min}}}{\rho_0} \cdot \nabla p_0$ depicts the KE_{GW} change rate due to BG pressure gradient or buoyancy term. The terms above are categorized as BG-GW interactions. $-\overline{\vec{v_{GW}} \cdot \nabla KE_{GW}}^{\text{20min}}$ and $-\overline{\vec{v_{GW}} \cdot \nabla p_{GW}}^{\text{20min}}$ depict the effect on KE_{GW} change rate from GW self-interactions. $\rho_0 \overline{u_{turb}^2 \frac{\partial u_{GW}}{\partial x}}^{\text{20min}}$ + $\rho_0 \overline{w_{turb}^2 \frac{\partial w_{GW}}{\partial z}}^{\text{20min}}$ depicts the KE_{GW} change rate due to GW redistributing turbulence. $\rho_0 \overline{w_{turb}u_{turb}(\frac{\partial w_{GW}}{\partial x} + \frac{\partial u_{GW}}{\partial z})}^{\text{20min}}$ represents the KE_{GW} change rate due to interactions of GW wind shear and turbulence momentum flux. $-\overline{\vec{v_{turb}} \cdot \nabla KE_{GW}}^{\text{20min}}$ shows the effects on KE_{GW} change rate due to the averaged effect of turbulence transporting KE_{GW}. $-\overline{\frac{\vec{v_{turb}}\rho_{turb}}{\rho_0} \cdot \nabla p_{GW}}^{\text{20min}}$, $-\overline{\vec{v_{turb}} \cdot \nabla p_{GW}}^{\text{20min}}$ and $-\overline{\vec{v_{GW}} \cdot \nabla p_{turb}}^{\text{20min}}$ depict the KE_{GW} change rate due to buoyancy force of GW and turbulence, acting on turbulence or GW perturbations, respectively. The terms discussed above are grouped as GW-turbulence interactions. The remaining terms in (13) are grouped as BG-GW-turbulence interactions because they involve variables from BG, GWs, and turbulence in their mathematical expressions. These terms reflect the complex interplay related to the three different scales.

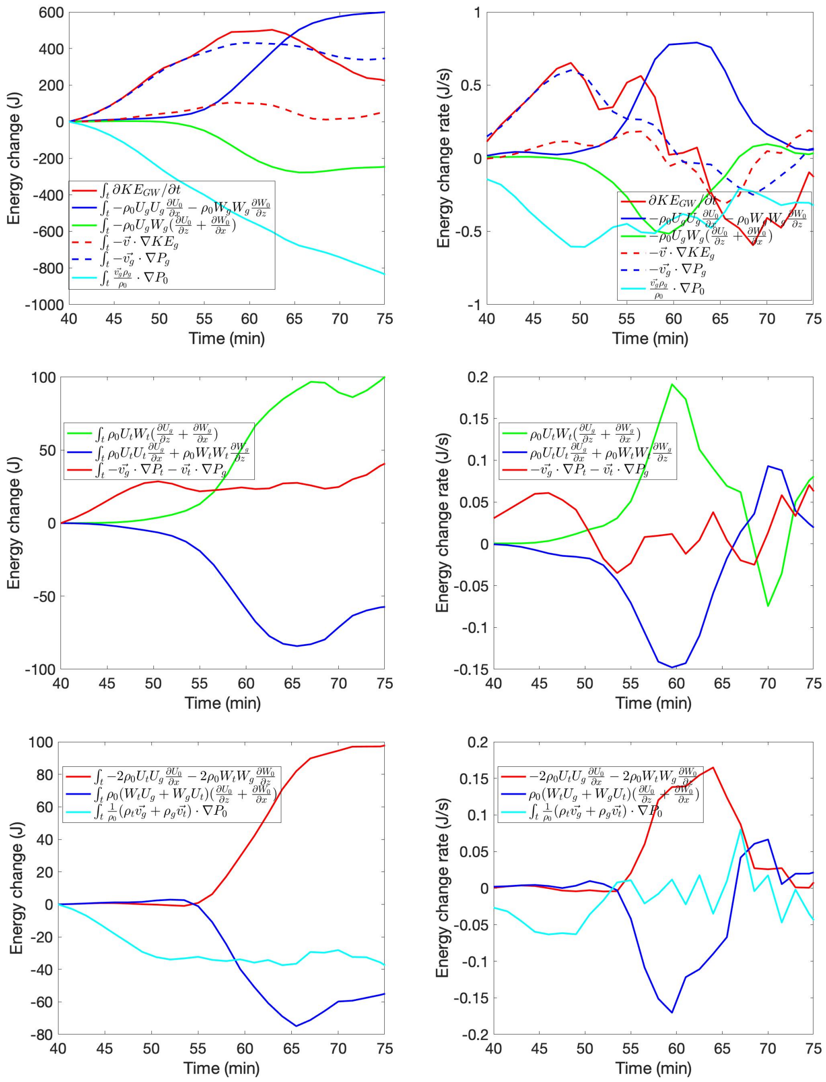

Figure 6: KE_{GW} change and change rate due to GW and BG interactions over the spatial domain. The left plot depicts the energy change due to different physical processes, and the right plot depicts the corresponding energy change rate. The energy changes depicted in the left plots are obtained by integrating the energy change rates over time. The energy change rates displayed in the right plots are obtained through the integration of energy change rates over the selected spatial domain.

Interactions between BG and GWs, such as KE_{GW} advection, redistribution of KE_{GW} by BG, KE_{GW} transportation by BG, GW self-strengthening, and other BG-GW interactions play the dominant role in the evolution of KE_{GW}. The changes in KE_{GW} and the change rates resulting from interactions between BG and GWs are shown in the top 2 plots of Figure 6. The energy changes depicted in the left plots are obtained by integrating the energy change rates over time. The energy change rates displayed in the right plots are obtained through the integration of energy change rates over the selected spatial domain. The red solid line shows that KE_{GW} increases from the start and reaches its maximum value at the 56th minute. After that, gravity wave breaking begins and KE_{GW} decreases. The blue solid lines in the top plots depict the redistribution of KE_{GW} by BG. After the GW starts to break, BG redistributes more energy into the chosen region. The redistribution stopped shortly after turbulence fully developed around the 73rd minute, after which the energy change due to redistribution remains constant. The green solid line in the left top plot represents the energy transfer between GWs and BG through the interaction of GW momentum flux and BG wind shear. The green line is negative, which indicates that GW is losing KE to BG. This mechanism starts to impact the KE_{GW} when GW begins to break. During GW breaks, GW loses about 220 J energy to BG through this interaction. GW advection slightly increased KE_{GW} before GW starts to break, as shown by the red dashed lines in the top two plots. Before GW starts to break, the main increase of KE_{GW} is due to the nonlinear interaction of GW velocity and GW pressure gradient force, as shown by the blue dashed lines in the top two plots. GW self-strengthening contributes to the increase of KE_{GW} before GW breaking. BG pressure gradient power decreases KE_{GW} in the chosen region, as shown by the cyan solid lines in the top two plots, starting before GWs start to break.

The role of turbulence in the alteration of KE_{GW} is significant. Both direct interactions between GWs and turbulence and the interactions between the BG, GWs, and turbulence contribute roughly equally to the rate of change in KE_{GW}. The KE_{GW} changes and change rate due to GW-turbulence interactions are presented in the middle 2 plots in Figure 6. The bottom 2 plots in the same figure display the changes and change rates in KE_{GW} due to BG-GW-turbulence interactions. The energy changes depicted in the left plots are obtained by integrating the energy change rates over time. The energy change rates displayed in the right plots are obtained through the integration of energy change rates over the selected spatial domain.

In general, GW-turbulence interactions increase KE_{GW}, while BG-GW-turbulence interactions decrease KE_{GW}. As shown by the green line in the middle 2 plots in Figure 6, the interaction between the turbulence momentum flux and the GW wind shear results in an increase in the GW wind shear, leading to a rise in KE_{GW} after the GW breaks. This is comparable to the process in which the GW momentum flux transfers its KE GW into the BG wind shear, as illustrated by the green line in the top two plots in Figure 6. Before GWs break, GW KE increases through turbulence pressure gradient force doing work shown by the red solid line in the middle 2 plots in Figure 6. BG expansion or compression interacts with GW and turbulence momentum flux increase the KE_{GW} during the turbulence developing process shown by the red solid line in the bottom 2 plots in Figure 6. The blue solid lines in the middle 2 plots depict that BG wind shear interacts with GW and turbulence momentum flux decrease the KE_{GW} during the 5-minute interval of the turbulence developing process.

BG-GW-turbulence interactions generally decreases KE_{GW}. Before turbulence develops, the three component interactions decrease KE_{GW}, transferring energy into BG. GW energy loses to BG. After GW starts to break, GW energy is transferred into turbulence and BG. About 230J KE is transferred from turbulence into GW at the end from KE_{turb} tendency as shown in the left middle plot in Figure 5. About 220J energy is transferred from turbulence into GW as shown in Figure 6. So most of the energy transferred by BG-GW-turbulence interactions finally goes into BG.

5.2.3 GW and Turbulence KE Tendencies During Turbulence Development

A closer examination of the period between the 56th and 65th minutes, when the gravity wave breaks and turbulence develops, is insightful. 2-s resolution KE_{turb} and KE_{GW} change and change rate are presented between the 56th minute and 65th minute when the GWs start to break and turbulence starts to develop. The energy changes due to various physical processes are presented in Figure 7. It is not necessary to display the 2-second resolution energy change and energy change rate of KE_0 as it only relates to low-frequency (period $\geq$ 20 minutes) variables or the 20-minute averaged effect of high-frequency perturbations (turbulence and GWs, period < 20 minutes).

From the 50th to the 58th minute, the growth rate of KE_{turb} is relatively slow, as depicted by the solid red lines in the top two plots of Figure 7. During this 8-min inter-

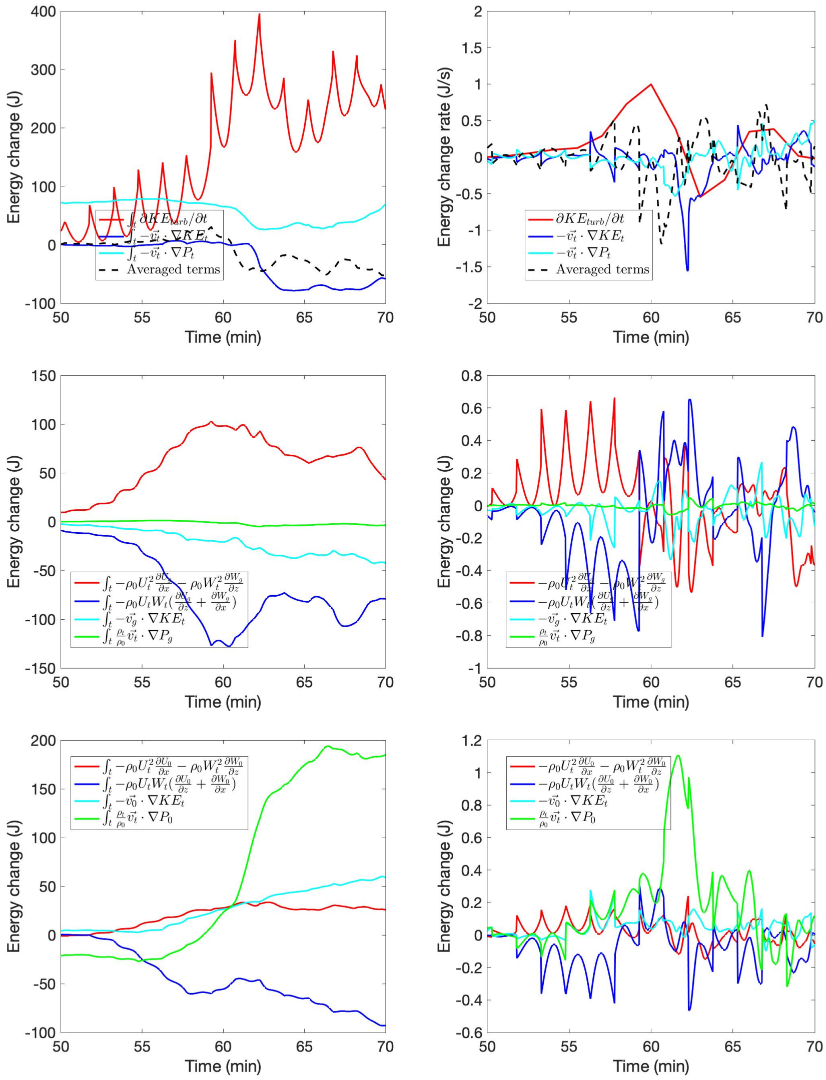

Figure 7: KE_{turb} change and change rate between the 50th minute and 70the minute. The left plot depicts the energy change due to different physical processes, and the right plot depicts the corresponding energy change rate. The energy changes depicted in the left plots are obtained by integrating the energy change rates over time. The energy change rates displayed in the right plots are obtained through the integration of energy change rates over the selected spatial domain.

val, the main factor contributing to the growth of KE_{turb} is the redistribution by gravity waves, as shown in the plot on the middle right. This 8-min interval is referred to as turbulence growth phase 1. The maximum value of turbulence KE_{turb} is reached 5 minutes after the 58th minute. This 5-minute period is referred to as turbulence growth phase 2. Before GWs break, the interaction of turbulence momentum flux and wind shear decreases KE_{turb}, as shown by the blue solid lines in the middle two plots of Figure 7. However, the GW redistribution increases KE_{turb}, as depicted by the red solid line in the same two plots. The combined effect from GW-turbulence interaction increases KE_{turb} before GWs break. After the breaking of GWs, turbulence starts to grow rapidly. However, the combined effect of GW-turbulence interaction decreases KE_{turb}. Turbulence mainly absorbs KE through BG-turbulence interactions, especially in the last 2 minutes when turbulence is at its strongest, as indicated by the green solid line in the bottom two plots in Figure 7. The primary driver of the BG-turbulence interactions that drive turbulence growth is the BG buoyant force acting on turbulence velocity.

5.3 Instabilities and GW-breaking

During the GW breaking period, instabilities play a significant role in the generation of turbulence. Instabilities are closely associated with GW breaking and the generation of turbulence. At the 46th minute, instabilities begin to emerge in the chosen region, as shown in Figure 8. Probabilities of instabilities reach their maximum at around the 70th minute.

PCI is closely linked to the GW breaking process. Between the 54th minute and 58th minute, both PCI and PDI rise along with KE_{GW} increases. However, between the 58th minute and 62nd minute, PCI drops approximately 8 percentage points along with the growth of KE_{turb}. Subsequently, from the 62nd to the 64th minute, as the KE_{turb} decreases by 150 J, as shown in the top left plot in Figure 7, the PCI increases by approximately 8 percentage points. Instabilities can result from large temperature gradients and wind shear introduced by GWs.

6 Discussion

The mechanisms of energy convergence during various stages of gravity wave breaking are distinct. Before the turbulence growth phase 2 and prior to the saturation of GWs

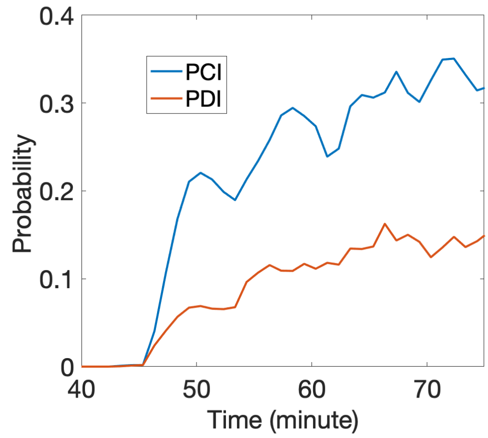

Figure 8: PCI and PDI in the chosen region. The blue lines depict the probability of convective instability. The red lines depict the probability of dynamic instability.

(around the 58th minute), the work done by the gravity force on vertical motion and the convergence of pressure flux due to flow expansion/compression balance each other, as demonstrated in the top two plots in Figure 3. On average, the work done by pressure is the dominant factor in the convergence of pressure flux before GW breaking begins, as indicated by the magenta solid line in the top left plot of Figure 3. The IE-KE conversion is through flow oscillations along with expansion/compression. The blue and red dashed lines in the top right plot of Figure 3 demonstrate that the magnitude of energy conversion from KE to IE is comparable to that from PE to KE, but with opposite signs. However, the converted IE is almost zero during the first 58 minutes. Prior to the breaking or dissipation of GWs, the energy conversion in the flow is an adiabatic process, and on average over the BG period, there is no conversion between mechanical energy and IE. During turbulence growth phase 2 and GW saturation interval (between the 58th and 62nd minute), KE_{GW} stays constant while KE_{turb} increases to its maximum. KE starts to be converted to PE, as indicated by the blue dashed line in the right top plot in Figure 3. Meanwhile, more IE starts to be converted to KE, as shown by the red dashed line in the right top plot in Figure 3. A possible dynamic is that as GW is about to break, the flow keeps expanding when the GW propagates upward, which increases the KE and maintains momentum conservation.

The relationship between wave energy deposition and turbulent dissipation has been suggested in previous studies [*Becker and Schmitz*, 2002]. In our simulation, before the onset of turbulence, there is limited energy deposition occurs, not only in the case of conservative wave propagation [*Becker and Schmitz*, 2002] but also before turbulence-growth phase 2 when turbulence interacts with BG. After phase 2, KE is converted into IE. This conversion is primarily driven by the pressure flux, which is in agreement with the findings of *Becker and Schmitz* [2002]. Turbulence starts to decay after the KE_{turb} reaches its maximum. Approximately 5 minutes after the KE_{turb} peak (at the 69th minute), KE starts to be converted to IE, as shown by the red dashed line in the right top plot in Figure 3. This suggests that the decay of turbulence is related to the pressure flux $p\nabla \cdot \vec{v}$ and KE-IE conversion. This study indicates that heat transport due to wave propagation is the main cause of IE variation prior to gravity wave breaking or saturation in the mesopause region. IE change due to KE-IE convergence becomes the dominant factor when GW starts to break especially after wave-breaking-generated turbulence starts to decay.

The interactions between GWs and turbulence, between BG and GWs, and between BG and turbulence have distinct functions during the two phases of turbulence growth. The energy transferred through these interactions is summarized in the energy-transfer triangle shown in Figure 9. The blue arrows indicate the direction of energy transferred through related interactions during turbulence growth phase 1. The red arrows indicate the direction of energy transferred during turbulence growth phase 2. The size of the arrows represents the energy transfer magnitude. In this system, GWs are the source of KE. In the two phases of turbulence growth, GWs transferred 570 J of energy to BG through BG-GW interactions, with the majority of energy transfer occurring in phase 1.

The convergence of energy resulting from gravity wave saturation is linked to turbulence. Gravity wave saturation primarily occurs through instabilities that act locally to dissipate wave energy and produce turbulence. GW saturation results in net deceleration of the zonal mean flow and turbulent heating of the environment [*Fritts*, 1989]. Figure 9 suggests that the processes are possibly related to turbulence. Saturated GW transfers GW KE to BG flow, but more energy is transferred from BG to turbulence, most of which is converted into BG IE through turbulent heating.

As GWs propagate, they continuously interact with the BG flow and alter it. Simulations by *Bölöni et al.* [2016] suggest that direct BG-GW interactions dominate energy transfer over the wave-breaking. Our simulation shows consistent results in both phases of turbulence development, as demonstrated in Figure 6. Before turbulence-growth phase

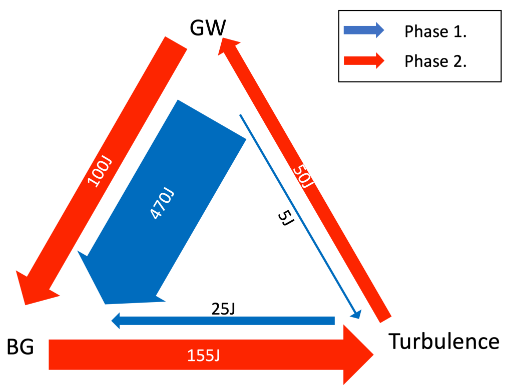

Figure 9: A schematic diagram of KE transfer between BG, GW, and turbulence. The blue arrows show the energy flow direction and amount during turbulence growth phase 1. The red arrows show the energy flow direction and amount during turbulence growth phase 2. The thicknesses of the arrows represent the amount of energy transferred within the time intervals of phases 1 or 2.

2, the KE transferred by direct BG-GW interactions is about 430 J and KE transferred related to the turbulence act is approximately 40 J. During phase 2, with the situation that the magnitude of turbulent perturbation grows rapidly, direct BG-GW interaction transfers 100 J KE to mean flow, while the turbulence transfers 50 J back to GW, as indicated by the red arrows in Figure 9.

GW-turbulence interactions initiated the initial development of turbulence. During phase 1, turbulence grows through both GW-turbulence interactions and self-strengthening. The transfer of energy between GWs and turbulence is solely achieved through the work done by the wave fluctuations in turbulent stress against the wave rates of strain [*Finnigan*, 1988; *Einaudi and Finnigan*, 1993; *Finnigan and Shaw*, 2008]. Our simulation confirms these results, showing that the transfer of KE between GWs and turbulence during the GW breaking process is solely achieved through the mechanism $U_t W_t \frac{\partial U_{g_i}}{\partial x_j}$. In this study, we also take into account the redistribution of KE_{turb} by GWs as part of the GW-turbulence interactions, even though no energy is directly transferred between the GWs and turbulence through this mechanism.

Our simulation reveals that the BG-turbulence interactions, particularly the buoyancy term, are the leading contributor to turbulence growth in phase 2, demonstrated by the green solid lines in the bottom plots of Figure 7. In the observation by *de Nijs and*

Pietrzak [2012], they found that buoyancy production dominates in some instants. The influence of buoyancy is typically taken into account as a sink of KE_{turb} but when buoyancy is negative, which is associated with unstable stratification, the buoyancy can convert turbulent potential energy into KE_{turb}. Therefore, buoyancy can cause an increase in KE_{turb}. Extra study about total turbulent energy and turbulent potential energy is necessary to examine this mechanism.

Convective instability is the first step leading to wave breaking and turbulence generation [*Koudella and Staquet*, 2006]. In the chosen domain, instabilities occur 10 minutes before GWs start to break. GW breaking generates turbulence which reduces instabilities through turbulence momentum flux absorbing energy from BG wind shear. This simulation provides support for the mechanisms proposed in *Fritts and Dunkerton* [1985].

This 2D simulation provided valuable insight into the dynamics of gravity wave breaking. However, as suggested by *Fritts et al.* [1994, 2022b,c] and *Andreassen et al.* [1994], 2D computations may not accurately capture the instability structure and turbulence generation associated with wave breaking. Additionally, this study focuses on turbulence kinetic energy (KE_{turb}) and does not account for conversions between KE_{turb} and turbulence potential energy. Further research in this area is necessary.

7 Conclusion

Energy conversions between KE, PE, and IE over the chosen region, are investigated. Throughout the simulation, kinetic energy in the mesopause region increased. Potential energy is converted to kinetic energy, and most of the increased kinetic energy is converted to internal energy. The energy conversion shows different patterns of dominance during the two intervals. Specifically, during the GW breaking process, the period of turbulence growth is divided into two distinct phases based on KE_{turb} change rate. Before phase 2, the dominant total energy change in the chosen region is caused by PE-KE conversion and KE transportation. After phase 1, the dominant total energy change in the chosen region results from PE-KE conversion and KE-IE conversion. The primary mechanism for KE-IE conversion is through pressure flux, which is associated with the decay of turbulence.

The kinetic energy transfer among the turbulence, GW, and background is studied. Energy transfers among these three components are bilateral. At different stages, the combined effects show different energy-transferring directions. The interactions between the BG and GWs dominate the energy transfer process during the GW-breaking event. On the other hand, GW-turbulence interactions initiated the growth of turbulence. However, in the second phase, the GW-turbulence interactions feed back energy from turbulence to the GWs. The only mechanism of energy transfer between GWs and turbulence through GW-turbulence interactions is the turbulent stress against the wave rates of strain. BG-turbulence interactions are the dominant contributor to the growth of turbulence, especially in the second phase, and the dominant contributor in BG-turbulence interaction is the work by buoyancy. However, buoyancy reduces KE_{GW} over the simulation.

Instabilities lead to the breaking of GWs. The breaking of GWs generates turbulence, which in turn weakens instabilities by dissipating wave energy. The BG acts as an intermediary in the process of turbulence dissipating wave energy.

DNS modeling studies are valuable in explaining small structure dynamics. Increasingly realistic DNS modeling can yield an improved ability to quantify the contributions to turbulence development through different mechanisms. More studies such as 3D simulations are necessary to improve our understanding of the GW breaking process.

8 Acknowledgement

This research was supported by National Science Foundation (NSF) grant AGS-1759471. The work by Alan Liu is supported by (while serving at) the NSF.

A: Energy Conversion

This appendix is to present the deduction for energy conservation among kinetic energy (KE), internal energy (IE), and potential energy (PE).

Start with CGCAM governing equations.

$$\frac{\partial \rho}{\partial t} + \frac{\partial(\rho u)}{\partial x} + \frac{\partial(\rho w)}{\partial z} = 0; \tag{A.1}$$

$$\frac{\partial(\rho u)}{\partial t} + \frac{\partial(\rho uu)}{\partial x} + \frac{\partial(\rho uw)}{\partial z} = -\frac{\partial p}{\partial x} + (\frac{\partial \sigma_{xx}}{\partial x} + \frac{\partial \sigma_{xz}}{\partial z}); \tag{A.2}$$

$$\frac{\partial(\rho w)}{\partial t} + \frac{\partial(\rho wu)}{\partial x} + \frac{\partial(\rho ww)}{\partial z} = -\frac{\partial p}{\partial z} - \rho g + (\frac{\partial \sigma_{xz}}{\partial x} + \frac{\partial \sigma_{zz}}{\partial z}). \tag{A.3}$$

(A.2) and (A.3) can be rewritten as

$$\rho\frac{\partial u}{\partial t} + \rho u\frac{\partial u}{\partial x} + \rho w\frac{\partial u}{\partial z} + u(\frac{\partial \rho}{\partial t} + \frac{\partial(\rho u)}{\partial x} + \frac{\partial(\rho w)}{\partial z}) = -\frac{\partial p}{\partial x} + (\frac{\partial \sigma_{xx}}{\partial x} + \frac{\partial \sigma_{xz}}{\partial z}); \tag{A.4}$$

$$\rho\frac{\partial w}{\partial t} + \rho u\frac{\partial w}{\partial x} + \rho w\frac{\partial w}{\partial z} + w(\frac{\partial \rho}{\partial t} + \frac{\partial(\rho u)}{\partial x} + \frac{\partial(\rho w)}{\partial z}) = -\frac{\partial p}{\partial z} - \rho g + (\frac{\partial \sigma_{xz}}{\partial x} + \frac{\partial \sigma_{zz}}{\partial z}). \tag{A.5}$$

Substitute (A.1) into the left hand side of equations above. The equations can be rewritten as follow after every term is divided by ρ. The equations describe the tendencies of momentum and energy per unit mass.

$$\frac{\partial u}{\partial t} + u\frac{\partial u}{\partial x} + w\frac{\partial u}{\partial z} = -\frac{1}{\rho}\frac{\partial p}{\partial x} + \frac{1}{\rho}\left(\frac{\partial \sigma_{xx}}{\partial x} + \frac{\partial \sigma_{xz}}{\partial z}\right), \tag{A.6}$$

$$\frac{\partial w}{\partial t} + u\frac{\partial w}{\partial x} + w\frac{\partial w}{\partial z} = -\frac{1}{\rho}\frac{\partial p}{\partial z} - g + \frac{1}{\rho}\left(\frac{\partial \sigma_{xz}}{\partial x} + \frac{\partial \sigma_{zz}}{\partial z}\right), \tag{A.7}$$

where

$$\sigma_{xx} = \mu\left(\frac{4}{3}\frac{\partial u}{\partial x} - \frac{2}{3}\frac{\partial w}{\partial z}\right), \tag{A.8}$$

$$\sigma_{zz} = \mu\left(\frac{4}{3}\frac{\partial w}{\partial z} - \frac{2}{3}\frac{\partial u}{\partial x}\right), \tag{A.9}$$

$$\sigma_{xz} = \mu\left(\frac{\partial w}{\partial x} + \frac{\partial u}{\partial z}\right), \tag{A.10}$$

where dynamical viscosity $\mu = 1.57\times10^{-5}$ (N m^{-3} kg). Substituting $\sigma_{xx}, \sigma_{zz}, \sigma_{xz}$ into (A.6) and (A.7) yields:

$$\frac{\partial u}{\partial t} + u\frac{\partial u}{\partial x} + w\frac{\partial u}{\partial z} = -\frac{1}{\rho}\frac{\partial p}{\partial x} + \mu\left(\frac{1}{\rho_0} - \frac{\rho_1}{\rho_0^2}\right)\left(\frac{4}{3}\frac{\partial^2 u}{\partial x^2} + \frac{1}{3}\frac{\partial^2 w}{\partial x \partial z} + \frac{\partial^2 u}{\partial z^2}\right), \tag{A.11}$$

$$\frac{\partial w}{\partial t} + u\frac{\partial w}{\partial x} + w\frac{\partial w}{\partial z} = -\frac{1}{\rho}\frac{\partial p}{\partial z} - g + \mu\left(\frac{1}{\rho_0} - \frac{\rho_1}{\rho_0^2}\right)\left(\frac{4}{3}\frac{\partial^2 w}{\partial z^2} + \frac{1}{3}\frac{\partial^2 u}{\partial x \partial z} + \frac{\partial^2 w}{\partial x^2}\right). \tag{A.12}$$

Part of the horizontal and vertical components of the kinetic energy tendency can be derived by multiplying ρu and ρw on (A.11) and (A.12), respectively.

$$\rho u\frac{\partial u}{\partial t}+\rho u^2\frac{\partial u}{\partial x}+\rho wu\frac{\partial u}{\partial z}=-u\frac{\partial p}{\partial x}+u\mu\left(\frac{4}{3}\frac{\partial^2 u}{\partial x^2}+\frac{1}{3}\frac{\partial^2 w}{\partial x\partial z}+\frac{\partial^2 u}{\partial z^2}\right), \tag{A.13}$$

$$\rho w\frac{\partial w}{\partial t}+\rho uw\frac{\partial w}{\partial x}+\rho w^2\frac{\partial w}{\partial z}=-w\frac{\partial p}{\partial z}-\rho wg+w\mu\left(\frac{4}{3}\frac{\partial^2 w}{\partial z^2}+\frac{1}{3}\frac{\partial^2 u}{\partial x\partial z}+\frac{\partial^2 w}{\partial x^2}\right). \tag{A.14}$$

The equations above missed the part of kinetic energy tendency due to density variation. Multiplying u^2 or w^2 with mass conservation (A.1) leads to the KE tendency due to density tendency:

$$u^2\frac{\partial \rho}{\partial t}+u^3\frac{\partial \rho}{\partial x}+u^2w\frac{\partial \rho}{\partial z}+\rho u^2\frac{\partial u}{\partial x}+\rho u^2\frac{\partial w}{\partial z}=0, \tag{A.15}$$

$$w^2\frac{\partial \rho}{\partial t}+w^2u\frac{\partial \rho}{\partial x}+w^3\frac{\partial \rho}{\partial z}+\rho w^2\frac{\partial u}{\partial x}+\rho w^2\frac{\partial w}{\partial z}=0. \tag{A.16}$$

Combining equations(A.13) and (A.15) together leads to the total tendency of the horizontal part of KE as (A.17). Combining equations(A.14) and (A.16) together gives the total vertical and the horizontal part of KE as (A.18). In the simulation, the diffusivity is negligible, so the diffusion terms are dropped in the KE tendency equations. The deduction of diffusion terms is in appendix 1.

$$\frac{\partial(\frac{1}{2}\rho u^2)}{\partial t}+\frac{1}{2}u^3\frac{\partial \rho}{\partial x}+\frac{1}{2}u^2w\frac{\partial \rho}{\partial z}+\frac{1}{2}\rho u^2\frac{\partial u}{\partial x}+\frac{1}{2}\rho u^2\frac{\partial w}{\partial z}+\rho u^2\frac{\partial u}{\partial x}+\rho uw\frac{\partial u}{\partial z}=-u\frac{\partial p}{\partial x}, \tag{A.17}$$

$$\frac{\partial(\frac{1}{2}\rho w^2)}{\partial t}+\frac{1}{2}w^2u\frac{\partial \rho}{\partial x}+\frac{1}{2}w^3\frac{\partial \rho}{\partial z}+\frac{1}{2}\rho w^2\frac{\partial u}{\partial x}+\frac{1}{2}\rho w^2\frac{\partial w}{\partial z}+\rho wu\frac{\partial w}{\partial x}+\rho w^2\frac{\partial w}{\partial z}=-w\frac{\partial p}{\partial z}-g\rho w. \tag{A.18}$$

Combining the 2 parts leads to the KE tendency.

$$\begin{aligned}\frac{\partial KE}{\partial t}&=-\nabla\cdot(KE\vec{v})-\vec{v}\cdot\nabla p-g\rho w\\&=-\nabla\cdot(KE\vec{v})-\nabla\cdot(p\vec{v})+p\nabla\cdot\vec{v}-g\rho w.\end{aligned} \tag{A.19}$$

The other part of the energy is the internal energy per unit mass (IE).

$$\mathrm{C_v}\frac{dT}{dt}-\frac{1}{\rho}\frac{dp}{dt}=\frac{\kappa}{\rho}\nabla^2 T+\frac{dq}{dt}, \tag{A.20}$$

where κ is the conductivity, and κ is not a constant.

$$\kappa=dif*suth. \tag{A.21}$$

where diffusivity $dif = \mu C_p/Pr$, where Prandtl number $Pr = 1$. $suth$ is Sutherland's formula:

$$suth = \frac{(T_0 + T_{suth})}{(T + T_{suth})}\left(\frac{T}{T_0}\right)^{3/2}, \tag{A.22}$$

where $T_{suth} = 110\,\mathrm{K}$. T_0 is the given background temperature in CGCAM at the initial time, which is 300 K. And dq/dt is zero since there is no heat input or output. So

$$\begin{aligned}\kappa &= \mu\frac{C_p}{Pr}\frac{(T_0 + T_{suth})}{(T + T_{suth})}\left(\frac{T}{T_0}\right)^{3/2}\\ \kappa &= \mu\frac{C_p}{Pr}\frac{410}{(T+110)}\left(\frac{T}{300}\right)^{3/2}.\end{aligned} \tag{A.23}$$

$$C_v\frac{dT}{dt} = \frac{1}{\rho}\frac{dp}{dt} + \frac{\kappa}{\rho}\nabla^2 T. \tag{A.24}$$

With ideal gas law,

$$C_v\frac{dT}{dt} = RT\frac{dln\rho}{dt} + \frac{\kappa}{\rho}\nabla^2 T. \tag{A.25}$$

With the continuity equation,

$$\begin{aligned}C_v\frac{dT}{dt} &= -RT\nabla\cdot\vec{v} + \frac{\kappa}{\rho}\nabla^2 T\\ \frac{\partial T}{\partial t} &= -\frac{1}{C_v}RT\nabla\cdot\vec{v} - \vec{v}\cdot\nabla T + \frac{\kappa}{C_v\rho}\nabla^2 T\\ &= -\frac{1}{\rho C_v}p\nabla\cdot\vec{v} - \vec{v}\cdot\nabla T + \frac{\kappa}{C_v\rho}\nabla^2 T.\end{aligned} \tag{A.26}$$

$C_v\rho\times$ (A.26) + $C_v T\times$ (A.1),

$$\begin{aligned}\frac{\partial IE}{\partial t} &= -C_v T(\vec{v}\cdot\nabla\rho + \rho\nabla\cdot\vec{v}) - p\nabla\cdot\vec{v} - C_v\rho\vec{v}\cdot\nabla T + \kappa\nabla^2 T\\ &= -\nabla\cdot(IE\vec{v}) - p\nabla\cdot\vec{v}.\end{aligned} \tag{A.27}$$

Another energy format is potential energy (PE). Potential energy PE = ρgh. The tendency of PE is

$$\begin{aligned}\frac{\partial pE}{\partial t} = gh\frac{\partial\rho}{\partial t} + g\rho w &= -gh(\vec{v}\cdot\nabla\rho + \rho\nabla\cdot\vec{v}) + g\rho w\\ &= -\nabla\cdot(PE\vec{v}) + g\rho w.\end{aligned} \tag{A.28}$$

B: Energy Transfer among Background and Perturbations

The variables are separated into the background part and the perturbation part. Define variable $q = q_0 + q_1$, and $q_0 = q_0(x,z), q_1 = q_1(t,x,z)$. Rewrite (A.11), (A.12), (A.13) and (A.14) as:

$$
\begin{aligned}
&\frac{\partial u_0}{\partial t}+\frac{\partial u_1}{\partial t}+\vec{v_0}\cdot\nabla u_0+\vec{v_1}\cdot\nabla u_0+\vec{v_0}\cdot\nabla u_1+\vec{v_1}\cdot\nabla u_1\\
&\quad=-\frac{1}{\rho_0}\frac{\partial p_0}{\partial x}-\frac{1}{\rho_0}\frac{\partial p_1}{\partial x}+\frac{\rho_1}{\rho_0^2}\frac{\partial p_0}{\partial x}+\frac{\rho_1}{\rho_0^2}\frac{\partial p_1}{\partial x}\\
&+\mu(\frac{1}{\rho_0}-\frac{\rho_1}{\rho_0^2})\left(\frac{4}{3}\frac{\partial^2 u_0}{\partial x^2}+\frac{1}{3}\frac{\partial^2 w_0}{\partial x\partial z}+\frac{\partial^2 u_0}{\partial z^2}+\frac{4}{3}\frac{\partial^2 u_1}{\partial x^2}+\frac{1}{3}\frac{\partial^2 w_1}{\partial x\partial z}+\frac{\partial^2 u_1}{\partial z^2}\right),
\end{aligned}
\tag{B.1}
$$

$$
\begin{aligned}
&\frac{\partial w_0}{\partial t}+\frac{\partial w_1}{\partial t}+\vec{v_0}\cdot\nabla w_0+\vec{v_1}\cdot\nabla w_0+\vec{v_0}\cdot\nabla w_1+\vec{v_1}\cdot\nabla w_1\\
&\quad=-\frac{1}{\rho_0}\frac{\partial p_0}{\partial z}-\frac{1}{\rho_0}\frac{\partial p_1}{\partial z}+\frac{\rho_1}{\rho_0^2}\frac{\partial p_0}{\partial z}+\frac{\rho_1}{\rho_0^2}\frac{\partial p_1}{\partial z}-g\\
&+\mu(\frac{1}{\rho_0}-\frac{\rho_1}{\rho_0^2})\left(\frac{4}{3}\frac{\partial^2 w_0}{\partial z^2}+\frac{1}{3}\frac{\partial^2 u_0}{\partial x\partial z}+\frac{\partial^2 w_0}{\partial x^2}+\frac{4}{3}\frac{\partial^2 w_1}{\partial z^2}+\frac{1}{3}\frac{\partial^2 u_1}{\partial x\partial z}+\frac{\partial^2 w_1}{\partial x^2}\right),
\end{aligned}
\tag{B.2}
$$

where Taylor expansion $\frac{1}{\rho_0+\rho_1}=\frac{1}{\rho_0}-\frac{\rho_1}{\rho_0^2}+\frac{2\rho_1^2}{\rho_0^3}+O(\rho^2)$ is used. Do a time average over one period. For the ideally theoretical case, the averaged q_0 over one period stays the same and the linear terms would vanish. Do a time average on (B.1) and (B.2). The tendency for averaged variables q_0 can be derived.

$$
\begin{aligned}
&\frac{\partial u_0}{\partial t}+\vec{v_0}\cdot\nabla u_0+\overline{\vec{v_1}\cdot\nabla u_1}\\
&\quad=-\frac{1}{\rho_0}\frac{\partial p_0}{\partial x}+\overline{\frac{\rho_1}{\rho_0^2}\frac{\partial p_1}{\partial x}}\\
&+\mu\frac{1}{\rho_0}\left(\frac{4}{3}\frac{\partial^2 u_0}{\partial x^2}+\frac{1}{3}\frac{\partial^2 w_0}{\partial x\partial z}+\frac{\partial^2 u_0}{\partial z^2}\right)-\mu\frac{1}{\rho_0^2}\left(\frac{4}{3}\overline{\rho_1\frac{\partial^2 u_1}{\partial x^2}}+\frac{1}{3}\overline{\rho_1\frac{\partial^2 w_1}{\partial x\partial z}}+\overline{\frac{\rho_1\partial^2 u_1}{\partial z^2}}\right),
\end{aligned}
\tag{B.3}
$$

$$
\begin{aligned}
&\frac{\partial w_0}{\partial t}+\vec{v_0}\cdot\nabla w_0+\overline{\vec{v_1}\cdot\nabla w_1}\\
&\quad=-\frac{1}{\rho_0}\frac{\partial p_0}{\partial z}+\overline{\frac{\rho_1}{\rho_0^2}\frac{\partial p_1}{\partial z}}-g\\
&+\mu\frac{1}{\rho_0}\left(\frac{4}{3}\frac{\partial^2 w_0}{\partial z^2}+\frac{1}{3}\frac{\partial^2 u_0}{\partial x\partial z}+\frac{\partial^2 w_0}{\partial x^2}\right)-\mu\frac{1}{\rho_0^2}\left(\frac{4}{3}\overline{\rho_1\frac{\partial^2 w_1}{\partial z^2}}+\frac{1}{3}\overline{\rho_1\frac{\partial^2 u_1}{\partial x\partial z}}+\overline{\rho_1\frac{\partial^2 w_1}{\partial x^2}}\right).
\end{aligned}
\tag{B.4}
$$

Derive momentum equations for perturbations or GWs by subtracting the BG-period-averaged equations from (B.1) and (B.2).

$$
\begin{aligned}
&\frac{\partial u_1}{\partial t}+\vec{v_1}\cdot\nabla u_0+\vec{v_0}\cdot\nabla u_1+\vec{v_1}\cdot\nabla u_1-\overline{\vec{v_1}\cdot\nabla u_1}\\
&\quad=-\frac{1}{\rho_0}\frac{\partial p_1}{\partial x}+\frac{\rho_1}{\rho_0^2}\frac{\partial p_0}{\partial x}+\frac{\rho_1}{\rho_0^2}\frac{\partial p_1}{\partial x}-\overline{\frac{\rho_1}{\rho_0^2}\frac{\partial p_1}{\partial x}}\\
&\quad+\mu\frac{1}{\rho_0}\left(\frac{4}{3}\frac{\partial^2 u_1}{\partial x^2}+\frac{1}{3}\frac{\partial^2 w_1}{\partial x\partial z}+\frac{\partial^2 u_1}{\partial z^2}\right)\\
&-\mu\frac{\rho_1}{\rho_0^2}\left(\frac{4}{3}\frac{\partial^2 u_0}{\partial x^2}+\frac{1}{3}\frac{\partial^2 w_0}{\partial x\partial z}+\frac{\partial^2 u_0}{\partial z^2}+\frac{4}{3}\frac{\partial^2 u_1}{\partial x^2}+\frac{1}{3}\frac{\partial^2 w_1}{\partial x\partial z}+\frac{\partial^2 u_1}{\partial z^2}\right)\\
&\quad+\mu\frac{1}{\rho_0^2}\left(\frac{4}{3}\overline{\rho_1\frac{\partial^2 u_1}{\partial x^2}}+\frac{1}{3}\overline{\rho_1\frac{\partial^2 w_1}{\partial x\partial z}}+\overline{\frac{\rho_1\partial^2 u_1}{\partial z^2}}\right),
\end{aligned}
\tag{B.5}
$$

$$\begin{aligned}
&\frac{\partial w_1}{\partial t} + \vec{v_1}\cdot\nabla w_0 + \vec{v_0}\cdot\nabla w_1 + \vec{v_1}\cdot\nabla w_1 - \overline{\vec{v_1}\cdot\nabla w_1} \\
&= -\frac{1}{\rho_0}\frac{\partial p_1}{\partial z} + \frac{\rho_1}{\rho_0^2}\frac{\partial p_0}{\partial z} + \frac{\rho_1}{\rho_0^2}\frac{\partial p_1}{\partial z} - \overline{\frac{\rho_1}{\rho_0^2}\frac{\partial p_1}{\partial z}} \\
&+\mu\frac{1}{\rho_0}\left(\frac{4}{3}\frac{\partial^2 w_1}{\partial z^2} + \frac{1}{3}\frac{\partial^2 u_1}{\partial x\partial z} + \frac{\partial^2 w_1}{\partial x^2}\right) \\
&-\mu(\frac{\rho_1}{\rho_0^2})\left(\frac{4}{3}\frac{\partial^2 w_0}{\partial z^2} + \frac{1}{3}\frac{\partial^2 u_0}{\partial x\partial z} + \frac{\partial^2 w_0}{\partial x^2} + \frac{4}{3}\frac{\partial^2 w_1}{\partial z^2} + \frac{1}{3}\frac{\partial^2 u_1}{\partial x\partial z} + \frac{\partial^2 w_1}{\partial x^2}\right) \\
&+\mu\frac{1}{\rho_0^2}\left(\frac{4}{3}\overline{\rho_1\frac{\partial^2 w_1}{\partial z^2}} + \frac{1}{3}\overline{\rho_1\frac{\partial^2 u_1}{\partial x\partial z}} + \overline{\rho_1\frac{\partial^2 w_1}{\partial x^2}}\right).
\end{aligned} \tag{B.6}$$

685 For kinetic energy (KE), KE is separated into background and perturbation parts. KE in
686 GWs is averaged over a wave period.

$$\begin{aligned}
KE_x &= \frac{1}{2}\overline{\rho u^2} \\
&= \frac{1}{2}\rho_0 u_0^2 + \frac{1}{2}\rho_0\overline{u_1^2} + \rho_0\overline{u_0 u_1},
\end{aligned} \tag{B.7}$$

687 where $\overline{u_0 u_1} = 0$ for averaging over a period. The horizontal part of background KE and
688 perturbation KE change rate are derived by multiplying $\rho_0 u_0$ and $\rho_0 u_1$ to every terms of
689 horizontal part of background and perturbation momentum change rate equations (B.3)
690 and (B.5), respectively. The same processes are applied to the vertical part of KE.

$$\begin{aligned}
&\rho_0\frac{\partial u_0^2}{2\partial t} + \rho_0 u_0\vec{v_0}\cdot\nabla u_0 + \rho_0 u_0\overline{\vec{v_1}\cdot\nabla u_1} \\
&= -u_0\frac{\partial p_0}{\partial x} + u_0\overline{\frac{\rho_1}{\rho_0}\frac{\partial p_1}{\partial x}} \\
&+\mu u_0\left(\frac{4}{3}\frac{\partial^2 u_0}{\partial x^2} + \frac{1}{3}\frac{\partial^2 w_0}{\partial x\partial z} + \frac{\partial^2 u_0}{\partial z^2}\right) - \mu\frac{u_0}{\rho_0}\left(\frac{4}{3}\overline{\rho_1\frac{\partial^2 u_1}{\partial x^2}} + \frac{1}{3}\overline{\rho_1\frac{\partial^2 w_1}{\partial x\partial z}} + \overline{\frac{\rho_1\partial^2 u_1}{\partial z^2}}\right).
\end{aligned} \tag{B.8}$$

$$\begin{aligned}
&\rho_0\frac{\partial u_1^2}{2\partial t} + \rho_0 u_1\vec{v_1}\cdot\nabla u_0 + \rho_0 u_1\vec{v_0}\cdot\nabla u_1 + \rho_0 u_1\vec{v_1}\cdot\nabla u_1 - \rho_0 u_1\overline{\vec{v_1}\cdot\nabla u_1} \\
&= -u_1\frac{\partial p_1}{\partial x} + \frac{u_1\rho_1}{\rho_0}\frac{\partial p_0}{\partial x} + \frac{\rho_1 u_1}{\rho_0}\frac{\partial p_1}{\partial x} - u_1\overline{\frac{\rho_1}{\rho_0}\frac{\partial p_1}{\partial x}} \\
&+\mu u_1\left(\frac{4}{3}\frac{\partial^2 u_1}{\partial x^2} + \frac{1}{3}\frac{\partial^2 w_1}{\partial x\partial z} + \frac{\partial^2 u_1}{\partial z^2}\right) \\
&-\mu\frac{u_1\rho_1}{\rho_0}\left(\frac{4}{3}\frac{\partial^2 u_0}{\partial x^2} + \frac{1}{3}\frac{\partial^2 w_0}{\partial x\partial z} + \frac{\partial^2 u_0}{\partial z^2} + \frac{4}{3}\frac{\partial^2 u_1}{\partial x^2} + \frac{1}{3}\frac{\partial^2 w_1}{\partial x\partial z} + \frac{\partial^2 u_1}{\partial z^2}\right) \\
&+\mu\frac{u_1}{\rho_0}\left(\frac{4}{3}\overline{\rho_1\frac{\partial^2 u_1}{\partial x^2}} + \frac{1}{3}\overline{\rho_1\frac{\partial^2 w_1}{\partial x\partial z}} + \overline{\frac{\rho_1\partial^2 u_1}{\partial z^2}}\right).
\end{aligned} \tag{B.9}$$

$$
\begin{aligned}
&\rho_0\frac{\partial w_0^2}{2\partial t}+\rho_0 w_0\vec{v_0}\cdot\nabla w_0+\rho_0 w_0\overline{\vec{v_1}\cdot\nabla w_1}\\
&=-w_0\frac{\partial p_0}{\partial z}+w_0\overline{\frac{\rho_1}{\rho_0}\frac{\partial p_1}{\partial z}}-\rho_0 g w_0\\
&+\mu w_0\left(\frac{4}{3}\frac{\partial^2 w_0}{\partial z^2}+\frac{1}{3}\frac{\partial^2 u_0}{\partial x\partial z}+\frac{\partial^2 w_0}{\partial x^2}\right)\\
&-\mu\frac{w_0}{\rho_0}\left(\frac{4}{3}\overline{\rho_1\frac{\partial^2 w_1}{\partial z^2}}+\frac{1}{3}\overline{\rho_1\frac{\partial^2 u_1}{\partial x\partial z}}+\overline{\rho_1\frac{\partial^2 w_1}{\partial x^2}}\right).
\end{aligned}
\tag{B.10}
$$

$$
\begin{aligned}
&\rho_0\frac{\partial w_1^2}{2\partial t}+\rho_0 w_1\vec{v_1}\cdot\nabla w_0+\rho_0 w_1\vec{v_0}\cdot\nabla w_1+\rho_0 w_1\vec{v_1}\cdot\nabla w_1-\rho_0 w_1\overline{\vec{v_1}\cdot\nabla w_1}\\
&=-w_1\frac{\partial p_1}{\partial z}+\frac{w_1\rho_1}{\rho_0}\frac{\partial p_0}{\partial z}+\frac{w_1\rho_1}{\rho_0}\frac{\partial p_1}{\partial z}-w_1\overline{\frac{\rho_1}{\rho_0}\frac{\partial p_1}{\partial z}}\\
&+\mu w_1\left(\frac{4}{3}\frac{\partial^2 w_1}{\partial z^2}+\frac{1}{3}\frac{\partial^2 u_1}{\partial x\partial z}+\frac{\partial^2 w_1}{\partial x^2}\right)\\
&-\mu\frac{\rho_1 w_1}{\rho_0}\left(\frac{4}{3}\frac{\partial^2 w_0}{\partial z^2}+\frac{1}{3}\frac{\partial^2 u_0}{\partial x\partial z}+\frac{\partial^2 w_0}{\partial x^2}+\frac{4}{3}\frac{\partial^2 w_1}{\partial z^2}+\frac{1}{3}\frac{\partial^2 u_1}{\partial x\partial z}+\frac{\partial^2 w_1}{\partial x^2}\right)\\
&+\mu\frac{w_1}{\rho_0}\left(\frac{4}{3}\overline{\rho_1\frac{\partial^2 w_1}{\partial z^2}}+\frac{1}{3}\overline{\rho_1\frac{\partial^2 u_1}{\partial x\partial z}}+\overline{\rho_1\frac{\partial^2 w_1}{\partial x^2}}\right),
\end{aligned}
\tag{B.11}
$$

Combining 2 parts of background KE tendency equations (B.8) and (B.10) together gives the KE_0 tendency:

$$
\begin{aligned}
&\frac{\partial KE_0}{\partial t}+\rho_0 u_0 u_0\frac{\partial u_0}{\partial x}+\rho_0 w_0 w_0\frac{\partial w_0}{\partial z}+\rho_0 w_0 u_0\left(\frac{\partial w_0}{\partial x}+\frac{\partial u_0}{\partial z}\right)\\
&+\rho_0 u_0\overline{\vec{v_1}\cdot\nabla u_1}+\rho_0 w_0\overline{\vec{v_1}\cdot\nabla w_1}\\
&=-\vec{v_0}\cdot\nabla p_0+\vec{v_0}\cdot\overline{\frac{\rho_1}{\rho_0}\nabla p_1}-\rho_0 g w_0\\
&+\mu u_0\left(\frac{4}{3}\frac{\partial^2 u_0}{\partial x^2}+\frac{1}{3}\frac{\partial^2 w_0}{\partial x\partial z}+\frac{\partial^2 u_0}{\partial z^2}\right)\\
&-\mu\frac{u_0}{\rho_0}\left(\frac{4}{3}\overline{\rho_1\frac{\partial^2 u_1}{\partial x^2}}+\frac{1}{3}\overline{\rho_1\frac{\partial^2 w_1}{\partial x\partial z}}+\overline{\frac{\rho_1\partial^2 u_1}{\partial z^2}}\right)\\
&+\mu\frac{w_0}{\rho_0}\left(\frac{4}{3}\frac{\partial^2 w_0}{\partial z^2}+\frac{1}{3}\frac{\partial^2 u_0}{\partial x\partial z}+\frac{\partial^2 w_0}{\partial x^2}\right)\\
&-\mu\frac{w_0}{\rho_0}\left(\frac{4}{3}\overline{\rho_1\frac{\partial^2 w_1}{\partial z^2}}+\frac{1}{3}\overline{\rho_1\frac{\partial^2 u_1}{\partial x\partial z}}+\overline{\rho_1\frac{\partial^2 w_1}{\partial x^2}}\right).
\end{aligned}
\tag{B.12}
$$

Combining two parts of KE_1 equations (B.9) and (B.11) yields:

$$
\begin{aligned}
&\frac{\partial KE_1}{\partial t} + \rho_0 u_1 \vec{v_1} \cdot \nabla u_0 + \rho_0 u_1 \vec{v_0} \cdot \nabla u_1 + \rho_0 u_1 \vec{v_1} \cdot \nabla u_1 \\
&+\rho_0 w_1 \vec{v_1} \cdot \nabla w_0 + \rho_0 w_1 \vec{v_0} \cdot \nabla w_1 + \rho_0 w_1 \vec{v_1} \cdot \nabla w_1 \\
&= -\vec{v_1} \cdot \nabla p_1 + \frac{\vec{v_1}\rho_1}{\rho_0} \cdot \nabla p_0 + \frac{\vec{v_1}\rho_1}{\rho_0} \cdot \nabla p_1 \\
&+\rho_0 u_1 \overline{\vec{v_1} \cdot \nabla u_1} + \rho_0 w_1 \overline{\vec{v_1} \cdot \nabla w_1} - u_1 \overline{\frac{\rho_1}{\rho_0}\frac{\partial p_1}{\partial x}} - w_1 \overline{\frac{\rho_1}{\rho_0}\frac{\partial p_1}{\partial z}} \\
&+\rho_0 \frac{4}{3}\mu \frac{u_1}{\rho_0}\frac{\partial^2 u_1}{\partial x^2} + \rho_0 \frac{1}{3}\mu \frac{u_1}{\rho_0}\frac{\partial^2 w_1}{\partial x \partial z} + \rho_0 \mu \frac{u_1}{\rho_0}\frac{\partial^2 u_1}{\partial z^2} \\
&-\rho_0 \frac{4}{3}\mu \frac{u_1\rho_1}{\rho_0^2}\frac{\partial^2 u_0}{\partial x^2} - \rho_0 \frac{1}{3}\mu \frac{u_1\rho_1}{\rho_0^2}\frac{\partial^2 w_0}{\partial x \partial z} - \rho_0 \mu \frac{u_1\rho_1}{\rho_0^2}\frac{\partial^2 u_0}{\partial z^2} \\
&-\rho_0 \frac{4}{3}\mu \frac{u_1\rho_1}{\rho_0^2}\frac{\partial^2 u_1}{\partial x^2} - \rho_0 \frac{1}{3}\mu \frac{u_1\rho_1}{\rho_0^2}\frac{\partial^2 w_1}{\partial x \partial z} - \rho_0 \mu \frac{u_1\rho_1}{\rho_0^2}\frac{\partial^2 u_1}{\partial z^2} \\
&+\frac{4}{3}\mu\rho_0 \frac{w_1}{\rho_0}\frac{\partial^2 w_1}{\partial z^2} + \frac{1}{3}\mu\rho_0 \frac{w_1}{\rho_0}\frac{\partial^2 u_1}{\partial x \partial z} + \mu\rho_0 \frac{w_1}{\rho_0}\frac{\partial^2 w_1}{\partial x^2} \\
&-\mu\rho_0 \frac{\rho_1 w_1}{\rho_0^2}\frac{4}{3}\frac{\partial^2 w_0}{\partial z^2} - \mu\rho_0 \frac{\rho_1 w_1}{\rho_0^2}\frac{1}{3}\frac{\partial^2 u_0}{\partial x \partial z} - \mu\rho_0 \frac{\rho_1 w_1}{\rho_0^2}\frac{\partial^2 w_0}{\partial x^2} \\
&-\mu\rho_0 \frac{\rho_1 w_1}{\rho_0^2}\frac{4}{3}\frac{\partial^2 w_1}{\partial z^2} - \mu\rho_0 \frac{\rho_1 w_1}{\rho_0^2}\frac{1}{3}\frac{\partial^2 u_1}{\partial x \partial z} - \mu\rho_0 \frac{\rho_1 w_1}{\rho_0^2}\frac{\partial^2 w_1}{\partial x^2}.
\end{aligned}
\tag{B.13}
$$

From the tendency for KE in perturbation, it is clear that the instantaneous KE_1 variation is related to BG flow expansion or compression, products of perturbation momentum flux and BG shear, advection, BG pressure gradient work, and perturbation pressure gradient work. Based on the model output, the KE change due to diffusivity is negligible. So equations for tendencies can be simplified as:

$$
\begin{aligned}
&\frac{\partial KE_0}{\partial t} + \rho_0 u_0 u_0 \frac{\partial u_0}{\partial x} + \rho_0 w_0 w_0 \frac{\partial w_0}{\partial z} + \rho_0 w_0 u_0 (\frac{\partial w_0}{\partial x} + \frac{\partial u_0}{\partial z}) \\
&+\rho_0 u_0 \overline{\vec{v_1} \cdot \nabla u_1} + \rho_0 w_0 \overline{\vec{v_1} \cdot \nabla w_1} \\
&= -\vec{v_0} \cdot \nabla p_0 + \vec{v_0} \cdot \overline{\frac{\rho_1}{\rho_0}\nabla p_1} - \rho_0 g w_0,
\end{aligned}
\tag{B.14}
$$

$$
\begin{aligned}
&\frac{\partial KE_1}{\partial t} + \rho_0 u_1 \vec{v_1} \cdot \nabla u_0 + \rho_0 u_1 \vec{v_0} \cdot \nabla u_1 + \rho_0 u_1 \vec{v_1} \cdot \nabla u_1 \\
&+\rho_0 w_1 \vec{v_1} \cdot \nabla w_0 + \rho_0 w_1 \vec{v_0} \cdot \nabla w_1 + \rho_0 w_1 \vec{v_1} \cdot \nabla w_1 \\
&= -\vec{v_1} \cdot \nabla p_1 + \frac{\vec{v_1}\rho_1}{\rho_0} \cdot \nabla p_0 + \frac{\vec{v_1}\rho_1}{\rho_0} \cdot \nabla p_1 \\
&+\rho_0 u_1 \overline{\vec{v_1} \cdot \nabla u_1} + \rho_0 w_1 \overline{\vec{v_1} \cdot \nabla w_1} - u_1 \overline{\frac{\rho_1}{\rho_0}\frac{\partial p_1}{\partial x}} - w_1 \overline{\frac{\rho_1}{\rho_0}\frac{\partial p_1}{\partial z}}.
\end{aligned}
\tag{B.15}
$$

Acknowledgments

This work and the Na lidar operation at ALO is being supported by the National Science Foundation (NSF) grants AGS-1759471.

References

Achatz, U. (2007), Gravity-wave breaking: Linear and primary nonlinear dynamics, *Adv. Space Res.*, *40*(6), 719–733, doi:10.1016/j.asr.2007.03.078.

Andreassen, Ø., C. E. Wasberg, D. C. Fritts, and J. R. Isler (1994), Gravity wave breaking in two and three dimensions: 1. model description and comparison of two-dimensional evolutions, *J. Geophys. Res. Atmos.*, *99*(D4), 8095–8108, doi:10.1029/93JD03435.

Atlas, R., and C. Bretherton (2022), Aircraft observations of gravity wave activity and turbulence in the tropical tropopause layer: prevalence, influence on cirrus and comparison with global-storm resolving models, *Atmos Chem Phys.*, *2022*, 1–30, doi:10.5194/acp-2022-491.

Barat, J., and J. C. Genie (1982), A new tool for the three-dimensional sounding of the atmosphere: The helisonde, *Journal of Applied Meteorology and Climatology*, *21*(10), 1497 – 1505, doi:10.1175/1520-0450(1982)021<1497:ANTFTT>2.0.CO;2.

Barbano, F., L. Brogno, F. Tampieri, and S. Di Sabatino (2022), Interaction between waves and turbulence within the nocturnal boundary layer, *Boundary-Layer Meteorol*, *183*, doi:10.1007/s10546-021-00678-2.

Becker, E., and G. Schmitz (2002), Energy deposition and turbulent dissipation owing to gravity waves in the mesosphere, *J. Atmos. Sci.*, *59*(1), 54 – 68, doi:10.1175/1520-0469(2002)059<0054:EDATDO>2.0.CO;2.

Bühler, O. (2010), Wave–vortex interactions in fluids and superfluids, *Annual Review of Fluid Mechanics*, *42*(1), 205–228, doi:10.1146/annurev.fluid.010908.165251.

Bölöni, G., B. Ribstein, J. Muraschko, C. Sgoff, J. Wei, and U. Achatz (2016), The interaction between atmospheric gravity waves and large-scale flows: An efficient description beyond the nonacceleration paradigm, *J. Atmos. Sci.*, *73*(12), 4833 – 4852, doi: 10.1175/JAS-D-16-0069.1.

Clayson, C. A., and L. Kantha (2008), On turbulence and mixing in the free atmosphere inferred from high-resolution soundings, *J. Atmos. Ocean. Technol.*, *25*(6), 833 – 852, doi:10.1175/2007JTECHA992.1.

de Nijs, M. A. J., and J. D. Pietrzak (2012), On total turbulent energy and the passive and active role of buoyancy in turbulent momentum and mass transfer, *Ocean Dynamics*, *62*, 849–865, doi:10.1007/s10236-012-0536-6.

Dong, W., D. C. Fritts, T. S. Lund, S. A. Wieland, and S. Zhang (2020), Self-acceleration and instability of gravity wave packets: 2. two-dimensional packet propagation, instability dynamics, and transient flow responses, *J.Geophys.Res.Atmos*, *125*(3), e2019JD030,691, doi:10.1029/2019JD030691.

Dong, W., D. C. Fritts, M. P. Hickey, A. Z. Liu, T. S. Lund, S. Zhang, Y. Yan, and F. Yang (2022), Modeling studies of gravity wave dynamics in highly structured environments: Reflection, trapping, instability, momentum transport, secondary gravity waves, and induced flow responses, *Journal of Geophysical Research: Atmospheres*, *127*(13), e2021JD035,894, doi:https://doi.org/10.1029/2021JD035894, e2021JD035894 2021JD035894.

Doran, P. M. (2013), Chapter 7 - fluid flow, in *Bioprocess Engineering Principles (Second Edition)*, edited by P. M. Doran, second edition ed., pp. 201–254, Academic Press, London, doi:https://doi.org/10.1016/B978-0-12-220851-5.00007-1.

Dunkerton, T. J. (1987), Effect of nonlinear instability on gravity-wave momentum transport, *J. Atmos. Sci.*, *44*(21), 3188 – 3209, doi:10.1175/1520-0469(1987)044<3188:EONIOG>2.0.CO;2.

Dunkerton, T. J., and D. C. Fritts (1984), Transient gravity wave-critical layer interaction. I Convective adjustment and the mean zonal acceleration, *J. Atmos. Sci.*, *41*, 992–1007, doi:10.1175/1520-0469(1984)041<0992:TGWCLI>2.0.CO;2.

Einaudi, F., and J. J. Finnigan (1993), Wave-turbulence dynamics in the stably stratified boundary layer, *50:13*, doi:10.1175/1520-0469(1993)050<1841:WTDITS>2.0.CO;2.

Felten, F. N., and T. S. Lund (2006), Kinetic energy conservation issues associated with the collocated mesh scheme for incompressible flow, *Journal of Computational Physics*, *215*(2), 465 – 484, doi:https://doi.org/10.1016/j.jcp.2005.11.009.

Finnigan, J. J. (1988), Kinetic energy transfer between internal gravity waves and turbulence, *Journal of Atmospheric Sciences*, *45*(3), 486 – 505, doi:10.1175/1520-0469(1988)045<0486:KETBIG>2.0.CO;2.

Finnigan, J. J., and F. Einaudi (1981), The interaction between an internal gravity wave and the planetary boundary layer. part ii: Effect of the wave on the turbulence structure, *Q J R Meteorol Soc.*, *107*(454), 807–832, doi:https://doi.org/10.1002/qj.49710745405.

Finnigan, J. J., and R. H. Shaw (2008), Double-averaging methodology and its application to turbulent flow in and above vegetation canopies, *Acta Geophysica*, *56*, 534 – 561, doi:10.2478/s11600-008-0034-x.

Finnigan, J. J., F. Einaudi, and D. Fua (1984), The interaction between an internal gravity wave and turbulence in the stably-stratified nocturnal boundary layer, *J. Atmos. Sci.*, *41*(16), 2409 – 2436, doi:10.1175/1520-0469(1984)041<2409:TIBAIG>2.0.CO;2.

Fritts, D. C. (1989), A review of gravity wave saturation processes, effects, and variability in the middle atmosphere, *pure and applied geophysics*, *130*, 343–371, doi: 10.1007/BF00874464.

Fritts, D. C., and M. J. Alexander (2003), Gravity wave dynamics and effects in the middle atmosphere, *Rev. Geophys.*, *41*(1), doi:https://doi.org/10.1029/2001RG000106.

Fritts, D. C., and T. J. Dunkerton (1985), Fluxes of heat and constituents due to convectively unstable gravity waves, *J. Atmos. Sci.*, *42*(6), 549–556, doi:10.1175/1520-0469(1985)042<0549:FOHACD>2.0.CO;2.

Fritts, D. C., J. R. Isler, and Ø. Andreassen (1994), Gravity wave breaking in two and three dimensions: 2. Three-dimensional evolution and instability structure, *J. Geophys. Res.*, *99*(D4), 8109–8123, doi:10.1029/93JD03436.

Fritts, D. C., J. F. Garten, and Øyvind Andreassen (1996), Wave breaking and transition to turbulence in stratified shear flows, *J. Atmos. Sci.*, *53*(8), 1057 – 1085, doi: 10.1175/1520-0469(1996)053<1057:WBATTT>2.0.CO;2.

Fritts, D. C., C. Bizon, J. A. Werne, and C. K. Meyer (2003), Layering accompanying turbulence generation due to shear instability and gravity-wave breaking, *J. Geophys. Res. Atmos.*, *108*(D8), doi:https://doi.org/10.1029/2002JD002406.

Fritts, D. C., B. P. Williams, C. Y. She, J. D. Vance, M. Rapp, F.-J. Lübken, A. Müllemann, F. J. Schmidlin, and R. A. Goldberg (2004), Observations of extreme temperature and wind gradients near the summer mesopause during the macwave/midas rocket campaign, *Geophys. Res. Lett.*, *31*(24), doi:https://doi.org/10.1029/2003GL019389.

Fritts, D. C., L. Wang, and J. A. Werne (2013a), Gravity wave–fine structure interactions. part i: Influences of fine structure form and orientation on flow evolution and instability, *J. Atmos. Sci*, *70*(12), 3710 – 3734, doi:10.1175/JAS-D-13-055.1.

Fritts, D. C., L. Wang, and J. A. Werne (2013b), Gravity wave–fine structure interactions. part i: Influences of fine structure form and orientation on flow evolution and instability, *Journal of the Atmospheric Sciences*, *70*(12), 3710 – 3734, doi:10.1175/JAS-D-13-055.1.

Fritts, D. C., B. Laughman, T. S. Lund, and J. B. Snively (2015), Self-acceleration and instability of gravity wave packets: 1. effects of temporal localization, *J. Geophys. Res. Atmos.*, *120*(17), 8783–8803, doi:https://doi.org/10.1002/2015JD023363.

Fritts, D. C., L. Wang, M. A. Geller, D. A. Lawrence, J. Werne, and B. B. Balsley (2016), Numerical Modeling of Multiscale Dynamics at a High Reynolds Number: Instabilities, Turbulence, and an Assessment of Ozmidov and Thorpe Scales, *J.Atmos.Sci*, *73*, 555–578.

Fritts, D. C., L. Wang, G. Baumgarten, A. D. Miller, M. A. Geller, G. Jones, M. Limon, D. Chapman, J. Didier, C. B. Kjellstrand, D. Araujo, S. Hillbrand, A. Korotkov, G. Tucker, and J. Vinokurov (2017a), High-resolution observations and modeling of turbulence sources, structures, and intensities in the upper mesosphere, *J. Atmos. Sol. Terr. Phys.*, *162*, 57–78, doi:https://doi.org/10.1016/j.jastp.2016.11.006, layered Phenomena in the Mesopause Region.

Fritts, D. C., L. Wang, G. Baumgarten, A. D. Miller, M. A. Geller, G. Jones, M. Limon, D. Chapman, J. Didier, C. B. Kjellstrand, D. Araujo, S. Hillbrand, A. Korotkov, G. Tucker, and J. Vinokurov (2017b), High-resolution observations and modeling of turbulence sources, structures, and intensities in the upper mesosphere, *J. Atmos. Sol. Terr. Phys.*, *162*, 57 – 78, doi:https://doi.org/10.1016/j.jastp.2016.11.006, layered Phenomena in the Mesopause Region.

Fritts, D. C., W. Dong, T. S. Lund, S. Wieland, and B. Laughman (2020), Self-acceleration and instability of gravity wave packets: 3. three-dimensional packet propagation, secondary gravity waves, momentum transport, and transient mean forcing in tidal winds, *J. Geophys. Res. Atmos.*, *125*(3), e2019JD030,692, doi: https://doi.org/10.1029/2019JD030692.

Fritts, D. C., L. Wang, T. S. Lund, S. A. Thorpe, C. B. Kjellstrand, B. Kaifler, and N. Kaifler (2022a), Multi-scale kelvin-helmholtz instability dynamics observed by pmc turbo on 12 july 2018: 2. dns modeling of khi dynamics and pmc responses, *J. Geophys. Res. Atmos.*, *127*(18), e2021JD035,834, doi:https://doi.org/10.1029/2021JD035834.

Fritts, D. C., L. Wang, T. Lund, and S. Thorpe (2022b), Multi-scale dynamics of kelvin–helmholtz instabilities. part 1. secondary instabilities and the dynamics of tubes and knots, *J. Fluid Mech.*, *941*, A30, doi:10.1017/jfm.2021.1085.

Fritts, D. C., L. Wang, S. Thorpe, and T. Lund (2022c), Multi-scale dynamics of kelvin–helmholtz instabilities. part 2. energy dissipation rates, evolutions and statistics, *J. Fluid Mech.*, *941*, A31, doi:10.1017/jfm.2021.1086.

Fua, D., G. Chimonas, F. Einaudi, and O. Zeman (1982), An analysis of wave-turbulence interaction, *J. Atmos. Sci.*, *39*(11), 2450–2463, doi:10.1175/1520-0469(1982)039<2450:AAOWTI>2.0.CO;2.

Hines, C. O. (1991), The saturation of gravity waves in the middle atmosphere. part i: Critique of linear-instability theory, *J. Atmos. Sci.*, *48*, 1348–1359, doi:10.1175/1520-0469(1991)048<1348:TSOGWI>2.0.CO;2.

Hunt, J. C. R., J. C. Kaimal, and J. E. Gaynor (1985), Some observations of turbulence structure in stable layers, *Q J R Meteorol Soc.*, *111*(469), 793–815, doi: https://doi.org/10.1002/qj.49711146908.

Klostermeyer, J. (1991), Two- and three-dimensional parametric instabilities in finite-amplitude internal gravity waves, *Geophys. Astrophys. Fluid Dyn.*, *61*(1-4), 1–25, doi: 10.1080/03091929108229035.

Koch, S. E., B. D. Jamison, C. Lu, T. L. Smith, E. I. Tollerud, C. Girz, N. Wang, T. P. Lane, M. A. Shapiro, D. D. Parrish, and O. R. Cooper (2005), Turbulence and gravity waves within an upper-level front, *J. Atmos. Sci*, *62*(11), 3885 – 3908, doi: 10.1175/JAS3574.1.

Koudella, C. R., and C. Staquet (2006), Instability mechanisms of a two-dimensional progressive internal gravity wave, *J. Fluid Mech*, *548*, 165–196, doi: 10.1017/S0022112005007524.

Lelong, M. P., and J. J. Riley (1991), Internal wave—vortical mode interactions in strongly stratified flows, *J. Fluid Mech.*, *232*, 1–19, doi:10.1017/S0022112091003609.

Lindzen, R. S. (1967), Thermally driven diurnal tide in the atmosphere, *Q J R Meteorol Soc.*, *93*(395), 18–42, doi:https://doi.org/10.1002/qj.49709339503.

Lindzen, R. S. (1968), Rossby waves with negative equivalent depths – comments on a note by g. a. corby, *Q J R Meteorol Soc.*, *94*(401), 402–407, doi: https://doi.org/10.1002/qj.49709440116.

Lindzen, R. S. (1971), Equatorial planetary waves in shear. part i, *J. Atmos. Sci.*, *28*(4), 609 – 622, doi:10.1175/1520-0469(1971)028<0609:EPWISP>2.0.CO;2.

Lindzen, R. S. (1981), Turbulence and stress owing to gravity wave and tidal breakdown, *J. Geophys. Res. Oceans*, *86*(C10), 9707–9714, doi: https://doi.org/10.1029/JC086iC10p09707.

Liu, X., J. Xu, H.-L. Liu, and R. Ma (2008), Nonlinear interactions between gravity waves with different wavelengths and diurnal tide, *J. Geophys. Res. Atmos.*, *113*(D8), doi: https://doi.org/10.1029/2007JD009136.

Liu, X., J. Xu, H.-L. Liu, J. Yue, and W. Yuan (2014), Simulations of large winds and wind shears induced by gravity wave breaking in the mesosphere and lower thermosphere (MLT) region, *Ann. Geophys.*, *32*(5), 543–552, doi:10.5194/angeo-32-543-2014.

Pairaud, I., C. Staquet, J. Sommeria, and M. M. Mahdizadeh (2010), Generation of harmonics and sub-harmonics from an internal tide in a uniformly stratified fluid: numerical and laboratory experiments, in *IUTAM Symposium on Turbulence in the Atmosphere and Oceans*, edited by D. Dritschel, pp. 51–62, Springer Netherlands, Dordrecht.

Palmer, A. J. (1996), A spectral model for turbulence and microphysics dynamics in an ice cloud, *Nonlinear Process Geophys*, *3*(1), 23–28, doi:10.5194/npg-3-23-1996.

Reiter, E. R. (1969), Structure of vertical wind profiles, *Radio Science*, *4*(12), 1133–1136, doi:https://doi.org/10.1029/RS004i012p01133.

Reynolds, W. C., and A. K. M. F. Hussain (1972), The mechanics of an organized wave in turbulent shear flow. part 3. theoretical models and comparisons with experiments, *J. Fluid Mech.*, *54*(2), 263–288, doi:10.1017/S0022112072000679.

Sedlak, R., P. Hannawald, C. Schmidt, S. Wúst, M. Bittner, and S. Stanič (2021), Gravity wave instability structures and turbulence from more than 1.5 years of oh* airglow imager observations in slovenia, *Atmospheric Measurement Techniques*, *14*(10), 6821–6833, doi:10.5194/amt-14-6821-2021.

Sun, J., C. J. Nappo, L. Mahrt, D. Belušić, B. Grisogono, D. R. Stauffer, M. Pulido, C. Staquet, Q. Jiang, A. Pouquet, C. Yagüe, B. Galperin, R. B. Smith, J. J. Finnigan, S. D. Mayor, G. Svensson, A. A. Grachev, and W. D. Neff (2015), Review of wave-turbulence interactions in the stable atmospheric boundary layer, *Rev. Geophys*, *53*(3), 956–993, doi:https://doi.org/10.1002/2015RG000487.

Sutherland, B. R. (2010), *Internal Gravity Waves*, Cambridge University Press, doi: 10.1017/CBO9780511780318.

Werne, J., and D. C. Fritts (1999), Stratified shear turbulence: Evolution and statistics, *Geophys. Res. Lett.*, *26*(4), 439–442, doi:https://doi.org/10.1029/1999GL900022.

Winters, K. B., and J. J. Riley (1992), Instability of internal waves near a critical level, *Dyn. Atmospheres Oceans*, *16*(3), 249–278, doi:https://doi.org/10.1016/0377-0265(92)90009-I.

Yang, F., and A. Z. Liu (2022), Stability characteristics of the mesopause region above the andes, *J. Geophys. Res. Space Phys.*, *127*(9), e2022JA030,315, doi: https://doi.org/10.1029/2022JA030315.

Yim, E., P. Meliga, and F. Gallaire (2019), Self-consistent triple decomposition of the turbulent flow over a backward-facing step under finite amplitude harmonic forcing, *Proc. R. Soc. A*, *475*(2225), 20190,018, doi:10.1098/rspa.2019.0018.

Zovko-Rajak, D., T. P. Lane, R. D. Sharman, and S. B. Trier (2019), The role of gravity wave breaking in a case of upper-level near-cloud turbulence, *Mon. Weather Rev.*, *147*(12), 4567 – 4588, doi:10.1175/MWR-D-18-0445.1.

Analysis of Energy Transfer among Background Flow, Gravity Waves and Turbulence in the mesopause region in the process of Gravity Wave Breaking from a High-resolution Atmospheric Model

Fan Yang[1],[*] **Wenjun Dong**[1,2], **Thomas Lund**[2], **Alan Z. Liu**[1], **Christopher Heale**[1], **Jonathan B. Snively**[1]

[1] Center for Space and Atmospheric Research, Department of Physical Sciences, Embry-Riddle Aeronautical University, Daytona Beach, FL, USA.

[2] GATS, Boulder, CO, USA.

Key Points:

- The energy flow during a GW breaking case was investigated via a high-resolution atmospheric model.
- The wave-flow interactions dominate the wave-breaking energy-transferring process.
- Kinetic energy in background, gravity wave, and turbulence transfer among each other through nonlinear interactions.

[*]Department of Physical Sciences, Embry-Riddle Aeronautical University, 1 Aerospace Blvd, Daytona Beach, FL 32114-3900, USA

Abstract

We conducted an analysis of the process of GW breaking from an energy perspective using the output from a high-resolution compressible atmospheric model. The investigation focused on the energy conversion and transfer that occur during the GW breaking. The total change in kinetic energy and the amount of energy converted to internal energy and potential energy within a selected region were calculated. Prior to GW breaking, part of the potential energy is converted into kinetic energy, most of which is transported out of the chosen region. After the GW breaks and turbulence develops, part of the potential energy is converted into kinetic energy, most of which is converted into internal energy. The calculations for the transfer of kinetic energy among GWs, turbulence, and the BG in a selected region, as well as the contributions from various interactions (BG-GW, BG-turbulence, and GW-turbulence), are performed. At the point where the GW breaks, turbulence is generated. As the GW breaking process proceeds, the GWs lose energy to the background. At the start of the GW breaking, turbulence receives energy through interactions between GWs and turbulence, and between the BG and turbulence. Once the turbulence has accumulated enough energy, it begins to absorb energy from the background while losing energy to the GWs. The probabilities of instability are calculated during various stages of the GW-breaking process. The simulation suggests that the propagation of GWs results in instabilities, which are responsible for the GW breaking. As turbulence grows, it reduces convective instability.

1 Plain language

In this study, we utilized a high-resolution atmospheric model to analyze the energy flow of a gravity breaking event. Our main focus was to examine the conversion and transfer of energy during this process, and to investigate how it moves between gravity waves, turbulence, and the background atmosphere. To accomplish this, we formulated change rate equations for the kinetic energy tendencies of turbulence, gravity waves, and background flow, and assessed how various processes and interactions contribute to the kinetic energy change rate. Our findings reveal that when gravity waves break, they lose energy to the background flow, while turbulence gains energy from interactions with both gravity waves and the background flow. Additionally, we calculated the conversion and transfer of energy during the gravity wave breaking process and discovered that potential energy transforms into kinetic energy both before and after the gravity wave breaking.

Furthermore, we evaluated the probability of instabilities occurring during different stages of the gravity wave breaking and found that turbulence can diminish convective instability as it grows.

2 Introduction

Gravity wave (GW) breaking plays an important role in depositing the momentum and energy in GWs to the background mean flow. [*Lindzen*, 1981; *Dunkerton and Fritts*, 1984]. GW breaking process is related to GW propagation, turbulence, interactions of different scales, and instabilities.

A complete quantification of GW breaking dynamics and consequences requires direct numerical simulation (DNS). *Barat and Genie* [1982] and *Hunt et al.* [1985] suggested that the atmosphere has a vertical structure characterized by strong stable 'sheet' and less stable 'layers'. The S&L structures play an important role in the transport and mixing of heat, momentum, and constituents. The formation mechanisms of S&L structures arising from superposition of stable GWs and mean shears are referred as 'Multi-scale dynamics' (MSD). MSD drives S&L structure and evolutions. MSD includes KHI, GW breaking, and fluid intrusions [*Fritts et al.*, 2013a].

Among all physical processes during GW breaking, the mechanism of turbulence development is one of the most important scientific topics because of its effects on weather, climate, aircraft, and atmospheric observations[*Reiter*, 1969]. Turbulent flows develop spinning or swirling fluid structures called eddies[*Doran*, 2013]. *Winters and Riley* [1992] found a major source of eddy kinetic energy (KE) would be buoyancy. Besides the buoyancy terms, large shears in the mean and GW motion fields also contribute to the formation of eddy structures. The vertical shear is the dominant source of eddy KE after the initial wave collapse. The pressure-work terms contribute very little to the eddy KE [*Fritts et al.*, 1994]. *Palmer* [1996]; *Fritts et al.* [1996], and *Werne and Fritts* [1999] studied the dynamics of turbulence generation due to KH instability. *Fritts and Alexander* [2003] suggested turbulence arises mainly due to Kelvin-Helmholz (KH) shear instability and GW breaking. KH shear is more common at lower altitudes such as the troposphere and stratosphere. GW breaking is more important at higher altitudes and is the dominant source in the mesosphere. *Achatz* [2007] emphasized that the 'statically enhanced roll mechanism' is a strong contributor to the tendency of turbulence energy. GW-breaking and KHI play major roles in leading to strong turbulence. Fluid intrusions play more significant roles following the initial KHI [*Fritts et al.*, 2016, 2017a]. *Fritts et al.* [2017b] and *Dong et al.* [2022] explored the dynamics of GW encountering a mesospheric inversion layer (MIL). They found mean fields are driven largely by 2D GW and instability dynamics. They implicated that turbulence due to GW overturning arises in a transient phase of the GW that has weak convective stability. Further exploring of KHI leads to cases of 'tube and knot' (T&K) dynamics. T&K dynamics accelerate the transition from KH billow to turbulence. It may also enable strong turbulence to occur at large Richardson numbers [*Fritts et al.*, 2022a].

Besides DNS studies, multiple observational studies have been conducted to reveal the mechanisms of turbulence generation. *Lindzen* [1967, 1968] noted the possible mechanism of turbulence generation from wave breaking in the mesosphere. *Lindzen* [1971, 1981] argued that 'turbulent' diffusion could also result from nonbreaking waves. *Atlas and Bretherton* [2022] used aircraft measurements to correlate gravity waves (GWs) and turbulence with tropical tropopause layer cirrus. They found during their observation, turbulence co-occurred with GWs 95 % of the time. Observations also suggest that the dynamics of GW energy dissipation often involve 'sheet and layer' (S&L) structures [*Fritts et al.*, 2004; *Clayson and Kantha*, 2008; *Fritts et al.*, 2017a]. *Zovko-Rajak et al.* [2019] found near-cloud turbulence is associated with strong GWs generated by moist convection.

Nonlinear interactions are crucial in the GW-breaking process. Multiple nonlinear saturation theories were proposed [*Dunkerton*, 1987; *Klostermeyer*, 1991; *Hines*, 1991; *Fritts et al.*, 2003] to explain the relationships between instabilities and nonlinear interactions that are not accounted for in a linear theory. Both mechanisms helped to explain the wave-breaking processes and instabilities. Nonlinearity mainly includes the interactions among wave, turbulence, vortex, and background flow [*Lelong and Riley*, 1991; *Bühler*, 2010; *Fritts et al.*, 2015; *Dong et al.*, 2020; *Fritts et al.*, 2020]. Wave-turbulence interactions can modify primary wave amplitudes [*Fua et al.*, 1982; *Einaudi and Finnigan*, 1993]. Wave breaking, which can be triggered by wave-mean flow interactions [*Sutherland*, 2010; *Pairaud et al.*, 2010], is one of the most common mechanisms for turbulence generation. *Koch et al.* [2005] found that GWs and turbulence are often observed simultaneously due to GW instability being the source of turbulence. Their research showed that turbulence intensity did not vary with wave phase. They also discovered that turbulence is mostly forced at a horizontal scale of 700 m, with energy from both larger and smaller scales being transferred to this scale. Two-dimensional model result [*Liu et al.*, 2014] showed that the momentum deposited by breaking GWs accelerates the mean wind. GW breaking accelerates the background wind suggesting that the nonlinear interactions increase the tidal amplitude [*Liu et al.*, 2008]. *Fritts et al.* [2013b] revealed 2D wave-wave interactions are the only (sole) cause of the decrease of primary GW amplitude. They conclude that turbulence is highly dependent on the orientation of the GW. *Barbano et al.* [2022] evaluated the wave-turbulence interaction through triple decomposition [*Reynolds and Hussain*, 1972; *Finnigan and Einaudi*, 1981; *Finnigan et al.*, 1984] focusing on the production of turbulence momentum flux and wave shear or vorticity, which is one part of the wave-turbulence interaction. This particular aspect of wave-turbulence interactions can cause both the production and destruction of turbulent energy.

GW breaking is often associated with instabilities, which can induce its occurrence, as noted by *Sedlak et al.* [2021]. *Achatz* [2007] discussed how singular vectors (SVs) can destabilize statically and dynamically stable low-frequency inertia-GWs, while normal modes (NMs) destabilize can statically stable high-frequency GWs. In an observatory study, *Yang and Liu* [2022] reported GW instabilities and their relationship with GW frequencies using ALO lidar measurements.

There have been a number of research on mechanisms for GW breaking. Most studies focus on the dynamical process, not on the energetics of this process. The energetics provides important insights of the growth and delay of different components in the interactions. Many studies also focus on how wave breaks into turbulence, but not how turbulence influences the wave and/or the background. This work looks at all three components together from the energy perspective, and not just on the initial breaking of a wave, but also the eventual decay of the turbulence. Physical understanding of nonlinear interactions is still lacking. Improved understanding is critical for weather and environmental forecasts [*Sun et al.*, 2015].

The primary purpose of this paper is to study the dynamics of a GW breaking and assess the roles played by GWs and their background (BG) flow in the process. The objectives of this paper are to quantify the energy conversion among kinetic energy (KE), potential energy (PE), and internal energy (IE) and to determine the contributions to turbulence generation from nonlinear interactions of various scales and their energy transfer directions during a gravity wave breaking process. The structure of this study is as follows: In Section 2, we introduce the model and its inputs used in the study. Section 3 outlines the methodology of our analysis. The results, including the findings on energy conversions, the transfer of kinetic energy (KE) among the background, GWs, and turbulence, and the connection between instabilities and GW breaking, are presented in Section 4. The results are discussed in detail in Section 5. The conclusions of the study are summarized in Section 6. Finally, Appendixes A and B present the derivations of the formulations used in Section 3.

3 Model Description

The model used for this study is the Complex Geometry Compressible Atmospheric Model (CGCAM) described extensively by *Dong et al.* [2020] (hereafter D20). CGCAM satisfies the numerical conservation of mass, momentum, and kinetic and thermal energies since it discretizes the compressible Navier-Stokes equations [*Felten and Lund*, 2006]. See D20 for additional details.

As for background, a uniform temperature profile, $T_0(z) = 300$ K, is used which yields a scale height $H \sim 8.9$ km, a buoyancy frequency $N \sim 0.018$ s^{-1}. To make the model results comparable to lidar observation, the vertical wavelength is chosen to be 15 km. Therefore, the initial GW has a horizontal wavelength $\lambda_x = 45$ km, a vertical wavelength $\lambda_z = 15$ km, and a horizontal intrinsic phase speed $ci = -u_0(z) = -40.1$ m/s, which results in an intrinsic wave period of $2\pi/\omega = \lambda_x/ci = 1122$ s. The initial GW packet is introduced into the domain by specifying the streamwise velocity distribution. See detail in D20.

The simulations used here are performed in a Cartesian computational domain. The computational domains extend from -150 km to 150 km in the streamwise (x) direction and from 0 km to 170 km in the vertical (z) direction. The resolutions Δx and Δz in the zone of instability, GW breaking, and turbulence are both 300 m. Periodic boundary conditions are used in the x direction. Isothermal no-stress wall conditions are used at the lower boundary and a characteristic radiation boundary condition is used at the upper boundary. Numerical sponge layers are used at all boundaries to absorb the energy of outgoing fluctuations. The sponge layers are 20 km deep at the upper boundary, 5 km deep at the lower boundary, and 10 km wide at the streamwise boundaries. The sponges work as force terms added to conservation equations. See details in equation (33) in D20.

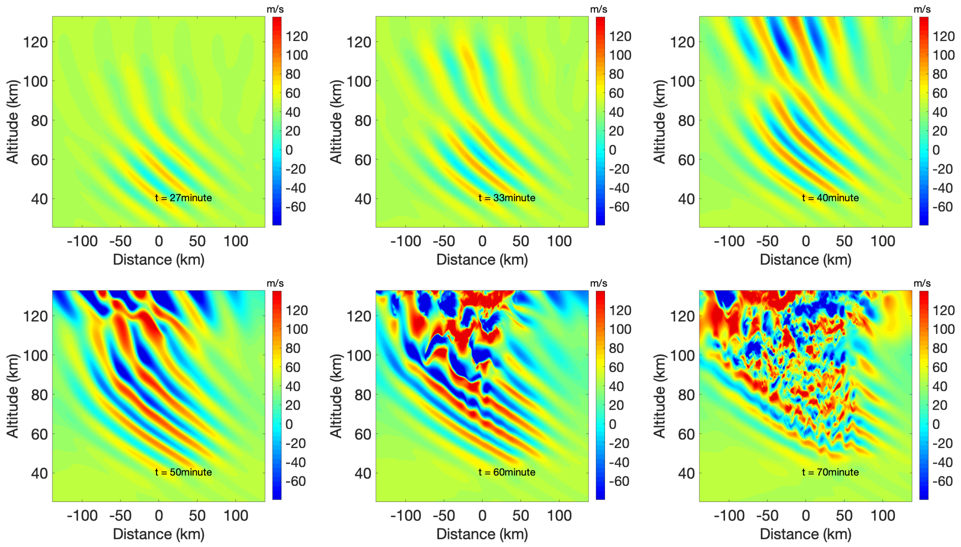

Figure 1: u (m/s) generated by 2D CGCAM at 6 times. They represent the horizontal wind speed in sequence from left to right, and from top to bottom, at the 27th, 33rd, 40th, 50th, 60th, and 70th minutes, respectively.

The output of CGCAM is used to investigate the energy transfer among turbulence, GWs, and background flow. The outputs of CGCAM are ρ, ρu, ρw and ρE. With ideal gas law, the temperature T, horizontal wind speed u, vertical wind speed w, pressure p, and density ρ can be derived. u at six different times are presented in Figure 1 as an example to depict the wave-breaking process. The initial condition for the simulation is a single GW with horizontal and vertical wavelengths of 45 km and 15 km, respectively. This study investigates the GW breaking process at the mesopause region. Thus, the activities in a 45 km-horizontal (-22.5 km - 22.5 km) and 15 km-vertical region at mesopause region (85 km - 100 km) are studied. In this chosen region, the GWs start to break around the 56th minute.

4 Methodology

Energy transfers studied in this paper include two sets. One set is energy conversion between KE, IE, and PE of the atmosphere. The other set is the kinetic energy transfer among BG, GWs, and turbulence.

4.1 Energy Conversion

Energy conversions are related to total KE, IE, and PE tendencies. The energy tendencies of KE, IE, and PE are:

$$\begin{aligned}\frac{\partial KE}{\partial t} &= -\nabla \cdot (KE\vec{v}) - \vec{v} \cdot \nabla p - g\rho w \\ &= -\nabla \cdot (KE\vec{v}) - \nabla \cdot (p\vec{v}) + p\nabla \cdot \vec{v} - g\rho w,\end{aligned} \tag{1}$$

$$\begin{aligned}\frac{\partial IE}{\partial t} &= -\mathrm{C_v}T(\vec{v} \cdot \nabla\rho + \rho\nabla \cdot \vec{v}) - p\nabla \cdot \vec{v} - \mathrm{C_v}\rho\vec{v} \cdot \nabla T + \kappa\nabla^2 T \\ &= -\nabla \cdot (IE\vec{v}) - p\nabla \cdot \vec{v},\end{aligned} \tag{2}$$

$$\begin{aligned}\frac{\partial pE}{\partial t} &= gh\frac{\partial \rho}{\partial t} + g\rho w = -gh\left(\vec{v} \cdot \nabla\rho + \rho\nabla \cdot \vec{v}\right) + g\rho w \\ &= -\nabla \cdot (PE\vec{v}) + g\rho w,\end{aligned} \tag{3}$$

where $\mathrm{C_v}$ is the specific heat at constant volume. κ is the conductivity, and κ is not a constant. See details and deductions for the energy tendencies in Appendix A.

PE, KE, and IE vary through transportation and conversions among each other. KE tendency is related to the divergence/convergence of KE flux ($-\nabla \cdot (KE\vec{v})$), air expansion/compression ($-\nabla \cdot (p\vec{v})$), pressure doing work on air expansion/compression ($p\nabla \cdot \vec{v}$), and gravity force doing work ($-g\rho w$). IE tendency is related to the divergence/convergence of IE flux ($-\nabla \cdot (IE\vec{v})$) and pressure doing work on air expansion/compression ($-p\nabla \cdot \vec{v}$). PE tendency is related to the divergence/convergence of PE flux ($-\nabla \cdot (PE\vec{v})$) and gravity force doing work on air expansion/compression ($g\rho w$). KE tendency and IE tendency are related through the term $(\pm)p\nabla \cdot \vec{v}$. KE tendency and PE tendency are related through the term $(\mp)\rho gW$. The conversion between KE and IE occurs through pressure doing work on flow expansion/compression. The conversion between KE and PE is through gravity force doing work.

4.2 Kinetic Energy Transfer between Background and Perturbations

A typical approach for analyzing flow motion is to decompose the perturbation from the mean flow [*Reynolds and Hussain*, 1972; *Finnigan and Einaudi*, 1981; *Yim et al.*, 2019; *Barbano et al.*, 2022]. A variable or product of variables Q is divided into a BG-period-average (BPA) value (Q_0) and a fluctuation (Q_1) whose BPA value is zero, where BPA is defined as the temporal average over the period of the wave or perturbation. The BPA is indicated by the overline symbol $\overline{Q}$.

The calculation of KE tendency involves the process of decomposition. The transfer of KE between the BG and perturbations can be demonstrated through the examination of their respective KE tendencies. The background and the perturbation KE tendencies yield (See deductions in Appendix B):

$$\begin{aligned}\frac{\partial KE_0}{\partial t} + \rho_0 u_0 u_0 \frac{\partial u_0}{\partial x} + \rho_0 w_0 w_0 \frac{\partial w_0}{\partial z} + \rho_0 w_0 u_0 (\frac{\partial w_0}{\partial x} + \frac{\partial u_0}{\partial z}) \\ + \rho_0 u_0 \overline{\vec{v_1} \cdot \nabla u_1} + \rho_0 w_0 \overline{\vec{v_1} \cdot \nabla w_1} \\ = -\vec{v_0} \cdot \nabla p_0 + \vec{v_0} \cdot \overline{\frac{\rho_1}{\rho_0} \nabla p_1} - \rho_0 g w_0,\end{aligned} \tag{4}$$

$$\begin{aligned}\frac{\partial KE_1}{\partial t} + \rho_0 u_1 \vec{v_1} \cdot \nabla u_0 + \rho_0 u_1 \vec{v_0} \cdot \nabla u_1 + \rho_0 u_1 \vec{v_1} \cdot \nabla u_1 \\ + \rho_0 w_1 \vec{v_1} \cdot \nabla w_0 + \rho_0 w_1 \vec{v_0} \cdot \nabla w_1 + \rho_0 w_1 \vec{v_1} \cdot \nabla w_1 \\ = -\vec{v_1} \cdot \nabla p_1 + \frac{\vec{v_1} \rho_1}{\rho_0} \cdot \nabla p_0 + \frac{\vec{v_1} \rho_1}{\rho_0} \cdot \nabla p_1 \\ + \rho_0 u_1 \overline{\vec{v_1} \cdot \nabla u_1} + \rho_0 w_1 \overline{\vec{v_1} \cdot \nabla w_1} - u_1 \overline{\frac{\rho_1}{\rho_0} \frac{\partial p_1}{\partial x}} - w_1 \overline{\frac{\rho_1}{\rho_0} \frac{\partial p_1}{\partial z}},\end{aligned} \tag{5}$$

where $\vec{v}$ is the wind velocity.

In order to demonstrate the variations in KE across different scale perturbations, proper BPAs must be applied to the tendency equations. Following the principle of triple decomposition, the variables are separated into turbulence, GWs, and BG [*Reynolds and Hussain*, 1972; *Finnigan and Einaudi*, 1981; *Yim et al.*, 2019; *Barbano et al.*, 2022]. The contributions to the energy change rate through different mechanics are analyzed, and the energy transfer among BG, GWs, and turbulence is studied. The triple decomposition for BG, GWs, and turbulence is based on their respective periods. The initial input is a single GW with a period of about 20 minutes. This period of 20 minutes is used to differentiate between the BG and the GWs. In terms of turbulence, there is no well-defined boundary between the GWs and turbulence. Fluctuations with periods less than 3 minutes are considered to be turbulence in this study. The selection of 3 minutes is based on the following considerations. On one hand, this period includes as much turbulence as possible. On the other hand, this study focuses on isotropic turbulence. CGCAM velocity output shows isotropic velocity fluctuations with periods shorter than around 3 minutes. As a result, 3-min averaged data is considered as the background for the turbulence perturbation, which encompasses GW perturbations and the slower varying 20-min averaged data.

During the GW breaking process, nonlinear physical terms play important roles in the energy transfer between different scales. As demonstrated by (5), the instantaneous

KE_1 tendency is related to various nonlinear terms, including flow expansion or compression, the products of perturbation momentum flux and BG shear, advection, and the pressure gradient force doing work. These nonlinear terms are derived to study the energy transfer process among turbulence, GWs, and BG. Linear terms, such as products of linear perturbation variables and BPA nonlinear products, represented by the last four terms in (5), will average to zero when the proper BPAs are applied.

4.3 Instability parameters

Probabilities of dynamic instabilities (PDI) and convective instabilities (PCI) [*Yang and Liu*, 2022] are used to depict the variation of instabilities in the chosen region. PCI and PDI represent the likelihood of occurrences of the negative values of the square of buoyance frequency and the values of Richardson number between 0 and 0.25. Further details can be found in *Yang and Liu* [2022].

5 Results

5.1 KE, IE and PE Conversions during GW breaking process

The KE, IE, and PE changes with respect to time are depicted in Figure 2. The energy changes are calculated as integrals of corresponding energy changes over the specified spatial domain. The blue solid lines in the left, middle, and right plots represent the total KE, IE, and PE variations derived from 2-s-resolution data, respectively. The red solid lines in these three plots depict the total KE, IE, and PE variations after a 20-min moving average with a 1.5-minute step. The vertical black lines mark the 56th minute, which is when the GWs start to break in the chosen region. The background values have been subtracted in IE and PE plots to highlight the variation. Before the start of the GW breaking process, the KE increases by approximately 400 J, while the IE and PE decrease by approximately 3000 J and 5000 J, respectively. The small variation in KE compared to the variations in IE and PE suggests that the energy change is primarily due to energy transport or advection, with the net effect of energy conversion being negligible.

Energy conversion is related to KE tendency. The right-hand side terms of KE tendency are presented in Figure 3. Based on (3), the energy conversion between KE and PE, and KE and IE, $p\nabla\cdot\vec{v}$ and $\rho g W$ are computed. The left plot depicts the energy change due to different physical processes, and the right plot depicts the corresponding energy change

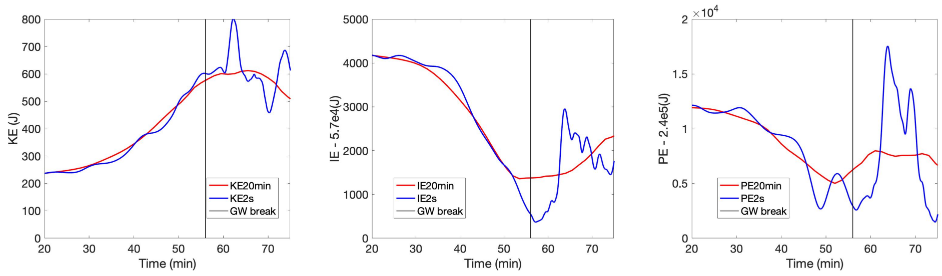

Figure 2: The integrals of KE, IE and PE over the chosen region. The three blue solid lines represent KE, IE, and PE obtained from 2-s resolution data. The three red solid lines show the results after applying 20-min moving averaging with 1.5-min step. GW breaking starts at the 56th minute marked by vertical black solid lines.

rate. The blue dashed line shows the integration of $-\rho g W$, which is the KE change converted from PE. The red dashed line is the KE change due to conversion from IE. The green solid line shows the KE change due to energy transport in the chosen region. The magenta solid line depicts the KE change due to air expansion or compression. During the first 60 minutes, roughly 2500 J of PE is converted into KE. During the same interval, only a limited amount of energy is converted into IE. The primary source of energy changes caused by fluid expansion or compression is from the work performed by the pressure gradient force. The process transported approximately 1500J of energy out of this region. During the period between the 60th and 63rd minutes, about 2500 J of KE is converted to PE, as indicated by the blue dashed line in the left top plot. Around 1500 J of IE is converted into KE, as depicted by the red dashed line in the same plot. During this 5-min interval, there is limited energy change resulting from the pressure gradient force doing work since the energy change by $-\nabla \cdot (p\vec{v})$ is about 1500 J as shown by the magenta solid line in the left top plot. Between the 63rd and 69th minutes, all factors in the right-hand side of KE tendency are relatively small compared with the tendency between 60th and 63rd minutes, and the tendency after the 69th minute. After the 69th minute, the primary source of energy variation caused by fluid expansion is the loss of energy into IE, as depicted by the red dashed line in the right top plot. The main increase of KE is a result of conversion from PE, as shown by the blue dashed line in the same plot.

KE tendency due to KE flux divergence is separated into its horizontal and vertical parts, as shown in the bottom 2 plots in Figure 3. The left plot illustrates the energy

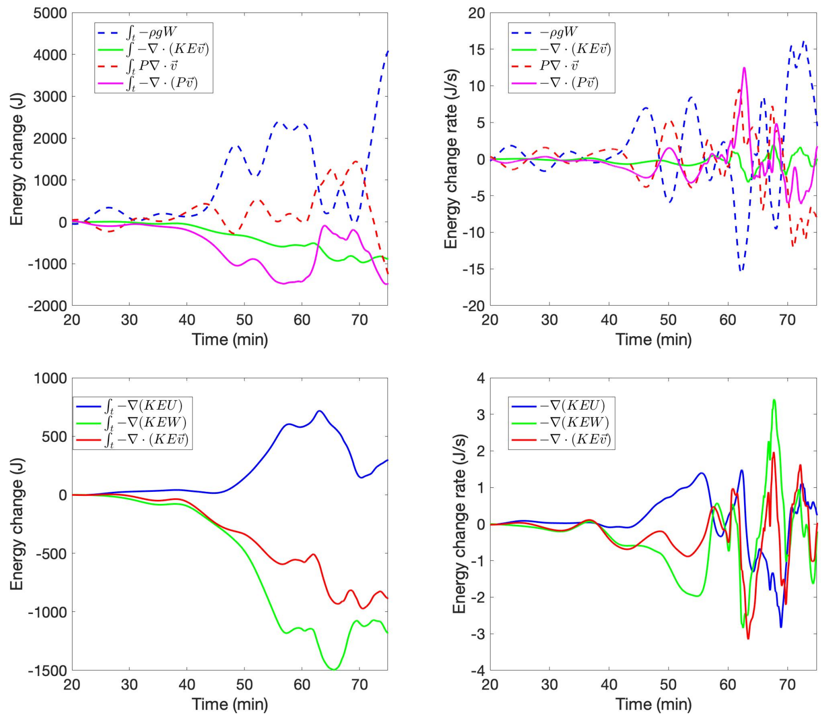

Figure 3: KE change and KE change rate due to forces. The top 2 plots depict the KE change and KE change rate due to conversion and the divergence of KE flux. The bottom 2 plots depict the horizontal and vertical components of KE change and KE change rate due to the divergence of KE flux. The energy changes depicted in the left plots are obtained by integrating the energy change rates over time. The energy change rates displayed in the right plots are obtained through the integration of energy change rates over the selected spatial domain.

change caused by various physical processes, while the right plot shows the corresponding energy change rate. The red solid lines represent the KE change and KE change rate due to the divergence of KE flux. The blue solid lines represent the KE change and KE change rate resulting from KE flux convergence through left and right boundaries. The green solid lines represent the KE change and KE change rate caused by KE divergence flux through the bottom and top boundaries. KE in the chosen region is reduced by approximately 2000 J due to the vertical KE flux, and increased by about 1500 J due to the horizontal KE flux. Prior to the 56th minute, the magnitude of convergence of horizontal KE flux and the divergence of vertical KE flux both increase. During the period from the 56th minute to the 75th minute, the variation is fast and substantial. Between the 70th minute and the 90th minute, the vertical KE flux continues to diverge and the horizontal KE flux continues to converge. After the 90th minute, the divergence or convergence of KE flux is almost negligible. The energy transported by the flux remains unchanged, which suggests the velocity field has been mixed uniformly on a 15km scale. The GW source in the simulation is below the chosen region. At this height region, most energy transport occurs through the horizontal KE flux, which absorbs energy into this region from the left and right boundaries.

5.2 Energy Transfer among BG, GWs, and Turbulence

KE in BG, GW, and turbulence transfer among each other through nonlinear interactions. These interactions play different roles at different times causing KE to vary. In this section, the general variations of KE in BG, GW, and turbulence over the entire GW breaking process are discussed. More detailed analyses are provided for the interval when GW begins to break. KE in 20-minute BG, KE in GW, and KE in turbulence are denoted by KE_0, KE_{GW}, and KE_{turb}, respectively.

5.2.1 Mean Flow KE Tendency

Following (4), the equation for KE_0 tendency is as follows:

$$\begin{aligned}\frac{\partial KE_0}{\partial t} &= -\rho_0 u_0 u_0 \frac{\partial u_0}{\partial x} - \rho_0 w_0 w_0 \frac{\partial w_0}{\partial z} \\ &\quad -\rho_0 w_0 u_0 \left(\frac{\partial w_0}{\partial x} + \frac{\partial u_0}{\partial z}\right) \\ &\quad -\rho_0 u_0 \overline{\vec{v_1} \cdot \nabla u_1}^{20\text{min}} - \rho_0 w_0 \overline{\vec{v_1} \cdot \nabla w_1}^{20\text{min}} \\ &\quad -\vec{v_0} \cdot \nabla p_0 + \vec{v_0} \cdot \overline{\frac{\rho_1}{\rho_0} \nabla p_1}^{20\text{min}} - \rho_0 g w_0.\end{aligned} \tag{6}$$

KE_0 change can be examined by integrating over time. The energy changes are calculated as the integrals of energy change rates over time. The energy change rates are obtained by integrating the energy change rates over the selected spatial domain. In (6), $-\rho_0 u_0 u_0 \frac{\partial u_0}{\partial x} - \rho_0 w_0 w_0 \frac{\partial w_0}{\partial z}$ is the KE_0 change due to BG air expansion or compression. $-\rho_0 w_0 u_0 (\frac{\partial w_0}{\partial x} + \frac{\partial u_0}{\partial z})$ is the KE_0 change due to BG wind shear. $-\rho_0 u_0 \overline{\vec{v_1} \cdot \nabla u_1}^{20\text{min}} - \rho_0 w_0 \overline{\vec{v_1} \cdot \nabla w_1}^{20\text{min}}$ depicts how BG changes due to nonlinear interactions of perturbations. $-\vec{v_0} \cdot \nabla p_0$ and $-\rho_0 g w_0$ depict the work by pressure gradient force and gravity force, respectively. $\vec{v_0} \cdot \overline{\frac{\rho_1}{\rho_0} \nabla p_1}^{20\text{min}}$ depicts the perturbation pressure gradient averaged effect on KE_0 change, which is another form of nonlinear interaction of perturbations.

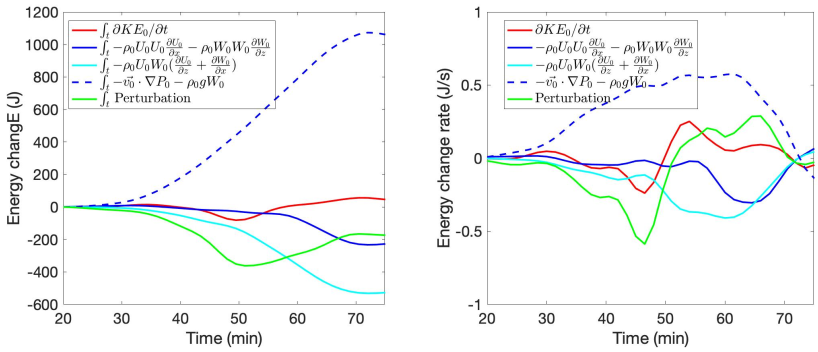

Figure 4: KE_0 change and change rate over the chosen domain. The left plot is the integration of force terms for KE_0 change rate. The right plot is the work done by force terms for KE_0 change. The energy changes depicted in the left plot are obtained by integrating the energy change rates over time. The energy change rates displayed in the right plot are obtained through the integration of energy change rates over the selected spatial domain.

The KE_0 change and change rate are shown in Figure 4. The energy changes depicted in the left plots are obtained by integrating the energy change rates over time. The energy change rates displayed in the right plots are obtained through the integration of energy change rates over a selected spatial domain. The energy changes caused by various mechanisms are described as follows. The evolution of KE_0 is depicted by the red solid line in the left plot. It decreases first and then increases slightly by about 180 J at the end. The only positive contribution to KE_0 comes from the work done by the pressure gradient force and gravity force, as shown by the blue dashed line. On the other hand, the blue solid line, which represents the expansion and compression of the flow, has a negative effect on KE_0. This indicates that the flow is expanding and transporting KE_0 out of the chosen domain. The cyan solid line depicts the product of BG momentum flux and BG wind shear. In general, this term is negative, meaning that the momentum flux and wind shear have the same sign. This process transports flow with smaller/larger momentum to the position of flow with larger/smaller momentum, making the velocity field more uniform and reducing the KE_0. Before the 50th minute, a few minutes before the GW breaking, the averaged nonlinear interactions reduce KE_0, as shown by the green solid line. After GW breaking and turbulence develop, the nonlinear terms have a positive contribution to KE_0 till the 75th minute. The same line types in the right plot depict the corresponding energy change rates.

5.2.2 Perturbation KE Tendency

KE in perturbation (KE_1) here includes KE in turbulence (KE_{turb}) and GWs (KE_{GW}). The background value is a 20-min average background. To accurately capture turbulence fluctuations, a 2-second resolution was used for the data analysis.

$$
\begin{aligned}
\frac{\partial KE_1}{\partial t} &= -\rho_0 u_1 u_1 \frac{\partial u_0}{\partial x} - \rho_0 w_1 w_1 \frac{\partial w_0}{\partial z} - \rho_0 w_1 u_1 (\frac{\partial w_0}{\partial x} + \frac{\partial u_0}{\partial z}) \\
&\quad -\vec{v} \cdot \nabla KE_1 + \frac{\vec{v_1}\rho_1}{\rho_0} \cdot \nabla p_0 + \frac{(\rho_1 - \rho_0)\vec{v_1}}{\rho_0} \cdot \nabla p_1 \\
&\quad +\rho_0 u_1 \overline{\vec{v_1} \cdot \nabla u_1}^{20\text{min}} + \rho_0 w_1 \overline{\vec{v_1} \cdot \nabla w_1}^{20\text{min}} \\
&\quad -u_1 \overline{\frac{\rho_1}{\rho_0} \frac{\partial p_1}{\partial x}}^{20\text{min}} - w_1 \overline{\frac{\rho_1}{\rho_0} \frac{\partial p_1}{\partial z}}^{20\text{min}},
\end{aligned}
\tag{7}
$$

Perturbation Q_1 can be separated into Q_{turb} and Q_{GW}. This allows for an investigation of the variations in both the KE_{turb} and KE_{GW}.

Turbulence KE

The 2 s-resolution data and 3-min BPA is utilized in this study to analyze the turbulence energy and its interaction with GWs and BG. The equation for turbulence is the same as for total perturbation, but the BG for turbulence in this equation is 3 min-resolution data, which includes GWs. The total BG for turbulence (Q_0) is separated into two components: Q_{GW} and Q_{BG}. This allows for the examination of the interactions between turbulence (Q_{turb}) and the BG (Q_{BG}), as well as between turbulence and GWs (Q_{GW}).

$$\begin{aligned}\frac{\partial KE_1}{\partial t} &= -\rho_0 u_1 u_1 \frac{\partial u_0}{\partial x} - \rho_0 w_1 w_1 \frac{\partial w_0}{\partial z} - \rho_0 w_1 u_1 (\frac{\partial w_0}{\partial x} + \frac{\partial u_0}{\partial z}) \\ &-\vec{v} \cdot \nabla KE_1 + \frac{\vec{v_1}\rho_1}{\rho_0} \cdot \nabla p_0 + \frac{(\rho_1 - \rho_0)\vec{v_1}}{\rho_0} \cdot \nabla p_1 \\ &+\rho_0 u_1 \overline{\vec{v_1} \cdot \nabla u_1}^{3\text{min}} + \rho_0 w_1 \overline{\vec{v_1} \cdot \nabla w_1}^{3\text{min}} \\ &-u_1 \overline{\frac{\rho_1}{\rho_0}\frac{\partial p_1}{\partial x}}^{3\text{min}} - w_1 \overline{\frac{\rho_1}{\rho_0}\frac{\partial p_1}{\partial z}}^{3\text{min}},\end{aligned} \tag{8}$$

where the symbol $\overline{Q}^{3\text{min}}$ denotes the 3-minute BPA. To simplify the problem, ρ_1 is assumed to be much smaller than ρ_0. Therefore, $\rho_1 + \rho_0 \sim \rho_0$ and $(\rho_0 - \rho_1)/\rho_0 \sim 1$.

$$\begin{aligned}\frac{\partial KE_{turb}}{\partial t} &= -\rho_0 u_{turb}^2 \frac{\partial (u_{GW} + u_0)}{\partial x} - \rho_0 w_{turb}^2 \frac{\partial (w_{GW} + w_0)}{\partial z} \\ &-\rho_0 w_{turb} u_{turb} (\frac{\partial (w_{GW} + w_0)}{\partial x} + \frac{\partial (u_{GW} + u_0)}{\partial z}) \\ -(\vec{v_{turb}} + \vec{v_{GW}} + \vec{v_0}) \cdot \nabla KE_{turb} &+ \frac{\vec{v_{turb}}\rho_{turb}}{\rho_0} \cdot \nabla (p_{GW} + p_0) - \vec{v_{turb}} \cdot \nabla p_{turb} \\ &+\rho_0 u_{turb} \overline{\vec{v_{turb}} \cdot \nabla u_{turb}}^{3\text{min}} + \rho_0 w_{turb} \overline{\vec{v_{turb}} \cdot \nabla w_{turb}}^{3\text{min}} \\ &-u_{turb} \overline{\frac{\rho_{turb}}{\rho_0}\frac{\partial p_{turb}}{\partial x}}^{3\text{min}} - w_{turb} \overline{\frac{\rho_{turb}}{\rho_0}\frac{\partial p_{turb}}{\partial z}}^{3\text{min}},\end{aligned} \tag{9}$$

Do 3-minute BPA on the KE_{turb} tendency equation and remove the terms averaged to zero yields

$$\begin{aligned}\overline{\frac{\partial KE_{turb}}{\partial t}}^{3\text{min}} &= -\rho_0 \overline{u_{turb}^2 \frac{\partial (u_{GW} + u_0)}{\partial x}}^{3\text{min}} - \rho_0 \overline{w_{turb}^2 \frac{\partial (w_{GW} + w_0)}{\partial z}}^{3\text{min}} \\ &-\rho_0 \overline{w_{turb} u_{turb}}^{3\text{min}} (\frac{\partial (w_{GW} + w_0)}{\partial x} + \frac{\partial (u_{GW} + u_0)}{\partial z}) \\ &-\overline{(\vec{v_{turb}} + \vec{v_{GW}} + \vec{v_0}) \cdot \nabla KE_{turb}}^{3\text{min}} \\ &+\overline{\frac{\vec{v_{turb}}\rho_{turb}}{\rho_0}}^{3\text{min}} \cdot \nabla (p_{GW} + p_0) - \overline{\vec{v_{turb}} \cdot \nabla p_{turb}}^{3\text{min}}.\end{aligned} \tag{10}$$

The last 4 terms in (9) averages to zero ideally theoretically. However, in the practical calculation, these 4 terms do not average to zero because the separation among different time scales cannot be clear-cut. In (10), $-\rho_0 \overline{u_{turb}^2 \frac{\partial (u_{GW}+u_0)}{\partial x}}^{3\text{min}} - \rho_0 \overline{w_{turb}^2 \frac{\partial (w_{GW}+w_0)}{\partial z}}^{3\text{min}}$ represents the KE_{turb} change rate due to GW and BG flow expansion or compression. GW and BG flow expansion or compression result in a redistribution of KE_{turb}. $-\rho_0 \overline{w_{turb} u_{turb}}^{3\text{min}} (\frac{\partial (w_{GW}+w_0)}{\partial x} + \frac{\partial (u_{GW}+u_0)}{\partial z})$ represents the KE_{turb} change rate due to GW and BG wind shear. $-\overline{(\vec{v_{GW}} + \vec{v_0}) \cdot \nabla KE_{turb}}^{3\text{min}}$ depicts the KE_{turb} change rate due to GW and BG wind transport KE_{turb} into or out of the chosen region. $\overline{\frac{\vec{v_{turb}}\rho_{turb}}{\rho_0}}^{3\text{min}} \cdot \nabla (p_{GW} + p_0)$ depicts the KE_{turb} change rate due to GW and BG pressure gradients or buoyancy terms. All the terms discussed above are related to interactions between turbulence and its background. $-\overline{(\vec{v_{turb}}) \cdot \nabla KE_{turb}}^{3\text{min}}$ and $-\overline{\vec{v_{turb}} \cdot \nabla p_{turb}}^{3\text{min}}$ are turbulence self-interactions. Self-interactions of perturbations may both strengthen or weaken the perturbation. These two processes are referred to as "self-strengthening" and "self-weakening," respectively.

GW-turbulence interactions generally result in a decrease in the KE_{turb} during the GW-breaking process. As illustrated in the middle 2 plots in Figure 5, in the left plot, the red solid line depicts the KE_{turb} increased by about 70 J due to redistribution of KE_{turb} by GWs. The blue solid line depicts the KE_{turb} lost approximately 170 J through the interaction of turbulence momentum flux and GW wind shear. The cyan line depicts a loss of about 120 J in KE_{turb} through advection caused by the velocity of GWs. The green solid line shows that the change in KE_{turb} due to the pressure gradient force of the GWs acting on the turbulence velocity is approximately zero. Turbulence loses about 220 J into GWs during the GW-breaking process.

After GWs begin to break, the increase in KE_{turb} is primarily due to BG-turbulence interactions. As shown in the bottom two plots in Figure 5, the left plot depicts the energy change due to different physical processes, while the right plot shows the corresponding energy change rate. The energy changes are obtained by integrating the rates of change over time, while the rates of change are obtained by integrating over a chosen spatial domain. In the left plot, the red solid line indicates that KE_{turb} increased by about 10 J due to the redistribution of KE_{turb} by BG flow. The blue solid line depicts that KE_{turb} lost approximately 110 J through the interaction of turbulence momentum flux and BG wind shear. The cyan line depicts that KE_{turb} continues to gain energy through advection due to BG velocity, resulting in a gain of approximately 100 J. The green solid line shows the KE_{turb} change and change rate through BG pressure gradient force doing work on turbulence velocity. This process decreases the KE_{turb} before GW breaking. However, after GW starts to break, the BG pressure gradient force or the buoyant force increases the KE_{turb} by approximately 300 J.

Self-interactions of turbulence play a crucial role in the variability of KE_{turb}. As shown in the top two plots in Figure 5, KE_{turb} starts to grow rapidly after the 56th minute when GW starts to break. Advection of KE_{turb} by turbulence velocity starts to decrease KE_{turb} around the 60th minute, as depicted by the blue lines. Turbulence pressure gradient along with turbulence velocity causes a decrease in KE_{turb} from the 56th to 65th minute and increases KE_{turb} after the 65th minute, as shown by the cyan lines.

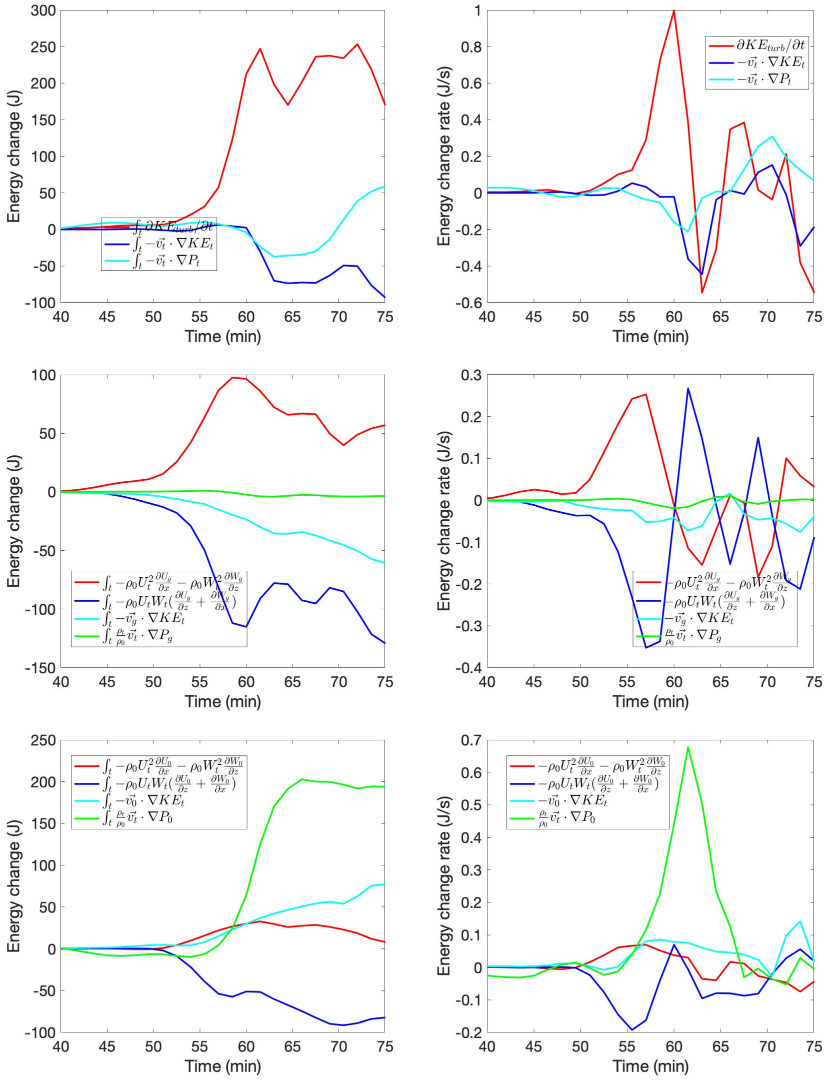

Figure 5: KE_{turb} change and change rate through different physical processes. The energy changes depicted in the left plots are obtained by integrating the energy change rates over time. The energy change rates displayed in the right plots are obtained through the integration of energy change rates over the selected spatial domain.

Gravity Wave KE

KE in perturbations with 20-min BPA BG and KE in turbulence with 3-min BPA BG were deducted in this section. Their difference represents the tendency of KE in GWs. Rewrite (7),

$$
\begin{aligned}
\frac{\partial(KE_{turb}+KE_{GW})}{\partial t} &= -\rho_0(u_{GW}+u_{turb})(u_{GW}+u_{turb})\frac{\partial u_0}{\partial x}\\
&-\rho_0(w_{GW}+w_{turb})(w_{GW}+w_{turb})\frac{\partial w_0}{\partial z}\\
&-\rho_0(w_{GW}+w_{turb})(u_{GW}+u_{turb})(\frac{\partial w_0}{\partial x}+\frac{\partial u_0}{\partial z})\\
&-\vec{v}\cdot\nabla(KE_{turb}+KE_{GW})\\
&+\frac{(\vec{v_{GW}}+\vec{v_{turb}})(\rho_{turb}+\rho_{GW})}{\rho_0}\cdot\nabla p_0-(\vec{v_{GW}}+\vec{v_{turb}})\cdot\nabla(p_{GW}+p_{turb})\\
&+\rho_0(u_{GW}+u_{turb})\overline{(\vec{v_{GW}}+\vec{v_{turb}})\cdot\nabla(u_{GW}+u_{turb})}^{20\mathrm{min}}\\
&+\rho_0(w_{GW}+w_{turb})\overline{(\vec{v_{GW}}+\vec{v_{turb}})\cdot\nabla(w_{GW}+w_{turb})}^{20\mathrm{min}}\\
&-(u_{GW}+u_{turb})\overline{\frac{(\rho_{turb}+\rho_{GW})}{\rho_0}\frac{\partial(p_{GW}+p_{turb})}{\partial x}}^{20\mathrm{min}}\\
&-(w_{GW}+w_{turb})\overline{\frac{(\rho_{turb}+\rho_{GW})}{\rho_0}\frac{\partial(p_{GW}+p_{turb})}{\partial z}}^{20\mathrm{min}},
\end{aligned}
\tag{11}
$$

where the symbol $\overline{Q}^{20\mathrm{min}}$ denotes the 20-minute BPA. Subtract (9) from (11).

$$
\begin{aligned}
\frac{\partial KE_{GW}}{\partial t} &= -\rho_0(u_{GW}^2+2u_{turb}u_{GW})\frac{\partial u_0}{\partial x}+\rho_0 u_{turb}^2\frac{\partial u_{GW}}{\partial x}\\
&-\rho_0(w_{GW}^2+2w_{turb}w_{GW})\frac{\partial w_0}{\partial z}+\rho_0 w_{turb}^2\frac{\partial w_{GW}}{\partial z}\\
&-\rho_0 w_{GW}u_{GW}(\frac{\partial w_0}{\partial x}+\frac{\partial u_0}{\partial z})-\rho_0(w_{turb}u_{GW}+w_{GW}u_{turb})(\frac{\partial w_0}{\partial x}+\frac{\partial u_0}{\partial z})\\
&+\rho_0 w_{turb}u_{turb}(\frac{\partial w_{GW}}{\partial x}+\frac{\partial u_{GW}}{\partial z})-\vec{v}\cdot\nabla KE_{GW}\\
&+\frac{(\vec{v_{GW}}\rho_{GW}+\vec{v_{GW}}\rho_{turb}+\vec{v_{turb}}\rho_{GW})}{\rho_0}\cdot\nabla p_0-\frac{\vec{v_{turb}}\rho_{turb}}{\rho_0}\cdot\nabla p_{GW}\\
&-\vec{v_{GW}}\cdot\nabla p_{GW}-\vec{v_{turb}}\cdot\nabla p_{GW}-\vec{v_{GW}}\cdot\nabla p_{turb}\\
&+\rho_0(u_{GW}+u_{turb})\overline{(\vec{v_{GW}}+\vec{v_{turb}})\cdot\nabla(u_{GW}+u_{turb})}^{20\mathrm{min}}\\
&+\rho_0(w_{GW}+w_{turb})\overline{(\vec{v_{GW}}+\vec{v_{turb}})\cdot\nabla(w_{GW}+w_{turb})}^{20\mathrm{min}}\\
&-(u_{GW}+u_{turb})\overline{\frac{(\rho_{turb}+\rho_{GW})}{\rho_0}\frac{\partial(p_{GW}+p_{turb})}{\partial x}}^{20\mathrm{min}}\\
&-(w_{GW}+w_{turb})\overline{\frac{(\rho_{turb}+\rho_{GW})}{\rho_0}\frac{\partial(p_{GW}+p_{turb})}{\partial z}}^{20\mathrm{min}}\\
&-\rho_0 u_{turb}\overline{\vec{v_{turb}}\cdot\nabla u_{turb}}^{3\mathrm{min}}-\rho_0 w_{turb}\overline{\vec{v_{turb}}\cdot\nabla w_{turb}}^{3\mathrm{min}}\\
&+u_{turb}\overline{\frac{\rho_{turb}}{\rho_0}\frac{\partial p_{turb}}{\partial x}}^{3\mathrm{min}}+w_{turb}\overline{\frac{\rho_{turb}}{\rho_0}\frac{\partial p_{turb}}{\partial z}}^{3\mathrm{min}}.
\end{aligned}
\tag{12}
$$

Averaging the equation over 20-min intervals and removing the linear terms that averaged to zero yields

$$
\begin{aligned}
\frac{\partial \overline{KE_{GW}}^{20\text{min}}}{\partial t} &= -\rho_0 \overline{(u_{GW}^2 + 2u_{turb}u_{GW})}^{20\text{min}} \frac{\partial u_0}{\partial x} + \rho_0 \overline{u_{turb}^2 \frac{\partial u_{GW}}{\partial x}}^{20\text{min}} \\
&\quad -\rho_0 \overline{(w_{GW}^2 + 2w_{turb}w_{GW})}^{20\text{min}} \frac{\partial w_0}{\partial z} + \rho_0 \overline{w_{turb}^2 \frac{\partial w_{GW}}{\partial z}}^{20\text{min}} \\
&\quad -\rho_0 \overline{w_{GW}u_{GW}}^{20\text{min}} \left(\frac{\partial w_0}{\partial x} + \frac{\partial u_0}{\partial z}\right) - \rho_0 \overline{(w_{turb}u_{GW} + w_{GW}u_{turb})}^{20\text{min}} \left(\frac{\partial w_0}{\partial x} + \frac{\partial u_0}{\partial z}\right) \\
&\quad + \overline{\rho_0 w_{turb}u_{turb}\left(\frac{\partial w_{GW}}{\partial x} + \frac{\partial u_{GW}}{\partial z}\right)}^{20\text{min}} - \overline{\vec{v} \cdot \nabla KE_{GW}}^{20\text{min}} \\
&\quad + \frac{\overline{(\vec{v_{GW}}\rho_{GW} + \vec{v_{GW}}\rho_{turb} + \vec{v_{turb}}\rho_{GW})}^{20\text{min}}}{\rho_0} \cdot \nabla p_0 - \overline{\frac{\vec{v_{turb}}\rho_{turb}}{\rho_0} \cdot \nabla p_{GW}}^{20\text{min}} \\
&\quad - \overline{\vec{v_{GW}} \cdot \nabla p_{GW}}^{20\text{min}} - \overline{\vec{v_{turb}} \cdot \nabla p_{GW}}^{20\text{min}} - \overline{\vec{v_{GW}} \cdot \nabla p_{turb}}^{20\text{min}} \\
&\quad - \overline{\rho_0 u_{turb} \overline{\vec{v_{turb}} \cdot \nabla u_{turb}}^{3\text{min}}}^{20\text{min}} - \overline{\rho_0 w_{turb} \overline{\vec{v_{turb}} \cdot \nabla w_{turb}}^{3\text{min}}}^{20\text{min}} \\
&\quad + \overline{u_{turb} \overline{\frac{\rho_{turb}}{\rho_0} \frac{\partial p_{turb}}{\partial x}}^{3\text{min}}}^{20\text{min}} + \overline{w_{turb} \overline{\frac{\rho_{turb}}{\rho_0} \frac{\partial p_{turb}}{\partial z}}^{3\text{min}}}^{20\text{min}} .
\end{aligned}
\tag{13}
$$

The 4 terms in (12) are expected to average to zero when using 20-minute averages, but in the practice, this is not always the case due to the difficulty in clearly distinguishing between different time scales. In (13), $-\rho_0 \overline{u_{GW}^2}^{20\text{min}} \frac{\partial u_0}{\partial x} - \rho_0 \overline{w_{GW}^2}^{20\text{min}} \frac{\partial w_0}{\partial z}$ is the KE_{GW} change rate due to BG flow expansion or compression, also referred to as the redistribution of KE_{GW} by BG. $-\rho_0 \overline{w_{GW}u_{GW}}^{20\text{min}} (\frac{\partial w_0}{\partial x} + \frac{\partial u_0}{\partial z})$ is the KE_{GW} change rate resulting from the interaction of GW momentum flux and BG wind shear. $-\overline{\vec{v_0} \cdot \nabla KE_{GW}}^{20\text{min}}$ is the transportation of KE_{GW} caused by the BG wind. $\frac{\overline{\vec{v_{GW}}\rho_{GW}}^{20\text{min}}}{\rho_0} \cdot \nabla p_0$ depicts the KE_{GW} change rate due to BG pressure gradient or buoyancy term. The terms above are categorized as BG-GW interactions. $-\overline{\vec{v_{GW}} \cdot \nabla KE_{GW}}^{20\text{min}}$ and $-\overline{\vec{v_{GW}} \cdot \nabla p_{GW}}^{20\text{min}}$ depict the effect on KE_{GW} change rate from GW self-interactions. $\rho_0 \overline{u_{turb}^2 \frac{\partial u_{GW}}{\partial x}}^{20\text{min}}$ + $\rho_0 \overline{w_{turb}^2 \frac{\partial w_{GW}}{\partial z}}^{20\text{min}}$ depicts the KE_{GW} change rate due to GW redistributing turbulence. $\overline{\rho_0 w_{turb}u_{turb}(\frac{\partial w_{GW}}{\partial x} + \frac{\partial u_{GW}}{\partial z})}^{20\text{min}}$ represents the KE_{GW} change rate due to interactions of GW wind shear and turbulence momentum flux. $-\overline{\vec{v_{turb}} \cdot \nabla KE_{GW}}^{20\text{min}}$ shows the effects on KE_{GW} change rate due to the averaged effect of turbulence transporting KE_{GW}. $-\overline{\frac{\vec{v_{turb}}\rho_{turb}}{\rho_0} \cdot \nabla p_{GW}}^{20\text{min}}$, $-\overline{\vec{v_{turb}} \cdot \nabla p_{GW}}^{20\text{min}}$ and $-\overline{\vec{v_{GW}} \cdot \nabla p_{turb}}^{20\text{min}}$ depict the KE_{GW} change rate due to buoyancy force of GW and turbulence, acting on turbulence or GW perturbations, respectively. The terms discussed above are grouped as GW-turbulence interactions. The remaining terms in (13) are grouped as BG-GW-turbulence interactions because they involve variables from BG, GWs, and turbulence in their mathematical expressions. These terms reflect the complex interplay related to the three different scales.

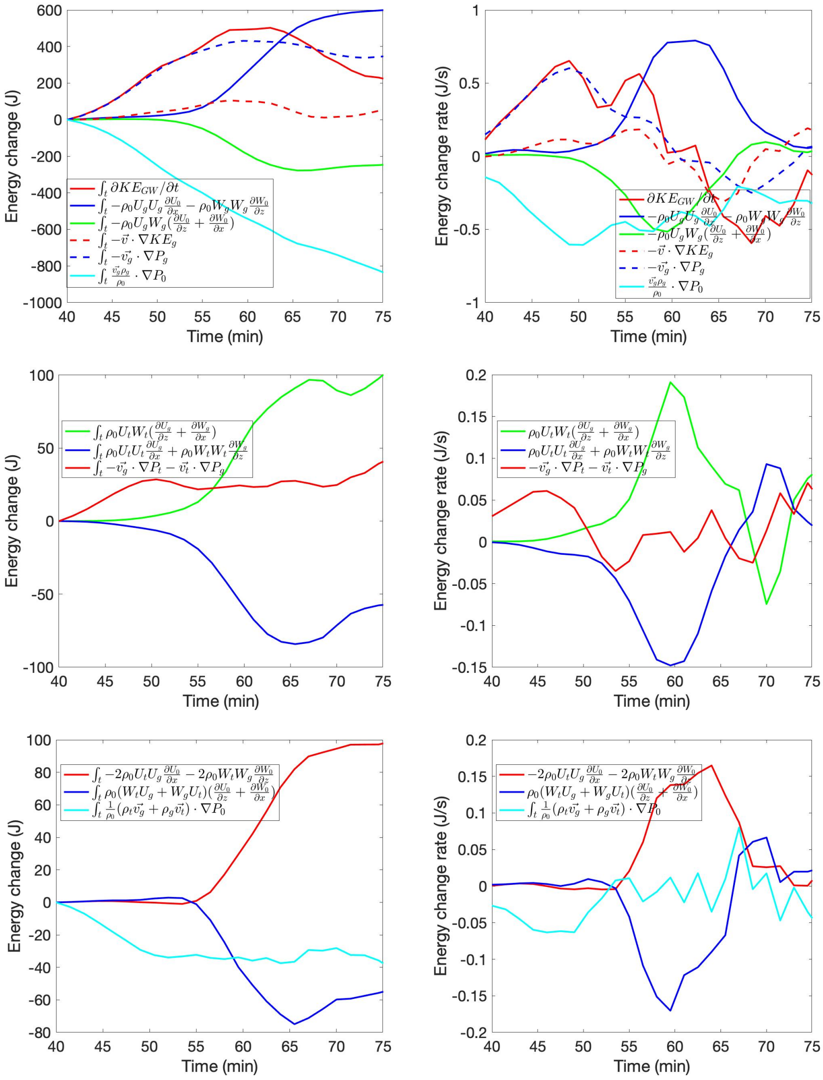

Figure 6: KE_{GW} change and change rate due to GW and BG interactions over the spatial domain. The left plot depicts the energy change due to different physical processes, and the right plot depicts the corresponding energy change rate. The energy changes depicted in the left plots are obtained by integrating the energy change rates over time. The energy change rates displayed in the right plots are obtained through the integration of energy change rates over the selected spatial domain.

Interactions between BG and GWs, such as KE_{GW} advection, redistribution of KE_{GW} by BG, KE_{GW} transportation by BG, GW self-strengthening, and other BG-GW interactions play the dominant role in the evolution of KE_{GW}. The changes in KE_{GW} and the change rates resulting from interactions between BG and GWs are shown in the top 2 plots of Figure 6. The energy changes depicted in the left plots are obtained by integrating the energy change rates over time. The energy change rates displayed in the right plots are obtained through the integration of energy change rates over the selected spatial domain. The red solid line shows that KE_{GW} increases from the start and reaches its maximum value at the 56th minute. After that, gravity wave breaking begins and KE_{GW} decreases. The blue solid lines in the top plots depict the redistribution of KE_{GW} by BG. After the GW starts to break, BG redistributes more energy into the chosen region. The redistribution stopped shortly after turbulence fully developed around the 73rd minute, after which the energy change due to redistribution remains constant. The green solid line in the left top plot represents the energy transfer between GWs and BG through the interaction of GW momentum flux and BG wind shear. The green line is negative, which indicates that GW is losing KE to BG. This mechanism starts to impact the KE_{GW} when GW begins to break. During GW breaks, GW loses about 220 J energy to BG through this interaction. GW advection slightly increased KE_{GW} before GW starts to break, as shown by the red dashed lines in the top two plots. Before GW starts to break, the main increase of KE_{GW} is due to the nonlinear interaction of GW velocity and GW pressure gradient force, as shown by the blue dashed lines in the top two plots. GW self-strengthening contributes to the increase of KE_{GW} before GW breaking. BG pressure gradient power decreases KE_{GW} in the chosen region, as shown by the cyan solid lines in the top two plots, starting before GWs start to break.

The role of turbulence in the alteration of KE_{GW} is significant. Both direct interactions between GWs and turbulence and the interactions between the BG, GWs, and turbulence contribute roughly equally to the rate of change in KE_{GW}. The KE_{GW} changes and change rate due to GW-turbulence interactions are presented in the middle 2 plots in Figure 6. The bottom 2 plots in the same figure display the changes and change rates in KE_{GW} due to BG-GW-turbulence interactions. The energy changes depicted in the left plots are obtained by integrating the energy change rates over time. The energy change rates displayed in the right plots are obtained through the integration of energy change rates over the selected spatial domain.

In general, GW-turbulence interactions increase KE_{GW}, while BG-GW-turbulence interactions decrease KE_{GW}. As shown by the green line in the middle 2 plots in Figure 6, the interaction between the turbulence momentum flux and the GW wind shear results in an increase in the GW wind shear, leading to a rise in KE_{GW} after the GW breaks. This is comparable to the process in which the GW momentum flux transfers its KE GW into the BG wind shear, as illustrated by the green line in the top two plots in Figure 6. Before GWs break, GW KE increases through turbulence pressure gradient force doing work shown by the red solid line in the middle 2 plots in Figure 6. BG expansion or compression interacts with GW and turbulence momentum flux increase the KE_{GW} during the turbulence developing process shown by the red solid line in the bottom 2 plots in Figure 6. The blue solid lines in the middle 2 plots depict that BG wind shear interacts with GW and turbulence momentum flux decrease the KE_{GW} during the 5-minute interval of the turbulence developing process.

BG-GW-turbulence interactions generally decreases KE_{GW}. Before turbulence develops, the three component interactions decrease KE_{GW}, transferring energy into BG. GW energy loses to BG. After GW starts to break, GW energy is transferred into turbulence and BG. About 230J KE is transferred from turbulence into GW at the end from KE_{turb} tendency as shown in the left middle plot in Figure 5. About 220J energy is transferred from turbulence into GW as shown in Figure 6. So most of the energy transferred by BG-GW-turbulence interactions finally goes into BG.

5.2.3 GW and Turbulence KE Tendencies During Turbulence Development

A closer examination of the period between the 56th and 65th minutes, when the gravity wave breaks and turbulence develops, is insightful. 2-s resolution KE_{turb} and KE_{GW} change and change rate are presented between the 56th minute and 65th minute when the GWs start to break and turbulence starts to develop. The energy changes due to various physical processes are presented in Figure 7. It is not necessary to display the 2-second resolution energy change and energy change rate of KE_0 as it only relates to low-frequency (period $\geq$ 20 minutes) variables or the 20-minute averaged effect of high-frequency perturbations (turbulence and GWs, period $<$ 20 minutes).

From the 50th to the 58th minute, the growth rate of KE_{turb} is relatively slow, as depicted by the solid red lines in the top two plots of Figure 7. During this 8-min inter-

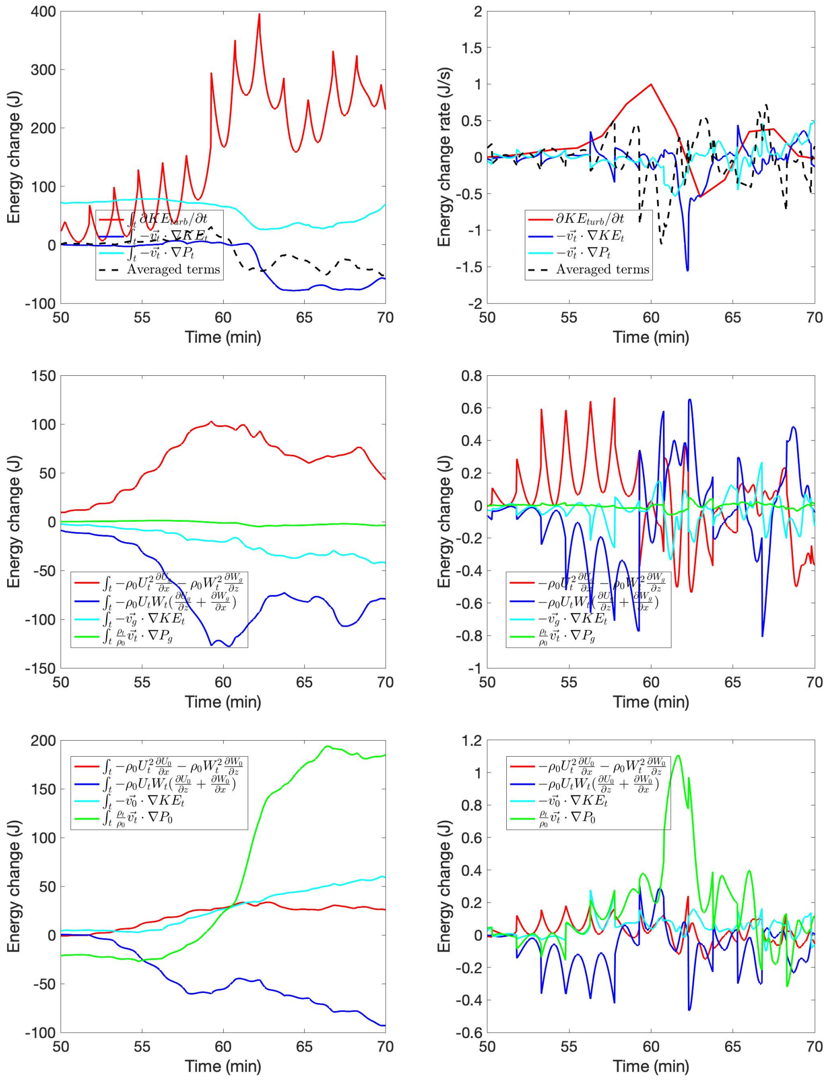

Figure 7: KE_{turb} change and change rate between the 50th minute and 70the minute. The left plot depicts the energy change due to different physical processes, and the right plot depicts the corresponding energy change rate. The energy changes depicted in the left plots are obtained by integrating the energy change rates over time. The energy change rates displayed in the right plots are obtained through the integration of energy change rates over the selected spatial domain.

val, the main factor contributing to the growth of KE_{turb} is the redistribution by gravity waves, as shown in the plot on the middle right. This 8-min interval is referred to as turbulence growth phase 1. The maximum value of turbulence KE_{turb} is reached 5 minutes after the 58th minute. This 5-minute period is referred to as turbulence growth phase 2. Before GWs break, the interaction of turbulence momentum flux and wind shear decreases KE_{turb}, as shown by the blue solid lines in the middle two plots of Figure 7. However, the GW redistribution increases KE_{turb}, as depicted by the red solid line in the same two plots. The combined effect from GW-turbulence interaction increases KE_{turb} before GWs break. After the breaking of GWs, turbulence starts to grow rapidly. However, the combined effect of GW-turbulence interaction decreases KE_{turb}. Turbulence mainly absorbs KE through BG-turbulence interactions, especially in the last 2 minutes when turbulence is at its strongest, as indicated by the green solid line in the bottom two plots in Figure 7. The primary driver of the BG-turbulence interactions that drive turbulence growth is the BG buoyant force acting on turbulence velocity.

5.3 Instabilities and GW-breaking

During the GW breaking period, instabilities play a significant role in the generation of turbulence. Instabilities are closely associated with GW breaking and the generation of turbulence. At the 46th minute, instabilities begin to emerge in the chosen region, as shown in Figure 8. Probabilities of instabilities reach their maximum at around the 70th minute.

PCI is closely linked to the GW breaking process. Between the 54th minute and 58th minute, both PCI and PDI rise along with KE_{GW} increases. However, between the 58th minute and 62nd minute, PCI drops approximately 8 percentage points along with the growth of KE_{turb}. Subsequently, from the 62nd to the 64th minute, as the KE_{turb} decreases by 150 J, as shown in the top left plot in Figure 7, the PCI increases by approximately 8 percentage points. Instabilities can result from large temperature gradients and wind shear introduced by GWs.

6 Discussion

The mechanisms of energy convergence during various stages of gravity wave breaking are distinct. Before the turbulence growth phase 2 and prior to the saturation of GWs

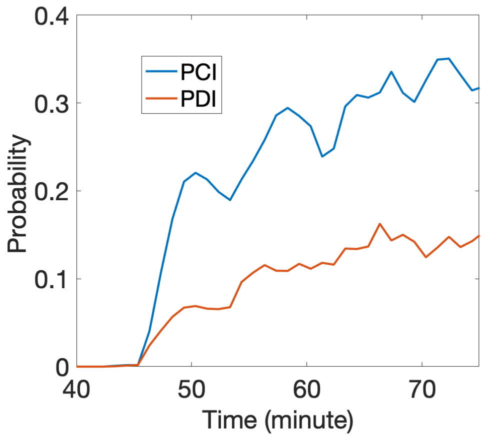

Figure 8: PCI and PDI in the chosen region. The blue lines depict the probability of convective instability. The red lines depict the probability of dynamic instability.

(around the 58th minute), the work done by the gravity force on vertical motion and the convergence of pressure flux due to flow expansion/compression balance each other, as demonstrated in the top two plots in Figure 3. On average, the work done by pressure is the dominant factor in the convergence of pressure flux before GW breaking begins, as indicated by the magenta solid line in the top left plot of Figure 3. The IE-KE conversion is through flow oscillations along with expansion/compression. The blue and red dashed lines in the top right plot of Figure 3 demonstrate that the magnitude of energy conversion from KE to IE is comparable to that from PE to KE, but with opposite signs. However, the converted IE is almost zero during the first 58 minutes. Prior to the breaking or dissipation of GWs, the energy conversion in the flow is an adiabatic process, and on average over the BG period, there is no conversion between mechanical energy and IE. During turbulence growth phase 2 and GW saturation interval (between the 58th and 62nd minute), KE_{GW} stays constant while KE_{turb} increases to its maximum. KE starts to be converted to PE, as indicated by the blue dashed line in the right top plot in Figure 3. Meanwhile, more IE starts to be converted to KE, as shown by the red dashed line in the right top plot in Figure 3. A possible dynamic is that as GW is about to break, the flow keeps expanding when the GW propagates upward, which increases the KE and maintains momentum conservation.

The relationship between wave energy deposition and turbulent dissipation has been suggested in previous studies [*Becker and Schmitz*, 2002]. In our simulation, before the onset of turbulence, there is limited energy deposition occurs, not only in the case of conservative wave propagation [*Becker and Schmitz*, 2002] but also before turbulence-growth phase 2 when turbulence interacts with BG. After phase 2, KE is converted into IE. This conversion is primarily driven by the pressure flux, which is in agreement with the findings of *Becker and Schmitz* [2002]. Turbulence starts to decay after the KE_{turb} reaches its maximum. Approximately 5 minutes after the KE_{turb} peak (at the 69th minute), KE starts to be converted to IE, as shown by the red dashed line in the right top plot in Figure 3. This suggests that the decay of turbulence is related to the pressure flux $p\nabla \cdot \vec{v}$ and KE-IE conversion. This study indicates that heat transport due to wave propagation is the main cause of IE variation prior to gravity wave breaking or saturation in the mesopause region. IE change due to KE-IE convergence becomes the dominant factor when GW starts to break especially after wave-breaking-generated turbulence starts to decay.

The interactions between GWs and turbulence, between BG and GWs, and between BG and turbulence have distinct functions during the two phases of turbulence growth. The energy transferred through these interactions is summarized in the energy-transfer triangle shown in Figure 9. The blue arrows indicate the direction of energy transferred through related interactions during turbulence growth phase 1. The red arrows indicate the direction of energy transferred during turbulence growth phase 2. The size of the arrows represents the energy transfer magnitude. In this system, GWs are the source of KE. In the two phases of turbulence growth, GWs transferred 570 J of energy to BG through BG-GW interactions, with the majority of energy transfer occurring in phase 1.

The convergence of energy resulting from gravity wave saturation is linked to turbulence. Gravity wave saturation primarily occurs through instabilities that act locally to dissipate wave energy and produce turbulence. GW saturation results in net deceleration of the zonal mean flow and turbulent heating of the environment [*Fritts*, 1989]. Figure 9 suggests that the processes are possibly related to turbulence. Saturated GW transfers GW KE to BG flow, but more energy is transferred from BG to turbulence, most of which is converted into BG IE through turbulent heating.

As GWs propagate, they continuously interact with the BG flow and alter it. Simulations by *Bölöni et al.* [2016] suggest that direct BG-GW interactions dominate energy transfer over the wave-breaking. Our simulation shows consistent results in both phases of turbulence development, as demonstrated in Figure 6. Before turbulence-growth phase

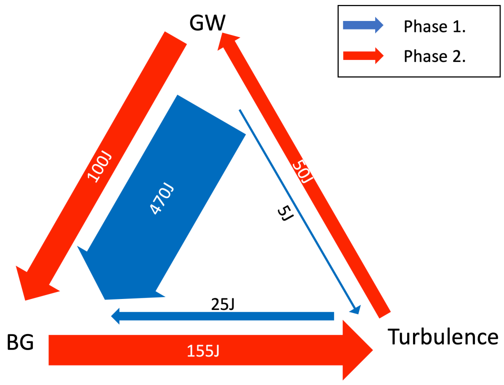

Figure 9: A schematic diagram of KE transfer between BG, GW, and turbulence. The blue arrows show the energy flow direction and amount during turbulence growth phase 1. The red arrows show the energy flow direction and amount during turbulence growth phase 2. The thicknesses of the arrows represent the amount of energy transferred within the time intervals of phases 1 or 2.

2, the KE transferred by direct BG-GW interactions is about 430 J and KE transferred related to the turbulence act is approximately 40 J. During phase 2, with the situation that the magnitude of turbulent perturbation grows rapidly, direct BG-GW interaction transfers 100 J KE to mean flow, while the turbulence transfers 50 J back to GW, as indicated by the red arrows in Figure 9.

GW-turbulence interactions initiated the initial development of turbulence. During phase 1, turbulence grows through both GW-turbulence interactions and self-strengthening. The transfer of energy between GWs and turbulence is solely achieved through the work done by the wave fluctuations in turbulent stress against the wave rates of strain [*Finnigan*, 1988; *Einaudi and Finnigan*, 1993; *Finnigan and Shaw*, 2008]. Our simulation confirms these results, showing that the transfer of KE between GWs and turbulence during the GW breaking process is solely achieved through the mechanism $U_t W_t \frac{\partial U_{g_i}}{\partial x_j}$. In this study, we also take into account the redistribution of KE_{turb} by GWs as part of the GW-turbulence interactions, even though no energy is directly transferred between the GWs and turbulence through this mechanism.

Our simulation reveals that the BG-turbulence interactions, particularly the buoyancy term, are the leading contributor to turbulence growth in phase 2, demonstrated by the green solid lines in the bottom plots of Figure 7. In the observation by *de Nijs and*

Pietrzak [2012], they found that buoyancy production dominates in some instants. The influence of buoyancy is typically taken into account as a sink of KE_{turb} but when buoyancy is negative, which is associated with unstable stratification, the buoyancy can convert turbulent potential energy into KE_{turb}. Therefore, buoyancy can cause an increase in KE_{turb}. Extra study about total turbulent energy and turbulent potential energy is necessary to examine this mechanism.

Convective instability is the first step leading to wave breaking and turbulence generation [*Koudella and Staquet*, 2006]. In the chosen domain, instabilities occur 10 minutes before GWs start to break. GW breaking generates turbulence which reduces instabilities through turbulence momentum flux absorbing energy from BG wind shear. This simulation provides support for the mechanisms proposed in *Fritts and Dunkerton* [1985].

This 2D simulation provided valuable insight into the dynamics of gravity wave breaking. However, as suggested by *Fritts et al.* [1994, 2022b,c] and *Andreassen et al.* [1994], 2D computations may not accurately capture the instability structure and turbulence generation associated with wave breaking. Additionally, this study focuses on turbulence kinetic energy (KE_{turb}) and does not account for conversions between KE_{turb} and turbulence potential energy. Further research in this area is necessary.

7 Conclusion

Energy conversions between KE, PE, and IE over the chosen region, are investigated. Throughout the simulation, kinetic energy in the mesopause region increased. Potential energy is converted to kinetic energy, and most of the increased kinetic energy is converted to internal energy. The energy conversion shows different patterns of dominance during the two intervals. Specifically, during the GW breaking process, the period of turbulence growth is divided into two distinct phases based on KE_{turb} change rate. Before phase 2, the dominant total energy change in the chosen region is caused by PE-KE conversion and KE transportation. After phase 1, the dominant total energy change in the chosen region results from PE-KE conversion and KE-IE conversion. The primary mechanism for KE-IE conversion is through pressure flux, which is associated with the decay of turbulence.

The kinetic energy transfer among the turbulence, GW, and background is studied. Energy transfers among these three components are bilateral. At different stages, the combined effects show different energy-transferring directions. The interactions between the BG and GWs dominate the energy transfer process during the GW-breaking event. On the other hand, GW-turbulence interactions initiated the growth of turbulence. However, in the second phase, the GW-turbulence interactions feed back energy from turbulence to the GWs. The only mechanism of energy transfer between GWs and turbulence through GW-turbulence interactions is the turbulent stress against the wave rates of strain. BG-turbulence interactions are the dominant contributor to the growth of turbulence, especially in the second phase, and the dominant contributor in BG-turbulence interaction is the work by buoyancy. However, buoyancy reduces KE_{GW} over the simulation.

Instabilities lead to the breaking of GWs. The breaking of GWs generates turbulence, which in turn weakens instabilities by dissipating wave energy. The BG acts as an intermediary in the process of turbulence dissipating wave energy.

DNS modeling studies are valuable in explaining small structure dynamics. Increasingly realistic DNS modeling can yield an improved ability to quantify the contributions to turbulence development through different mechanisms. More studies such as 3D simulations are necessary to improve our understanding of the GW breaking process.

8 Acknowledgement

This research was supported by National Science Foundation (NSF) grant AGS-1759471. The work by Alan Liu is supported by (while serving at) the NSF.

A: Energy Conversion

This appendix is to present the deduction for energy conservation among kinetic energy (KE), internal energy (IE), and potential energy (PE).

Start with CGCAM governing equations.

$$\frac{\partial \rho}{\partial t} + \frac{\partial(\rho u)}{\partial x} + \frac{\partial(\rho w)}{\partial z} = 0; \tag{A.1}$$

$$\frac{\partial(\rho u)}{\partial t} + \frac{\partial(\rho uu)}{\partial x} + \frac{\partial(\rho uw)}{\partial z} = -\frac{\partial p}{\partial x} + (\frac{\partial \sigma_{xx}}{\partial x} + \frac{\partial \sigma_{xz}}{\partial z}); \tag{A.2}$$

$$\frac{\partial(\rho w)}{\partial t} + \frac{\partial(\rho wu)}{\partial x} + \frac{\partial(\rho ww)}{\partial z} = -\frac{\partial p}{\partial z} - \rho g + (\frac{\partial \sigma_{xz}}{\partial x} + \frac{\partial \sigma_{zz}}{\partial z}). \tag{A.3}$$

(A.2) and (A.3) can be rewritten as

$$\rho\frac{\partial u}{\partial t} + \rho u\frac{\partial u}{\partial x} + \rho w\frac{\partial u}{\partial z} + u(\frac{\partial \rho}{\partial t} + \frac{\partial(\rho u)}{\partial x} + \frac{\partial(\rho w)}{\partial z}) = -\frac{\partial p}{\partial x} + (\frac{\partial \sigma_{xx}}{\partial x} + \frac{\partial \sigma_{xz}}{\partial z}); \tag{A.4}$$

$$\rho\frac{\partial w}{\partial t} + \rho u\frac{\partial w}{\partial x} + \rho w\frac{\partial w}{\partial z} + w(\frac{\partial \rho}{\partial t} + \frac{\partial(\rho u)}{\partial x} + \frac{\partial(\rho w)}{\partial z}) = -\frac{\partial p}{\partial z} - \rho g + (\frac{\partial \sigma_{xz}}{\partial x} + \frac{\partial \sigma_{zz}}{\partial z}). \tag{A.5}$$

Substitute (A.1) into the left hand side of equations above. The equations can be rewritten as follow after every term is divided by ρ. The equations describe the tendencies of momentum and energy per unit mass.

$$\frac{\partial u}{\partial t} + u\frac{\partial u}{\partial x} + w\frac{\partial u}{\partial z} = -\frac{1}{\rho}\frac{\partial p}{\partial x} + \frac{1}{\rho}\left(\frac{\partial \sigma_{xx}}{\partial x} + \frac{\partial \sigma_{xz}}{\partial z}\right), \tag{A.6}$$

$$\frac{\partial w}{\partial t} + u\frac{\partial w}{\partial x} + w\frac{\partial w}{\partial z} = -\frac{1}{\rho}\frac{\partial p}{\partial z} - g + \frac{1}{\rho}\left(\frac{\partial \sigma_{xz}}{\partial x} + \frac{\partial \sigma_{zz}}{\partial z}\right), \tag{A.7}$$

where

$$\sigma_{xx} = \mu\left(\frac{4}{3}\frac{\partial u}{\partial x} - \frac{2}{3}\frac{\partial w}{\partial z}\right), \tag{A.8}$$

$$\sigma_{zz} = \mu\left(\frac{4}{3}\frac{\partial w}{\partial z} - \frac{2}{3}\frac{\partial u}{\partial x}\right), \tag{A.9}$$

$$\sigma_{xz} = \mu\left(\frac{\partial w}{\partial x} + \frac{\partial u}{\partial z}\right), \tag{A.10}$$

where dynamical viscosity $\mu = 1.57\times10^{-5}$ (N m^{-3} kg). Substituting $\sigma_{xx}, \sigma_{zz}, \sigma_{xz}$ into (A.6) and (A.7) yields:

$$\frac{\partial u}{\partial t} + u\frac{\partial u}{\partial x} + w\frac{\partial u}{\partial z} = -\frac{1}{\rho}\frac{\partial p}{\partial x} + \mu\left(\frac{1}{\rho_0} - \frac{\rho_1}{\rho_0^2}\right)\left(\frac{4}{3}\frac{\partial^2 u}{\partial x^2} + \frac{1}{3}\frac{\partial^2 w}{\partial x \partial z} + \frac{\partial^2 u}{\partial z^2}\right), \tag{A.11}$$

$$\frac{\partial w}{\partial t} + u\frac{\partial w}{\partial x} + w\frac{\partial w}{\partial z} = -\frac{1}{\rho}\frac{\partial p}{\partial z} - g + \mu\left(\frac{1}{\rho_0} - \frac{\rho_1}{\rho_0^2}\right)\left(\frac{4}{3}\frac{\partial^2 w}{\partial z^2} + \frac{1}{3}\frac{\partial^2 u}{\partial x \partial z} + \frac{\partial^2 w}{\partial x^2}\right). \tag{A.12}$$

Part of the horizontal and vertical components of the kinetic energy tendency can be derived by multiplying ρu and ρw on (A.11) and (A.12), respectively.

$$\rho u\frac{\partial u}{\partial t}+\rho u^2\frac{\partial u}{\partial x}+\rho wu\frac{\partial u}{\partial z}=-u\frac{\partial p}{\partial x}+u\mu\left(\frac{4}{3}\frac{\partial^2 u}{\partial x^2}+\frac{1}{3}\frac{\partial^2 w}{\partial x\partial z}+\frac{\partial^2 u}{\partial z^2}\right), \tag{A.13}$$

$$\rho w\frac{\partial w}{\partial t}+\rho uw\frac{\partial w}{\partial x}+\rho w^2\frac{\partial w}{\partial z}=-w\frac{\partial p}{\partial z}-\rho wg+w\mu\left(\frac{4}{3}\frac{\partial^2 w}{\partial z^2}+\frac{1}{3}\frac{\partial^2 u}{\partial x\partial z}+\frac{\partial^2 w}{\partial x^2}\right). \tag{A.14}$$

The equations above missed the part of kinetic energy tendency due to density variation. Multiplying u^2 or w^2 with mass conservation (A.1) leads to the KE tendency due to density tendency:

$$u^2\frac{\partial\rho}{\partial t}+u^3\frac{\partial\rho}{\partial x}+u^2w\frac{\partial\rho}{\partial z}+\rho u^2\frac{\partial u}{\partial x}+\rho u^2\frac{\partial w}{\partial z}=0, \tag{A.15}$$

$$w^2\frac{\partial\rho}{\partial t}+w^2u\frac{\partial\rho}{\partial x}+w^3\frac{\partial\rho}{\partial z}+\rho w^2\frac{\partial u}{\partial x}+\rho w^2\frac{\partial w}{\partial z}=0. \tag{A.16}$$

Combining equations(A.13) and (A.15) together leads to the total tendency of the horizontal part of KE as (A.17). Combining equations(A.14) and (A.16) together gives the total vertical and the horizontal part of KE as (A.18). In the simulation, the diffusivity is negligible, so the diffusion terms are dropped in the KE tendency equations. The deduction of diffusion terms is in appendix 1.

$$\frac{\partial(\frac{1}{2}\rho u^2)}{\partial t}+\frac{1}{2}u^3\frac{\partial\rho}{\partial x}+\frac{1}{2}u^2w\frac{\partial\rho}{\partial z}+\frac{1}{2}\rho u^2\frac{\partial u}{\partial x}+\frac{1}{2}\rho u^2\frac{\partial w}{\partial z}+\rho u^2\frac{\partial u}{\partial x}+\rho uw\frac{\partial u}{\partial z}=-u\frac{\partial p}{\partial x}, \tag{A.17}$$

$$\frac{\partial(\frac{1}{2}\rho w^2)}{\partial t}+\frac{1}{2}w^2u\frac{\partial\rho}{\partial x}+\frac{1}{2}w^3\frac{\partial\rho}{\partial z}+\frac{1}{2}\rho w^2\frac{\partial u}{\partial x}+\frac{1}{2}\rho w^2\frac{\partial w}{\partial z}+\rho wu\frac{\partial w}{\partial x}+\rho w^2\frac{\partial w}{\partial z}=-w\frac{\partial p}{\partial z}-g\rho w. \tag{A.18}$$

Combining the 2 parts leads to the KE tendency.

$$\begin{aligned}\frac{\partial KE}{\partial t}&=-\nabla\cdot(KE\vec{v})-\vec{v}\cdot\nabla p-g\rho w\\&=-\nabla\cdot(KE\vec{v})-\nabla\cdot(p\vec{v})+p\nabla\cdot\vec{v}-g\rho w.\end{aligned} \tag{A.19}$$

The other part of the energy is the internal energy per unit mass (IE).

$$\mathrm{C_v}\frac{dT}{dt}-\frac{1}{\rho}\frac{dp}{dt}=\frac{\kappa}{\rho}\nabla^2T+\frac{dq}{dt}, \tag{A.20}$$

where κ is the conductivity, and κ is not a constant.

$$\kappa=dif*suth. \tag{A.21}$$

where diffusivity $dif = \mu \mathrm{C_p}/Pr$, where Prandtl number $Pr = 1$. $suth$ is Sutherland's formula:

$$suth = \frac{(T_0 + T_{suth})}{(T + T_{suth})}\left(\frac{T}{T_0}\right)^{3/2}, \tag{A.22}$$

where $T_{suth} = 110\,\mathrm{K}$. T_0 is the given background temperature in CGCAM at the initial time, which is 300 K. And dq/dt is zero since there is no heat input or output. So

$$\begin{aligned} \kappa &= \mu \frac{\mathrm{C_p}}{Pr}\frac{(T_0 + T_{suth})}{(T + T_{suth})}\left(\frac{T}{T_0}\right)^{3/2} \\ \kappa &= \mu \frac{\mathrm{C_p}}{Pr}\frac{410}{(T + 110)}\left(\frac{T}{300}\right)^{3/2}. \end{aligned} \tag{A.23}$$

$$\mathrm{C_v}\frac{dT}{dt} = \frac{1}{\rho}\frac{dp}{dt} + \frac{\kappa}{\rho}\nabla^2 T. \tag{A.24}$$

With ideal gas law,

$$\mathrm{C_v}\frac{dT}{dt} = RT\frac{dln\rho}{dt} + \frac{\kappa}{\rho}\nabla^2 T. \tag{A.25}$$

With the continuity equation,

$$\begin{aligned} \mathrm{C_v}\frac{dT}{dt} &= -RT\nabla\cdot\vec{v} + \frac{\kappa}{\rho}\nabla^2 T \\ \frac{\partial T}{\partial t} &= -\frac{1}{\mathrm{C_v}}RT\nabla\cdot\vec{v} - \vec{v}\cdot\nabla T + \frac{\kappa}{\mathrm{C_v}\rho}\nabla^2 T \\ &= -\frac{1}{\rho \mathrm{C_v}}p\nabla\cdot\vec{v} - \vec{v}\cdot\nabla T + \frac{\kappa}{\mathrm{C_v}\rho}\nabla^2 T. \end{aligned} \tag{A.26}$$

$\mathrm{C_v}\rho\times$ (A.26) + $\mathrm{C_v}T\times$ (A.1),

$$\begin{aligned} \frac{\partial IE}{\partial t} &= -\mathrm{C_v}T(\vec{v}\cdot\nabla\rho + \rho\nabla\cdot\vec{v}) - p\nabla\cdot\vec{v} - \mathrm{C_v}\rho\vec{v}\cdot\nabla T + \kappa\nabla^2 T \\ &= -\nabla\cdot(IE\vec{v}) - p\nabla\cdot\vec{v}. \end{aligned} \tag{A.27}$$

Another energy format is potential energy (PE). Potential energy PE = $\rho g h$. The tendency of PE is

$$\begin{aligned} \frac{\partial pE}{\partial t} = gh\frac{\partial\rho}{\partial t} + g\rho w &= -gh(\vec{v}\cdot\nabla\rho + \rho\nabla\cdot\vec{v}) + g\rho w \\ &= -\nabla\cdot(PE\vec{v}) + g\rho w. \end{aligned} \tag{A.28}$$

B: Energy Transfer among Background and Perturbations

The variables are separated into the background part and the perturbation part. Define variable $q = q_0 + q_1$, and $q_0 = q_0(x,z), q_1 = q_1(t,x,z)$. Rewrite (A.11), (A.12), (A.13) and (A.14) as:

$$\begin{aligned}
&\frac{\partial u_0}{\partial t}+\frac{\partial u_1}{\partial t}+\vec{v_0}\cdot\nabla u_0+\vec{v_1}\cdot\nabla u_0+\vec{v_0}\cdot\nabla u_1+\vec{v_1}\cdot\nabla u_1\\
&=-\frac{1}{\rho_0}\frac{\partial p_0}{\partial x}-\frac{1}{\rho_0}\frac{\partial p_1}{\partial x}+\frac{\rho_1}{\rho_0^2}\frac{\partial p_0}{\partial x}+\frac{\rho_1}{\rho_0^2}\frac{\partial p_1}{\partial x}\\
&+\mu(\frac{1}{\rho_0}-\frac{\rho_1}{\rho_0^2})\left(\frac{4}{3}\frac{\partial^2 u_0}{\partial x^2}+\frac{1}{3}\frac{\partial^2 w_0}{\partial x\partial z}+\frac{\partial^2 u_0}{\partial z^2}+\frac{4}{3}\frac{\partial^2 u_1}{\partial x^2}+\frac{1}{3}\frac{\partial^2 w_1}{\partial x\partial z}+\frac{\partial^2 u_1}{\partial z^2}\right),
\end{aligned}\tag{B.1}$$

$$\begin{aligned}
&\frac{\partial w_0}{\partial t}+\frac{\partial w_1}{\partial t}+\vec{v_0}\cdot\nabla w_0+\vec{v_1}\cdot\nabla w_0+\vec{v_0}\cdot\nabla w_1+\vec{v_1}\cdot\nabla w_1\\
&=-\frac{1}{\rho_0}\frac{\partial p_0}{\partial z}-\frac{1}{\rho_0}\frac{\partial p_1}{\partial z}+\frac{\rho_1}{\rho_0^2}\frac{\partial p_0}{\partial z}+\frac{\rho_1}{\rho_0^2}\frac{\partial p_1}{\partial z}-g\\
&+\mu(\frac{1}{\rho_0}-\frac{\rho_1}{\rho_0^2})\left(\frac{4}{3}\frac{\partial^2 w_0}{\partial z^2}+\frac{1}{3}\frac{\partial^2 u_0}{\partial x\partial z}+\frac{\partial^2 w_0}{\partial x^2}+\frac{4}{3}\frac{\partial^2 w_1}{\partial z^2}+\frac{1}{3}\frac{\partial^2 u_1}{\partial x\partial z}+\frac{\partial^2 w_1}{\partial x^2}\right),
\end{aligned}\tag{B.2}$$

where Taylor expansion $\frac{1}{\rho_0+\rho_1}=\frac{1}{\rho_0}-\frac{\rho_1}{\rho_0^2}+\frac{2\rho_1^2}{\rho_0^3}+O(\rho^2)$ is used. Do a time average over one period. For the ideally theoretical case, the averaged q_0 over one period stays the same and the linear terms would vanish. Do a time average on (B.1) and (B.2). The tendency for averaged variables q_0 can be derived.

$$\begin{aligned}
&\frac{\partial u_0}{\partial t}+\vec{v_0}\cdot\nabla u_0+\overline{\vec{v_1}\cdot\nabla u_1}\\
&=-\frac{1}{\rho_0}\frac{\partial p_0}{\partial x}+\overline{\frac{\rho_1}{\rho_0^2}\frac{\partial p_1}{\partial x}}\\
&+\mu\frac{1}{\rho_0}\left(\frac{4}{3}\frac{\partial^2 u_0}{\partial x^2}+\frac{1}{3}\frac{\partial^2 w_0}{\partial x\partial z}+\frac{\partial^2 u_0}{\partial z^2}\right)-\mu\frac{1}{\rho_0^2}\left(\frac{4}{3}\overline{\rho_1\frac{\partial^2 u_1}{\partial x^2}}+\frac{1}{3}\overline{\rho_1\frac{\partial^2 w_1}{\partial x\partial z}}+\overline{\frac{\rho_1\partial^2 u_1}{\partial z^2}}\right),
\end{aligned}\tag{B.3}$$

$$\begin{aligned}
&\frac{\partial w_0}{\partial t}+\vec{v_0}\cdot\nabla w_0+\overline{\vec{v_1}\cdot\nabla w_1}\\
&=-\frac{1}{\rho_0}\frac{\partial p_0}{\partial z}+\overline{\frac{\rho_1}{\rho_0^2}\frac{\partial p_1}{\partial z}}-g\\
&+\mu\frac{1}{\rho_0}\left(\frac{4}{3}\frac{\partial^2 w_0}{\partial z^2}+\frac{1}{3}\frac{\partial^2 u_0}{\partial x\partial z}+\frac{\partial^2 w_0}{\partial x^2}\right)-\mu\frac{1}{\rho_0^2}\left(\frac{4}{3}\overline{\rho_1\frac{\partial^2 w_1}{\partial z^2}}+\frac{1}{3}\overline{\rho_1\frac{\partial^2 u_1}{\partial x\partial z}}+\overline{\rho_1\frac{\partial^2 w_1}{\partial x^2}}\right).
\end{aligned}\tag{B.4}$$

Derive momentum equations for perturbations or GWs by subtracting the BG-period-averaged equations from (B.1) and (B.2).

$$\begin{aligned}
&\frac{\partial u_1}{\partial t}+\vec{v_1}\cdot\nabla u_0+\vec{v_0}\cdot\nabla u_1+\vec{v_1}\cdot\nabla u_1-\overline{\vec{v_1}\cdot\nabla u_1}\\
&=-\frac{1}{\rho_0}\frac{\partial p_1}{\partial x}+\frac{\rho_1}{\rho_0^2}\frac{\partial p_0}{\partial x}+\frac{\rho_1}{\rho_0^2}\frac{\partial p_1}{\partial x}-\overline{\frac{\rho_1}{\rho_0^2}\frac{\partial p_1}{\partial x}}\\
&+\mu\frac{1}{\rho_0}\left(\frac{4}{3}\frac{\partial^2 u_1}{\partial x^2}+\frac{1}{3}\frac{\partial^2 w_1}{\partial x\partial z}+\frac{\partial^2 u_1}{\partial z^2}\right)\\
&-\mu\frac{\rho_1}{\rho_0^2}\left(\frac{4}{3}\frac{\partial^2 u_0}{\partial x^2}+\frac{1}{3}\frac{\partial^2 w_0}{\partial x\partial z}+\frac{\partial^2 u_0}{\partial z^2}+\frac{4}{3}\frac{\partial^2 u_1}{\partial x^2}+\frac{1}{3}\frac{\partial^2 w_1}{\partial x\partial z}+\frac{\partial^2 u_1}{\partial z^2}\right)\\
&+\mu\frac{1}{\rho_0^2}\left(\frac{4}{3}\overline{\rho_1\frac{\partial^2 u_1}{\partial x^2}}+\frac{1}{3}\overline{\rho_1\frac{\partial^2 w_1}{\partial x\partial z}}+\overline{\frac{\rho_1\partial^2 u_1}{\partial z^2}}\right),
\end{aligned}\tag{B.5}$$

$$\begin{aligned}
&\frac{\partial w_1}{\partial t} + \vec{v_1}\cdot\nabla w_0 + \vec{v_0}\cdot\nabla w_1 + \vec{v_1}\cdot\nabla w_1 - \overline{\vec{v_1}\cdot\nabla w_1} \\
&= -\frac{1}{\rho_0}\frac{\partial p_1}{\partial z} + \frac{\rho_1}{\rho_0^2}\frac{\partial p_0}{\partial z} + \frac{\rho_1}{\rho_0^2}\frac{\partial p_1}{\partial z} - \overline{\frac{\rho_1}{\rho_0^2}\frac{\partial p_1}{\partial z}} \\
&+\mu\frac{1}{\rho_0}\left(\frac{4}{3}\frac{\partial^2 w_1}{\partial z^2} + \frac{1}{3}\frac{\partial^2 u_1}{\partial x\partial z} + \frac{\partial^2 w_1}{\partial x^2}\right) \\
&-\mu(\frac{\rho_1}{\rho_0^2})\left(\frac{4}{3}\frac{\partial^2 w_0}{\partial z^2} + \frac{1}{3}\frac{\partial^2 u_0}{\partial x\partial z} + \frac{\partial^2 w_0}{\partial x^2} + \frac{4}{3}\frac{\partial^2 w_1}{\partial z^2} + \frac{1}{3}\frac{\partial^2 u_1}{\partial x\partial z} + \frac{\partial^2 w_1}{\partial x^2}\right) \\
&+\mu\frac{1}{\rho_0^2}\left(\frac{4}{3}\overline{\rho_1\frac{\partial^2 w_1}{\partial z^2}} + \frac{1}{3}\overline{\rho_1\frac{\partial^2 u_1}{\partial x\partial z}} + \overline{\rho_1\frac{\partial^2 w_1}{\partial x^2}}\right).
\end{aligned} \tag{B.6}$$

685 For kinetic energy (KE), KE is separated into background and perturbation parts. KE in
686 GWs is averaged over a wave period.

$$\begin{aligned}
KE_x &= \frac{1}{2}\overline{\rho u^2} \\
&= \frac{1}{2}\rho_0 u_0^2 + \frac{1}{2}\rho_0\overline{u_1^2} + \rho_0\overline{u_0 u_1},
\end{aligned} \tag{B.7}$$

687 where $\overline{u_0 u_1} = 0$ for averaging over a period. The horizontal part of background KE and
688 perturbation KE change rate are derived by multiplying $\rho_0 u_0$ and $\rho_0 u_1$ to every terms of
689 horizontal part of background and perturbation momentum change rate equations (B.3)
690 and (B.5), respectively. The same processes are applied to the vertical part of KE.

$$\begin{aligned}
&\rho_0\frac{\partial u_0^2}{2\partial t} + \rho_0 u_0\vec{v_0}\cdot\nabla u_0 + \rho_0 u_0\overline{\vec{v_1}\cdot\nabla u_1} \\
&= -u_0\frac{\partial p_0}{\partial x} + u_0\overline{\frac{\rho_1}{\rho_0}\frac{\partial p_1}{\partial x}} \\
&+\mu u_0\left(\frac{4}{3}\frac{\partial^2 u_0}{\partial x^2} + \frac{1}{3}\frac{\partial^2 w_0}{\partial x\partial z} + \frac{\partial^2 u_0}{\partial z^2}\right) - \mu\frac{u_0}{\rho_0}\left(\frac{4}{3}\overline{\rho_1\frac{\partial^2 u_1}{\partial x^2}} + \frac{1}{3}\overline{\rho_1\frac{\partial^2 w_1}{\partial x\partial z}} + \overline{\frac{\rho_1\partial^2 u_1}{\partial z^2}}\right).
\end{aligned} \tag{B.8}$$

$$\begin{aligned}
&\rho_0\frac{\partial u_1^2}{2\partial t} + \rho_0 u_1\vec{v_1}\cdot\nabla u_0 + \rho_0 u_1\vec{v_0}\cdot\nabla u_1 + \rho_0 u_1\vec{v_1}\cdot\nabla u_1 - \rho_0 u_1\overline{\vec{v_1}\cdot\nabla u_1} \\
&= -u_1\frac{\partial p_1}{\partial x} + \frac{u_1\rho_1}{\rho_0}\frac{\partial p_0}{\partial x} + \frac{\rho_1 u_1}{\rho_0}\frac{\partial p_1}{\partial x} - u_1\overline{\frac{\rho_1}{\rho_0}\frac{\partial p_1}{\partial x}} \\
&+\mu u_1\left(\frac{4}{3}\frac{\partial^2 u_1}{\partial x^2} + \frac{1}{3}\frac{\partial^2 w_1}{\partial x\partial z} + \frac{\partial^2 u_1}{\partial z^2}\right) \\
&-\mu\frac{u_1\rho_1}{\rho_0}\left(\frac{4}{3}\frac{\partial^2 u_0}{\partial x^2} + \frac{1}{3}\frac{\partial^2 w_0}{\partial x\partial z} + \frac{\partial^2 u_0}{\partial z^2} + \frac{4}{3}\frac{\partial^2 u_1}{\partial x^2} + \frac{1}{3}\frac{\partial^2 w_1}{\partial x\partial z} + \frac{\partial^2 u_1}{\partial z^2}\right) \\
&+\mu\frac{u_1}{\rho_0}\left(\frac{4}{3}\overline{\rho_1\frac{\partial^2 u_1}{\partial x^2}} + \frac{1}{3}\overline{\rho_1\frac{\partial^2 w_1}{\partial x\partial z}} + \overline{\frac{\rho_1\partial^2 u_1}{\partial z^2}}\right).
\end{aligned} \tag{B.9}$$

$$\begin{aligned}
&\rho_0\frac{\partial w_0^2}{2\partial t}+\rho_0 w_0\vec{v_0}\cdot\nabla w_0+\rho_0 w_0\overline{\vec{v_1}\cdot\nabla w_1}\\
&=-w_0\frac{\partial p_0}{\partial z}+w_0\overline{\frac{\rho_1}{\rho_0}\frac{\partial p_1}{\partial z}}-\rho_0 g w_0\\
&+\mu w_0\left(\frac{4}{3}\frac{\partial^2 w_0}{\partial z^2}+\frac{1}{3}\frac{\partial^2 u_0}{\partial x\partial z}+\frac{\partial^2 w_0}{\partial x^2}\right)\\
&-\mu\frac{w_0}{\rho_0}\left(\frac{4}{3}\overline{\rho_1\frac{\partial^2 w_1}{\partial z^2}}+\frac{1}{3}\overline{\rho_1\frac{\partial^2 u_1}{\partial x\partial z}}+\overline{\rho_1\frac{\partial^2 w_1}{\partial x^2}}\right).
\end{aligned} \tag{B.10}$$

$$\begin{aligned}
&\rho_0\frac{\partial w_1^2}{2\partial t}+\rho_0 w_1\vec{v_1}\cdot\nabla w_0+\rho_0 w_1\vec{v_0}\cdot\nabla w_1+\rho_0 w_1\vec{v_1}\cdot\nabla w_1-\rho_0 w_1\overline{\vec{v_1}\cdot\nabla w_1}\\
&=-w_1\frac{\partial p_1}{\partial z}+\frac{w_1\rho_1}{\rho_0}\frac{\partial p_0}{\partial z}+\frac{w_1\rho_1}{\rho_0}\frac{\partial p_1}{\partial z}-w_1\overline{\frac{\rho_1}{\rho_0}\frac{\partial p_1}{\partial z}}\\
&+\mu w_1\left(\frac{4}{3}\frac{\partial^2 w_1}{\partial z^2}+\frac{1}{3}\frac{\partial^2 u_1}{\partial x\partial z}+\frac{\partial^2 w_1}{\partial x^2}\right)\\
&-\mu\frac{\rho_1 w_1}{\rho_0}\left(\frac{4}{3}\frac{\partial^2 w_0}{\partial z^2}+\frac{1}{3}\frac{\partial^2 u_0}{\partial x\partial z}+\frac{\partial^2 w_0}{\partial x^2}+\frac{4}{3}\frac{\partial^2 w_1}{\partial z^2}+\frac{1}{3}\frac{\partial^2 u_1}{\partial x\partial z}+\frac{\partial^2 w_1}{\partial x^2}\right)\\
&+\mu\frac{w_1}{\rho_0}\left(\frac{4}{3}\overline{\rho_1\frac{\partial^2 w_1}{\partial z^2}}+\frac{1}{3}\overline{\rho_1\frac{\partial^2 u_1}{\partial x\partial z}}+\overline{\rho_1\frac{\partial^2 w_1}{\partial x^2}}\right),
\end{aligned} \tag{B.11}$$

Combining 2 parts of background KE tendency equations (B.8) and (B.10) together gives the KE_0 tendency:

$$\begin{aligned}
&\frac{\partial KE_0}{\partial t}+\rho_0 u_0 u_0\frac{\partial u_0}{\partial x}+\rho_0 w_0 w_0\frac{\partial w_0}{\partial z}+\rho_0 w_0 u_0\left(\frac{\partial w_0}{\partial x}+\frac{\partial u_0}{\partial z}\right)\\
&+\rho_0 u_0\overline{\vec{v_1}\cdot\nabla u_1}+\rho_0 w_0\overline{\vec{v_1}\cdot\nabla w_1}\\
&=-\vec{v_0}\cdot\nabla p_0+\vec{v_0}\cdot\overline{\frac{\rho_1}{\rho_0}\nabla p_1}-\rho_0 g w_0\\
&+\mu u_0\left(\frac{4}{3}\frac{\partial^2 u_0}{\partial x^2}+\frac{1}{3}\frac{\partial^2 w_0}{\partial x\partial z}+\frac{\partial^2 u_0}{\partial z^2}\right)\\
&-\mu\frac{u_0}{\rho_0}\left(\frac{4}{3}\overline{\rho_1\frac{\partial^2 u_1}{\partial x^2}}+\frac{1}{3}\overline{\rho_1\frac{\partial^2 w_1}{\partial x\partial z}}+\overline{\frac{\rho_1\partial^2 u_1}{\partial z^2}}\right)\\
&+\mu\frac{w_0}{\rho_0}\left(\frac{4}{3}\frac{\partial^2 w_0}{\partial z^2}+\frac{1}{3}\frac{\partial^2 u_0}{\partial x\partial z}+\frac{\partial^2 w_0}{\partial x^2}\right)\\
&-\mu\frac{w_0}{\rho_0}\left(\frac{4}{3}\overline{\rho_1\frac{\partial^2 w_1}{\partial z^2}}+\frac{1}{3}\overline{\rho_1\frac{\partial^2 u_1}{\partial x\partial z}}+\overline{\rho_1\frac{\partial^2 w_1}{\partial x^2}}\right).
\end{aligned} \tag{B.12}$$

Combining two parts of KE_1 equations (B.9) and (B.11) yields:

$$
\begin{aligned}
&\frac{\partial KE_1}{\partial t} + \rho_0 u_1 \vec{v_1}\cdot\nabla u_0 + \rho_0 u_1 \vec{v_0}\cdot\nabla u_1 + \rho_0 u_1 \vec{v_1}\cdot\nabla u_1 \\
&+\rho_0 w_1 \vec{v_1}\cdot\nabla w_0 + \rho_0 w_1 \vec{v_0}\cdot\nabla w_1 + \rho_0 w_1 \vec{v_1}\cdot\nabla w_1 \\
&= -\vec{v_1}\cdot\nabla p_1 + \frac{\vec{v_1}\rho_1}{\rho_0}\cdot\nabla p_0 + \frac{\vec{v_1}\rho_1}{\rho_0}\cdot\nabla p_1 \\
&+\rho_0 u_1 \overline{\vec{v_1}\cdot\nabla u_1} + \rho_0 w_1 \overline{\vec{v_1}\cdot\nabla w_1} - u_1 \overline{\frac{\rho_1}{\rho_0}\frac{\partial p_1}{\partial x}} - w_1 \overline{\frac{\rho_1}{\rho_0}\frac{\partial p_1}{\partial z}} \\
&+\rho_0 \frac{4}{3}\mu \frac{u_1}{\rho_0}\frac{\partial^2 u_1}{\partial x^2} + \rho_0 \frac{1}{3}\mu \frac{u_1}{\rho_0}\frac{\partial^2 w_1}{\partial x \partial z} + \rho_0 \mu \frac{u_1}{\rho_0}\frac{\partial^2 u_1}{\partial z^2} \\
&-\rho_0 \frac{4}{3}\mu \frac{u_1\rho_1}{\rho_0^2}\frac{\partial^2 u_0}{\partial x^2} - \rho_0 \frac{1}{3}\mu \frac{u_1\rho_1}{\rho_0^2}\frac{\partial^2 w_0}{\partial x \partial z} - \rho_0 \mu \frac{u_1\rho_1}{\rho_0^2}\frac{\partial^2 u_0}{\partial z^2} \\
&-\rho_0 \frac{4}{3}\mu \frac{u_1\rho_1}{\rho_0^2}\frac{\partial^2 u_1}{\partial x^2} - \rho_0 \frac{1}{3}\mu \frac{u_1\rho_1}{\rho_0^2}\frac{\partial^2 w_1}{\partial x \partial z} - \rho_0 \mu \frac{u_1\rho_1}{\rho_0^2}\frac{\partial^2 u_1}{\partial z^2} \\
&+\frac{4}{3}\mu\rho_0 \frac{w_1}{\rho_0}\frac{\partial^2 w_1}{\partial z^2} + \frac{1}{3}\mu\rho_0 \frac{w_1}{\rho_0}\frac{\partial^2 u_1}{\partial x \partial z} + \mu\rho_0 \frac{w_1}{\rho_0}\frac{\partial^2 w_1}{\partial x^2} \\
&-\mu\rho_0 \frac{\rho_1 w_1}{\rho_0^2}\frac{4}{3}\frac{\partial^2 w_0}{\partial z^2} - \mu\rho_0 \frac{\rho_1 w_1}{\rho_0^2}\frac{1}{3}\frac{\partial^2 u_0}{\partial x \partial z} - \mu\rho_0 \frac{\rho_1 w_1}{\rho_0^2}\frac{\partial^2 w_0}{\partial x^2} \\
&-\mu\rho_0 \frac{\rho_1 w_1}{\rho_0^2}\frac{4}{3}\frac{\partial^2 w_1}{\partial z^2} - \mu\rho_0 \frac{\rho_1 w_1}{\rho_0^2}\frac{1}{3}\frac{\partial^2 u_1}{\partial x \partial z} - \mu\rho_0 \frac{\rho_1 w_1}{\rho_0^2}\frac{\partial^2 w_1}{\partial x^2}.
\end{aligned}
\tag{B.13}
$$

From the tendency for KE in perturbation, it is clear that the instantaneous KE_1 variation is related to BG flow expansion or compression, products of perturbation momentum flux and BG shear, advection, BG pressure gradient work, and perturbation pressure gradient work. Based on the model output, the KE change due to diffusivity is negligible. So equations for tendencies can be simplified as:

$$
\begin{aligned}
&\frac{\partial KE_0}{\partial t} + \rho_0 u_0 u_0 \frac{\partial u_0}{\partial x} + \rho_0 w_0 w_0 \frac{\partial w_0}{\partial z} + \rho_0 w_0 u_0 \left(\frac{\partial w_0}{\partial x} + \frac{\partial u_0}{\partial z}\right) \\
&+\rho_0 u_0 \overline{\vec{v_1}\cdot\nabla u_1} + \rho_0 w_0 \overline{\vec{v_1}\cdot\nabla w_1} \\
&= -\vec{v_0}\cdot\nabla p_0 + \vec{v_0}\cdot\overline{\frac{\rho_1}{\rho_0}\nabla p_1} - \rho_0 g w_0,
\end{aligned}
\tag{B.14}
$$

$$
\begin{aligned}
&\frac{\partial KE_1}{\partial t} + \rho_0 u_1 \vec{v_1}\cdot\nabla u_0 + \rho_0 u_1 \vec{v_0}\cdot\nabla u_1 + \rho_0 u_1 \vec{v_1}\cdot\nabla u_1 \\
&+\rho_0 w_1 \vec{v_1}\cdot\nabla w_0 + \rho_0 w_1 \vec{v_0}\cdot\nabla w_1 + \rho_0 w_1 \vec{v_1}\cdot\nabla w_1 \\
&= -\vec{v_1}\cdot\nabla p_1 + \frac{\vec{v_1}\rho_1}{\rho_0}\cdot\nabla p_0 + \frac{\vec{v_1}\rho_1}{\rho_0}\cdot\nabla p_1 \\
&+\rho_0 u_1 \overline{\vec{v_1}\cdot\nabla u_1} + \rho_0 w_1 \overline{\vec{v_1}\cdot\nabla w_1} - u_1 \overline{\frac{\rho_1}{\rho_0}\frac{\partial p_1}{\partial x}} - w_1 \overline{\frac{\rho_1}{\rho_0}\frac{\partial p_1}{\partial z}}.
\end{aligned}
\tag{B.15}
$$

Acknowledgments

This work and the Na lidar operation at ALO is being supported by the National Science Foundation (NSF) grants AGS-1759471.

References

Achatz, U. (2007), Gravity-wave breaking: Linear and primary nonlinear dynamics, *Adv. Space Res.*, *40*(6), 719–733, doi:10.1016/j.asr.2007.03.078.

Andreassen, Ø., C. E. Wasberg, D. C. Fritts, and J. R. Isler (1994), Gravity wave breaking in two and three dimensions: 1. model description and comparison of two-dimensional evolutions, *J. Geophys. Res. Atmos.*, *99*(D4), 8095–8108, doi:10.1029/93JD03435.

Atlas, R., and C. Bretherton (2022), Aircraft observations of gravity wave activity and turbulence in the tropical tropopause layer: prevalence, influence on cirrus and comparison with global-storm resolving models, *Atmos Chem Phys.*, *2022*, 1–30, doi:10.5194/acp-2022-491.

Barat, J., and J. C. Genie (1982), A new tool for the three-dimensional sounding of the atmosphere: The helisonde, *Journal of Applied Meteorology and Climatology*, *21*(10), 1497 – 1505, doi:10.1175/1520-0450(1982)021<1497:ANTFTT>2.0.CO;2.

Barbano, F., L. Brogno, F. Tampieri, and S. Di Sabatino (2022), Interaction between waves and turbulence within the nocturnal boundary layer, *Boundary-Layer Meteorol*, *183*, doi:10.1007/s10546-021-00678-2.

Becker, E., and G. Schmitz (2002), Energy deposition and turbulent dissipation owing to gravity waves in the mesosphere, *J. Atmos. Sci.*, *59*(1), 54 – 68, doi:10.1175/1520-0469(2002)059<0054:EDATDO>2.0.CO;2.

Bühler, O. (2010), Wave–vortex interactions in fluids and superfluids, *Annual Review of Fluid Mechanics*, *42*(1), 205–228, doi:10.1146/annurev.fluid.010908.165251.

Bölöni, G., B. Ribstein, J. Muraschko, C. Sgoff, J. Wei, and U. Achatz (2016), The interaction between atmospheric gravity waves and large-scale flows: An efficient description beyond the nonacceleration paradigm, *J. Atmos. Sci.*, *73*(12), 4833 – 4852, doi: 10.1175/JAS-D-16-0069.1.

Clayson, C. A., and L. Kantha (2008), On turbulence and mixing in the free atmosphere inferred from high-resolution soundings, *J. Atmos. Ocean. Technol.*, *25*(6), 833 – 852, doi:10.1175/2007JTECHA992.1.

de Nijs, M. A. J., and J. D. Pietrzak (2012), On total turbulent energy and the passive and active role of buoyancy in turbulent momentum and mass transfer, *Ocean Dynamics*, *62*, 849–865, doi:10.1007/s10236-012-0536-6.

Dong, W., D. C. Fritts, T. S. Lund, S. A. Wieland, and S. Zhang (2020), Self-acceleration and instability of gravity wave packets: 2. two-dimensional packet propagation, instability dynamics, and transient flow responses, *J.Geophys.Res.Atmos*, *125*(3), e2019JD030,691, doi:10.1029/2019JD030691.

Dong, W., D. C. Fritts, M. P. Hickey, A. Z. Liu, T. S. Lund, S. Zhang, Y. Yan, and F. Yang (2022), Modeling studies of gravity wave dynamics in highly structured environments: Reflection, trapping, instability, momentum transport, secondary gravity waves, and induced flow responses, *Journal of Geophysical Research: Atmospheres*, *127*(13), e2021JD035,894, doi:https://doi.org/10.1029/2021JD035894, e2021JD035894 2021JD035894.

Doran, P. M. (2013), Chapter 7 - fluid flow, in *Bioprocess Engineering Principles (Second Edition)*, edited by P. M. Doran, second edition ed., pp. 201–254, Academic Press, London, doi:https://doi.org/10.1016/B978-0-12-220851-5.00007-1.

Dunkerton, T. J. (1987), Effect of nonlinear instability on gravity-wave momentum transport, *J. Atmos. Sci.*, *44*(21), 3188 – 3209, doi:10.1175/1520-0469(1987)044<3188:EONIOG>2.0.CO;2.

Dunkerton, T. J., and D. C. Fritts (1984), Transient gravity wave-critical layer interaction. I Convective adjustment and the mean zonal acceleration, *J. Atmos. Sci.*, *41*, 992–1007, doi:10.1175/1520-0469(1984)041<0992:TGWCLI>2.0.CO;2.

Einaudi, F., and J. J. Finnigan (1993), Wave-turbulence dynamics in the stably stratified boundary layer, *50:13*, doi:10.1175/1520-0469(1993)050<1841:WTDITS>2.0.CO;2.

Felten, F. N., and T. S. Lund (2006), Kinetic energy conservation issues associated with the collocated mesh scheme for incompressible flow, *Journal of Computational Physics*, *215*(2), 465 – 484, doi:https://doi.org/10.1016/j.jcp.2005.11.009.

Finnigan, J. J. (1988), Kinetic energy transfer between internal gravity waves and turbulence, *Journal of Atmospheric Sciences*, *45*(3), 486 – 505, doi:10.1175/1520-0469(1988)045<0486:KETBIG>2.0.CO;2.

Finnigan, J. J., and F. Einaudi (1981), The interaction between an internal gravity wave and the planetary boundary layer. part ii: Effect of the wave on the turbulence structure, *Q J R Meteorol Soc.*, *107*(454), 807–832, doi:https://doi.org/10.1002/qj.49710745405.

Finnigan, J. J., and R. H. Shaw (2008), Double-averaging methodology and its application to turbulent flow in and above vegetation canopies, *Acta Geophysica*, *56*, 534 – 561, doi:10.2478/s11600-008-0034-x.

Finnigan, J. J., F. Einaudi, and D. Fua (1984), The interaction between an internal gravity wave and turbulence in the stably-stratified nocturnal boundary layer, *J. Atmos. Sci.*, *41*(16), 2409 – 2436, doi:10.1175/1520-0469(1984)041<2409:TIBAIG>2.0.CO;2.

Fritts, D. C. (1989), A review of gravity wave saturation processes, effects, and variability in the middle atmosphere, *pure and applied geophysics*, *130*, 343–371, doi: 10.1007/BF00874464.

Fritts, D. C., and M. J. Alexander (2003), Gravity wave dynamics and effects in the middle atmosphere, *Rev. Geophys.*, *41*(1), doi:https://doi.org/10.1029/2001RG000106.

Fritts, D. C., and T. J. Dunkerton (1985), Fluxes of heat and constituents due to convectively unstable gravity waves, *J. Atmos. Sci.*, *42*(6), 549–556, doi:10.1175/1520-0469(1985)042<0549:FOHACD>2.0.CO;2.

Fritts, D. C., J. R. Isler, and Ø. Andreassen (1994), Gravity wave breaking in two and three dimensions: 2. Three-dimensional evolution and instability structure, *J. Geophys. Res.*, *99*(D4), 8109–8123, doi:10.1029/93JD03436.

Fritts, D. C., J. F. Garten, and Øyvind Andreassen (1996), Wave breaking and transition to turbulence in stratified shear flows, *J. Atmos. Sci.*, *53*(8), 1057 – 1085, doi: 10.1175/1520-0469(1996)053<1057:WBATTT>2.0.CO;2.

Fritts, D. C., C. Bizon, J. A. Werne, and C. K. Meyer (2003), Layering accompanying turbulence generation due to shear instability and gravity-wave breaking, *J. Geophys. Res. Atmos.*, *108*(D8), doi:https://doi.org/10.1029/2002JD002406.

Fritts, D. C., B. P. Williams, C. Y. She, J. D. Vance, M. Rapp, F.-J. Lübken, A. Müllemann, F. J. Schmidlin, and R. A. Goldberg (2004), Observations of extreme temperature and wind gradients near the summer mesopause during the macwave/midas rocket campaign, *Geophys. Res. Lett.*, *31*(24), doi:https://doi.org/10.1029/2003GL019389.

Fritts, D. C., L. Wang, and J. A. Werne (2013a), Gravity wave–fine structure interactions. part i: Influences of fine structure form and orientation on flow evolution and instability, *J. Atmos. Sci*, *70*(12), 3710 – 3734, doi:10.1175/JAS-D-13-055.1.

Fritts, D. C., L. Wang, and J. A. Werne (2013b), Gravity wave–fine structure interactions. part i: Influences of fine structure form and orientation on flow evolution and instability, *Journal of the Atmospheric Sciences*, *70*(12), 3710 – 3734, doi:10.1175/JAS-D-13-055.1.

Fritts, D. C., B. Laughman, T. S. Lund, and J. B. Snively (2015), Self-acceleration and instability of gravity wave packets: 1. effects of temporal localization, *J. Geophys. Res. Atmos.*, *120*(17), 8783–8803, doi:https://doi.org/10.1002/2015JD023363.

Fritts, D. C., L. Wang, M. A. Geller, D. A. Lawrence, J. Werne, and B. B. Balsley (2016), Numerical Modeling of Multiscale Dynamics at a High Reynolds Number: Instabilities, Turbulence, and an Assessment of Ozmidov and Thorpe Scales, *J.Atmos.Sci*, *73*, 555–578.

Fritts, D. C., L. Wang, G. Baumgarten, A. D. Miller, M. A. Geller, G. Jones, M. Limon, D. Chapman, J. Didier, C. B. Kjellstrand, D. Araujo, S. Hillbrand, A. Korotkov, G. Tucker, and J. Vinokurov (2017a), High-resolution observations and modeling of turbulence sources, structures, and intensities in the upper mesosphere, *J. Atmos. Sol. Terr. Phys.*, *162*, 57–78, doi:https://doi.org/10.1016/j.jastp.2016.11.006, layered Phenomena in the Mesopause Region.

Fritts, D. C., L. Wang, G. Baumgarten, A. D. Miller, M. A. Geller, G. Jones, M. Limon, D. Chapman, J. Didier, C. B. Kjellstrand, D. Araujo, S. Hillbrand, A. Korotkov, G. Tucker, and J. Vinokurov (2017b), High-resolution observations and modeling of turbulence sources, structures, and intensities in the upper mesosphere, *J. Atmos. Sol. Terr. Phys.*, *162*, 57 – 78, doi:https://doi.org/10.1016/j.jastp.2016.11.006, layered Phenomena in the Mesopause Region.

Fritts, D. C., W. Dong, T. S. Lund, S. Wieland, and B. Laughman (2020), Self-acceleration and instability of gravity wave packets: 3. three-dimensional packet propagation, secondary gravity waves, momentum transport, and transient mean forcing in tidal winds, *J. Geophys. Res. Atmos.*, *125*(3), e2019JD030,692, doi: https://doi.org/10.1029/2019JD030692.

Fritts, D. C., L. Wang, T. S. Lund, S. A. Thorpe, C. B. Kjellstrand, B. Kaifler, and N. Kaifler (2022a), Multi-scale kelvin-helmholtz instability dynamics observed by pmc turbo on 12 july 2018: 2. dns modeling of khi dynamics and pmc responses, *J. Geophys. Res. Atmos.*, *127*(18), e2021JD035,834, doi:https://doi.org/10.1029/2021JD035834.

Fritts, D. C., L. Wang, T. Lund, and S. Thorpe (2022b), Multi-scale dynamics of kelvin–helmholtz instabilities. part 1. secondary instabilities and the dynamics of tubes and knots, *J. Fluid Mech.*, *941*, A30, doi:10.1017/jfm.2021.1085.

Fritts, D. C., L. Wang, S. Thorpe, and T. Lund (2022c), Multi-scale dynamics of kelvin–helmholtz instabilities. part 2. energy dissipation rates, evolutions and statistics, *J. Fluid Mech.*, *941*, A31, doi:10.1017/jfm.2021.1086.

Fua, D., G. Chimonas, F. Einaudi, and O. Zeman (1982), An analysis of wave-turbulence interaction, *J. Atmos. Sci.*, *39*(11), 2450–2463, doi:10.1175/1520-0469(1982)039<2450:AAOWTI>2.0.CO;2.

Hines, C. O. (1991), The saturation of gravity waves in the middle atmosphere. part i: Critique of linear-instability theory, *J. Atmos. Sci.*, *48*, 1348–1359, doi:10.1175/1520-0469(1991)048<1348:TSOGWI>2.0.CO;2.

Hunt, J. C. R., J. C. Kaimal, and J. E. Gaynor (1985), Some observations of turbulence structure in stable layers, *Q J R Meteorol Soc.*, *111*(469), 793–815, doi: https://doi.org/10.1002/qj.49711146908.

Klostermeyer, J. (1991), Two- and three-dimensional parametric instabilities in finite-amplitude internal gravity waves, *Geophys. Astrophys. Fluid Dyn.*, *61*(1-4), 1–25, doi: 10.1080/03091929108229035.

Koch, S. E., B. D. Jamison, C. Lu, T. L. Smith, E. I. Tollerud, C. Girz, N. Wang, T. P. Lane, M. A. Shapiro, D. D. Parrish, and O. R. Cooper (2005), Turbulence and gravity waves within an upper-level front, *J. Atmos. Sci*, *62*(11), 3885 – 3908, doi: 10.1175/JAS3574.1.

Koudella, C. R., and C. Staquet (2006), Instability mechanisms of a two-dimensional progressive internal gravity wave, *J. Fluid Mech*, *548*, 165–196, doi: 10.1017/S0022112005007524.

Lelong, M. P., and J. J. Riley (1991), Internal wave—vortical mode interactions in strongly stratified flows, *J. Fluid Mech.*, *232*, 1–19, doi:10.1017/S0022112091003609.

Lindzen, R. S. (1967), Thermally driven diurnal tide in the atmosphere, *Q J R Meteorol Soc.*, *93*(395), 18–42, doi:https://doi.org/10.1002/qj.49709339503.

Lindzen, R. S. (1968), Rossby waves with negative equivalent depths – comments on a note by g. a. corby, *Q J R Meteorol Soc.*, *94*(401), 402–407, doi: https://doi.org/10.1002/qj.49709440116.

Lindzen, R. S. (1971), Equatorial planetary waves in shear. part i, *J. Atmos. Sci.*, *28*(4), 609 – 622, doi:10.1175/1520-0469(1971)028<0609:EPWISP>2.0.CO;2.

Lindzen, R. S. (1981), Turbulence and stress owing to gravity wave and tidal breakdown, *J. Geophys. Res. Oceans*, *86*(C10), 9707–9714, doi: https://doi.org/10.1029/JC086iC10p09707.

Liu, X., J. Xu, H.-L. Liu, and R. Ma (2008), Nonlinear interactions between gravity waves with different wavelengths and diurnal tide, *J. Geophys. Res. Atmos.*, *113*(D8), doi: https://doi.org/10.1029/2007JD009136.

Liu, X., J. Xu, H.-L. Liu, J. Yue, and W. Yuan (2014), Simulations of large winds and wind shears induced by gravity wave breaking in the mesosphere and lower thermosphere (MLT) region, *Ann. Geophys.*, *32*(5), 543–552, doi:10.5194/angeo-32-543-2014.

Pairaud, I., C. Staquet, J. Sommeria, and M. M. Mahdizadeh (2010), Generation of harmonics and sub-harmonics from an internal tide in a uniformly stratified fluid: numerical and laboratory experiments, in *IUTAM Symposium on Turbulence in the Atmosphere and Oceans*, edited by D. Dritschel, pp. 51–62, Springer Netherlands, Dordrecht.

Palmer, A. J. (1996), A spectral model for turbulence and microphysics dynamics in an ice cloud, *Nonlinear Process Geophys*, *3*(1), 23–28, doi:10.5194/npg-3-23-1996.

Reiter, E. R. (1969), Structure of vertical wind profiles, *Radio Science*, *4*(12), 1133–1136, doi:https://doi.org/10.1029/RS004i012p01133.

Reynolds, W. C., and A. K. M. F. Hussain (1972), The mechanics of an organized wave in turbulent shear flow. part 3. theoretical models and comparisons with experiments, *J. Fluid Mech.*, *54*(2), 263–288, doi:10.1017/S0022112072000679.

Sedlak, R., P. Hannawald, C. Schmidt, S. Wúst, M. Bittner, and S. Stanič (2021), Gravity wave instability structures and turbulence from more than 1.5 years of oh* airglow imager observations in slovenia, *Atmospheric Measurement Techniques*, *14*(10), 6821–6833, doi:10.5194/amt-14-6821-2021.

Sun, J., C. J. Nappo, L. Mahrt, D. Belušić, B. Grisogono, D. R. Stauffer, M. Pulido, C. Staquet, Q. Jiang, A. Pouquet, C. Yagüe, B. Galperin, R. B. Smith, J. J. Finnigan, S. D. Mayor, G. Svensson, A. A. Grachev, and W. D. Neff (2015), Review of wave-turbulence interactions in the stable atmospheric boundary layer, *Rev. Geophys*, *53*(3), 956–993, doi:https://doi.org/10.1002/2015RG000487.

Sutherland, B. R. (2010), *Internal Gravity Waves*, Cambridge University Press, doi: 10.1017/CBO9780511780318.

Werne, J., and D. C. Fritts (1999), Stratified shear turbulence: Evolution and statistics, *Geophys. Res. Lett.*, *26*(4), 439–442, doi:https://doi.org/10.1029/1999GL900022.

Winters, K. B., and J. J. Riley (1992), Instability of internal waves near a critical level, *Dyn. Atmospheres Oceans*, *16*(3), 249–278, doi:https://doi.org/10.1016/0377-0265(92)90009-I.

Yang, F., and A. Z. Liu (2022), Stability characteristics of the mesopause region above the andes, *J. Geophys. Res. Space Phys.*, *127*(9), e2022JA030,315, doi: https://doi.org/10.1029/2022JA030315.

Yim, E., P. Meliga, and F. Gallaire (2019), Self-consistent triple decomposition of the turbulent flow over a backward-facing step under finite amplitude harmonic forcing, *Proc. R. Soc. A*, *475*(2225), 20190,018, doi:10.1098/rspa.2019.0018.

Zovko-Rajak, D., T. P. Lane, R. D. Sharman, and S. B. Trier (2019), The role of gravity wave breaking in a case of upper-level near-cloud turbulence, *Mon. Weather Rev.*, *147*(12), 4567 – 4588, doi:10.1175/MWR-D-18-0445.1.